Master's thesis

NTNU
Norwegian University of Science and Technology
Faculty of Natural Sciences
Department of Physics

Supreet Kaur

TEM Characterization of Strontium Barium Niobate ($Sr_xBa_{1-x}Nb_2O_6$) thin films.

Master's thesis in Physics
Supervisor: Randi Holmestad
Co-supervisor: Per Erik Vullum
July 2023

Norwegian University of Science and Technology

Supreet Kaur

TEM Characterization of Strontium Barium Niobate ($Sr_xBa_{1-x}Nb_2O_6$) thin films.

Master's thesis in Physics
Supervisor: Randi Holmestad
Co-supervisor: Per Erik Vullum
July 2023

Norwegian University of Science and Technology
Faculty of Natural Sciences
Department of Physics

Abstract

In this master thesis, transmission electron microscopy (TEM) was used to study the orientation of the grains in strontium barium niobate $Sr_xBa_{1-x}Nb_2O_6$ (SBN) thin films grown on (001) oriented strontium titanate $SrTiO_3$ (STO) substrates by chemical solution deposition which is an environmentally friendly and cheap production method. To prepare the TEM samples, focused ion beam was used. Two samples named SBN 001 and SBN 310 were studied, differentiated on the basis of the heat treatments given, and the termination of the substrate. The aim of the study was to determine the polarization (direction of c-axis) of the grains inside the thin film, to decide whether it was in-plane or out-of-plane. In order to find the polarization, various TEM techniques were used such as bright field imaging, selected area electron diffraction, high-resolution transmission electron microscopy, energy dispersive spectroscopy, and electron energy loss spectroscopy. These TEM techniques helped: to have an overview of the film, find out the direction of the c-axis, to have elemental information, know about substrate termination, and know the interdiffusion between the film and the substrate.

The hypothesis was that the sample SBN 001 has mainly grains with out-of-plane polarization and SBN 310 has grains with in-plane polarization. After studying SAED patterns 54 grains of SBN 001 and 41 grains of SBN 310, it was found that in SBN 100, 92.6% of the grains have out-of-plane polarization, 3.7% have in-plane polarization, and 3.7% have random orientation. In sample SBN 310, only 56.1% of the grains have in-plane polarization, 12.2% grains have out-of-plane polarization, and the remaining 31.7% have random orientation. SBN 001 was studied by high-resolution imaging scanning transmission electron microscopy, energy dispersive and electron energy loss spectroscopy and line profiles of chemical composition were obtained from the grains of different orientations which are in-plane, out-of-plane, and random. It was found in that the interface between film and substrate is not flat, which is why it was difficult to say something about the substrate termination. From chemical composition maps, it was found that Sr and Ba occupy different sites in SBN. Line profiles showed that the titanium peak does not decay to zero upto 15nm in the film. Future studies can focus on how to avoid having randomly oriented grains and how to grow film with only out-of-plane polarization as it can then be used in memory cells.

Sammendrag

I denne masteroppgaven, ble transmisjonselektron mikroskopi (TEM) benyttet for å grundig undersøke kornorienteringen i tynne filmer av strontium barium niobat $Sr_xBa_{1x}Nb_2O_6$ (SBN) som ble dyrket på (001)-orienterte substrater av strontium titanat $SrTiO_3$ (STO) ved hjelp av kjemisk løsningsdeponering, en kostnadseffektiv og miljøvennlig produksjonsmetode. For å forberede TEM-prøvene ble en presisjonsskåret ionestråle brukt. To prøver, betegnet SBN 001 og SBN 310, ble nøye undersøkt, med differensiering basert på varmebehandlingen som ble påført og termineringen av substratet. Formålet med studien var å nøyaktig bestemme polarisasjonen (retningen av c-aksen) til kornene i den tynne filmen for å avgjøre om de var i planet eller utenfor planet. For å oppnå dette ble flere TEM-teknikker tatt i bruk, inkludert lysfeltavbildning, utvalgt område elektron-diffraksjon, høyoppløsning transmisjonselektronmikroskopi, energispredningsspektroskopi og elektronenergitapspektroskopi. Disse sofistikerte TEM-teknikkene bidro til å gi en helhetlig forståelse av filmstrukturen, fastslå retningen av c-aksen, skaffe informasjon om elementene som inngår, vurdere substratets terminering og analysere interdiffusjonen mellom filmen og substratet.

Hypotesen som ble testet i studien var at SBN 001 primært besto av korn med polarisasjon utenfor planet, mens SBN 310 hadde korn med polarisasjon i planet. Resultatene av analysen av utvalgte område elektron-diffraksjonsmønstre for 54 korn i SBN 001 og 41 korn i SBN 310 bekreftet dette. I SBN 001 viste det seg at hele 92,6% av kornene hadde polarisasjon utenfor planet, mens 3,7% hadde polarisasjon i planet og 3,7% hadde tilfeldig orientering. I SBN 310 bare 56,1% av kornene polarisasjon i planet, 12,2% hadde polarisasjon utenfor planet, og de gjenværende 31,7% hadde tilfeldig orientering. Videre ble SBN 001 studert grundig ved hjelp av høyoppløselig skanningstransmisjonselektronmikroskop avbildning, energispredning og elektronenergitapspektroskopi. Linjeprofiler ble analysert for å få innsikt i den kjemiske sammensetningen til korn med ulike orienteringer, inkludert i planet, utenfor planet og tilfeldig. Det ble observert at grensesnittet mellom filmen og substratet ikke var flatt, hvilket gjorde det vanskelig å konkludere med sikkerhet angående termineringen av substratet.

Fremtidige studier kan rette fokus mot metoder for å unngå tilfeldig orienterte korn og realisere vekst av filmer med kun polarisasjon utenfor planet, da dette kan ha betydelig anvendelse i minneceller.

Preface

This thesis concludes my Master of Science Physics degree at the Department of Physics of the Norwegian University of Science and Technology (NTNU). It is a part of the PhD project studied by Viviann Hole Pedersen with supervisor Mari-Ann Einarsrud from the Department of Material Science and Engineering at NTNU. The experimental work presented in this thesis was carried out at TEM Gemini Centre and Nano lab at the Department of Physics. This work was supervised by Professor Randi Holmestad and Senior Researcher at SINTEF Industry and Associate Professor II at NTNU, Per Erik Vullum.

Many people have helped me through this journey, and I owe them my gratitude. I would first like to thank my main supervisor Professor Randi Holmestad, for giving constant support and feedback. A big thank you to my co-supervisor Per Erik Vullum for his invaluable guidance and feedback throughout this project. Thank you for acquiring the HAADF-STEM images, teaching me how to make line profiles, answering my emails, and clearing my doubts. A great thank you to Bjørn Gunnar Soleim and Emil Frang Christiansen for educating me on how to use TEM and coming to my aid when TEM gave me trouble. I would like to thank Jørgen A. Sørhaug, Emil, and Håkon Wiik Ånes for looking through my overleaf document and solving the problem. A very big thank you to Viviann Hole Pedersen for her guidance and feedback on my writing. I would also like to thank Dipanwita Chatterjee for teaching me how to perform tilting, how to use different software, giving feedback on my presentations and always checking on me how I was doing. Thanks to Elisabeth Savitri Thrane for giving me feedback and helping me solving issues realted to overleaf commands.Thanks to my family member who helped me installing windows on macOS and made it possible for me use digital micrograph and ReciPro on my mac. I am very grateful to my husband for all his immense support and motivation. Very special thanks to my daughter who taught me how to stay energetic all the time and also to make my tasks more challenging. Last, but not least, I am thankful to my friends and my parents who were constant sources of inspiration.

I look forward to the next chapter in my life, starting PhD with the Centre for Research-based Innovation (SFI) in the field of physical metallurgy (PhysMet).

List of Acronyms

AFM	Atomic Force Microscopy
BF	Bright Field
BFP	Back Focal Plane
CA	Condenser Aperture
CL	Condenser Lens
CSD	Chemical Solution Deposition
DF	Dark Field
DP	Diffraction Pattern
EDS	Energy Dispersive spectroscopy
EELS	Electron Energy-Loss Spectroscopy
EM	Electromagnetic
FeRAM	Ferroelectric Random Access Memory
FEG	Field Emission Gun
FT	Fourier Transform
FIB	Focused Ion Beam
HAADF	High Angle Annular Dark Field
HOLZ	High Ordered Laue Zone
HRTEM	High Resolution Transmission Electron Microscopy/Microscope
LOLZ	Low Ordered Laue Zone
NV	Non Volatite
OA	Objective Aperture
OL	Objective Lens
PZT	$Pb[Zr_xTi_{1-x}]O_3$
SA	Selected area Aperture
SADP	Selected Area Diffraction Pattern
SAED	Selected Area Electron Diffraction
SBN	$Sr_xBa1 - xNb_2O_6$
SEM	Scanning Electron Microscopy/ Micrpcope
STEM	Scanning Transmission Electron Microscopy/Microscope
STO	$SrTiO_3$
TTB	Tetragonal Tungsten Bronze
VLM	Visible Light Microscope
TEM	Transmission Electron Microscopy/Microscope

Table of Contents

1 Introduction **1**

2 Theory **3**

2.1 Basic Crystallography 3

2.1.1 Lattice and lattice types 3

2.1.2 Index System for Crystal Planes 5

2.1.3 Reciprocal Lattice 6

2.2 Ferroelectrics 8

2.2.1 Introduction to ferroelectric materials 8

2.2.2 Applications of ferroelectrics 10

2.3 About Strontium Barium Niobate (SBN) 12

2.3.1 Crystal structure of SBN 12

2.3.2 Symmetry considerations and ferroelectric properties 14

2.3.3 Relation between SBN and STO 15

2.4 Transmission Electron Microscopy 17

2.4.1 Electron-matter interaction 18

2.4.2 Diffraction 22

2.4.3 TEM Hardware and Imaging Techniques 24

2.5 Imaging Techniques 27

3 Experimental Methods **36**

3.1 Chemical Solution Deposition 36

3.2 Focussed Ion Beam (FIB) sample preparation 38

3.3 TEM operations 38

3.4 ReciPro Simulations of Diffraction Patterns 39

4 Results **43**

4.1 Thin Film Microstructure 43

4.2 Understanding Orientation with DPs 47

4.3 To find out-of-plane orientation 52

4.4 Statistics of the grains 55

4.5 Results from JEOL JEM-ARM200F 56

5 Discussion **60**

6 Conclusion **62**

References **63**

Appendix **68**

A SBN 001 **68**

B SBN 310 **71**

1 Introduction

Materials and material science play an important role in the development of human life from the stone age to the bronze age to the iron age and now to the computer age [53]. A better understanding of materials can help to develop innovative materials. Such materials are essential for safety, clean energy, transportation, human health, and industrial productivity. To discover new materials it is important for researchers to deepen their knowledge of the structural, morphological, thermal, and mechanical properties of the materials from macro- to nanoscale. Electron microscopy is a technique capable of providing insight into materials down to the nanoscale [54]. Since everyone is now encouraged to lead greener lifestyles, emphasis has been made to develop environmentally friendly materials with environmentally friendly methods.

Ferroelectrics materials are an important class of materials and are everywhere in modern society from consumer electronics to car engines [24]. These materials have spontaneous and switchable polarization and these have been studied for a long time for their use in ferroelectric random-access memories, pyroelectric detectors, electro-optic modulators, and more [16]. The maximum number of technologically important ferroelectrics have the perovskite crystal structure, and the leading material is lead zirconate titanate (PZT) [55]. PZT contains 60% by weight of toxic lead, therefore effort has been made on finding an alternative to replace PZT. One such option is the tetragonal tungsten bronze $Sr_xBa_{1-x}Nb_20_6$ (SBN) [59]. Due to its unfilled tetragonal tungsten bronze structure, it has great flexibility and tunable properties. The ferroelectric polarization in SBN is uniaxial along the c-axis [28]. Thin films of SBN have been deposited by a low-cost, environmentally friendly, and flexible deposition method, called aqueous chemical solution deposition [16].

For its use in ferroelectric random-access memories, it is important for filmmakers to know and control the mechanism of polarization. Transmission electron microscopy is one of the techniques that can help us to find out the direction of polarization or the direction of the c-axis. Therefore, the aim of this study is to look out for the polarization of the grains and how this polarization is affected by using different TEM techniques. Two SBN thin films were grown on a strontium titanate substrate $SrTiO_3$ (STO) using different heating rates and substrate terminations. With the help of various TEM techniques, it was discovered that the grains in the film have in-plane, out-of-plane, and random orientations. Later, it was discovered that the quality of the substrate affects the orientation relationship.

The layout of the thesis is given as follows: Chapter 2 consists of an overview of the theory needed to understand the crystals, the material SBN, and transmission electron microscopy. The

experimental methods are introduced in Chapter 3, to help to understand the methods used for the growth of the thin films and TEM sample preparation along with simulations needed to understand the results. The results are introduced in Chapter 4 and discussed in Chapter 5. Chapter 6 explores further work that can be done. The appendices contain supporting results.

2 Theory

2.1 Basic Crystallography

Crystallography is important to introduce here because there is a very strong relationship between crystal structure and properties of the material. As an example, ferroelectricity is directly related to the crystal structure of the material and it is the crystal structure that determines if a material is ferroelectric or not, and along which direction the polarization occurs. To better understand the TEM results it is significant to learn about crystals and crystal structures. This section is based on `Introduction to Solid State Physics´ by Charles Kittel [1] and `Solid State Physics´, An introduction by Philip Hofmann [3]. Therefore, citations throughout this section are omitted.

On the basis of the arrangement of atoms with respect to each other, the material can be classified as Crystalline or Amorphous. The materials in which atoms are placed in a periodic array over a long range are known as crystalline [8]. The structure of such materials can be well defined by explaining *Lattice* and *Basis*. A lattice is a regular and periodic arrangement of points in space. It can be two-dimensional or three-dimensional. A Basis is described as a group of similar atoms or molecules that are placed on a lattice to make a crystal. A basis can be a single atom or it can be a complex arrangement of hundreds of atoms. The center position of an atom k in a basis with respect to the associated lattice point that is the origin is described by the following equation. The origin can be arranged such that $0 \leq x_k, y_k, z_k \leq 1$.

$$r_k = x_k\vec{a_1} + y_k\vec{a_2} + z_k\vec{a_3}, \tag{2.1}$$

An example of how crystal structure is formed by convolving lattice and basis is shown in figure 2.1.

2.1.1 Lattice and lattice types

As stated earlier, lattice can be two-dimensional or three-dimensional and a three-dimensional lattice can be described by the following equation

$$R = u_1\vec{a_1} + u_2\vec{a_2} + u_3\vec{a_3}, \tag{2.2}$$

where $\vec{a_1}, \vec{a_2}, \vec{a_3}$ are translation vectors and u_1, u_2, u_3 are arbitrary integers. This kind of lattice is called Braivais lattice. Based on different combinations of the length of vectors $\vec{a_1}, \vec{a_2}, \vec{a_3}$ and the angles between them α, β, γ together with positions of the basis, there are 5 lattices in two

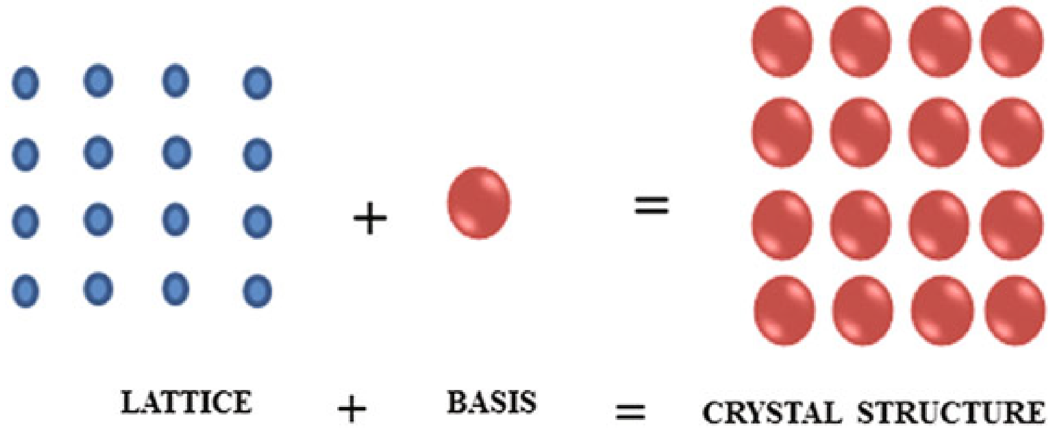

Figure 2.1: A Crystal structure formed by convolving a lattice and a basis. Copied from [9].

dimensions and 14 lattices in three dimensions shown in Table (2.1). The next important term is the Primitive unit cell which contains only one lattice point drawn at each corner and is labeled P. When it is translated through vectors $\vec{a_1}, \vec{a_2}$, $\vec{a_3}$ fills space without leaving gaps. So, the volume of the smallest unit cell is $\vec{a_1} \cdot \vec{a_2} \times \vec{a_3}$. Other unit cells contain more than one lattice point and are described below. In a *Body-centered* unit cell, a lattice point is present at each corner and at the center of the unit cell. Thereby carrying two lattice points in total and it is denoted by I. In a *Face-centred* unit cell, a lattice point is present in the middle of each face among a lattice at corners. Thus, containing four lattice points in total and it is labeled F. The last type is *Base-centred* which is also known by the names of *Side-centred* and *Basis-centred* and is denoted by C. In this type, a lattice point is present at the center of two opposite faces. It could be A-*face-centred*, B-*face-centred* and C-*face-centred*, if centred faces cut the a-axis, b-axis and c-axis respectively [2]. It is shown in the table (2.1) that the *Orthorhombic* system have all four types of unit cells and these are shown in the figure 2.2.

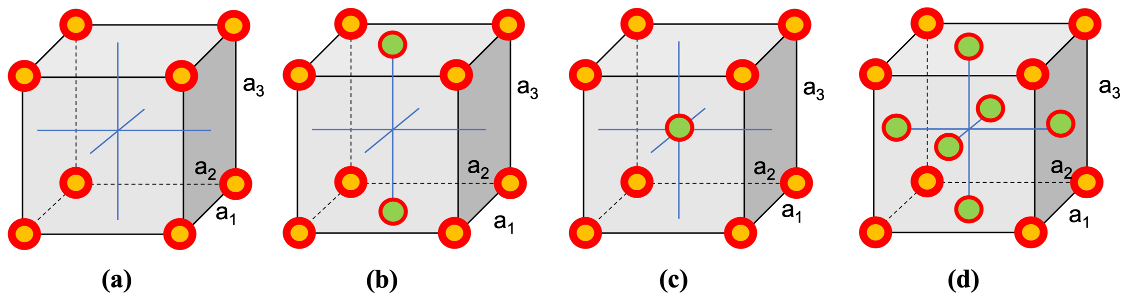

Figure 2.2: The four types of orthorhombic unit cells: (a) Simple or Primitive (P), (b) Base-centred (C), (c)Body-centred (I), and (d) Face-centred (F) are illustrated. Adapted from [2].

An interesting property of crystal lattices is that they can be plotted onto themselves by translations and other symmetry operations such as rotation, rotoinversions, and mirror reflections. In rotation

Table 2.1: Overview of the different crystal systems and their Braivais lattices. Obtained from [1].

System	Restriction on axes and angles	Number of lattices
Triclinic	$a_1 \neq a_2 \neq a_3$ $\alpha \neq \beta \neq \gamma$	1 (P)
Monoclinic	$a_1 \neq a_2 \neq a_3$ $\alpha = \gamma = 90° \neq \beta$	2 (P, C)
Orthorhombic	$a_1 \neq a_2 \neq a_3$ $\alpha = \beta\gamma = 90°$	4 (P, F, I, C)
Tetragonal	$a_1 = a_2 \neq a_3$ $\alpha = \beta = \gamma = 90°$	2 (P, I)
Cubic	$a_1 = a_2 = a_3$ $\alpha = \beta = \gamma = 90°$	3 (P, I, F)
Trigonal	$a_1 = a_2 = a_3$ $\alpha = \beta = \gamma < 120°, \neq 90°$	1 (P)
Hexagonal	$a_1 = a_2 \neq a_3$ $\alpha = \beta = 90°, \gamma = 120°$	1 (P)

symmetry, there is a rotation about an axis by an angle 360°/n that goes through the lattice point. Lattices are found to have one-, two-, three-, four-, five-, and sixfold rotation axes corresponding to n= 1, 2, 3, 4, and 6. In mirror reflections, a mirror plane is a plane that goes through a lattice point. In rotoinversions (a combination of rotation and inversion), rotation n is followed by inversion through an inversion center point. Point Group is a combination of different symmetry operations and there are 10 and 32 point groups in 2-D and 3-D respectively. These 32 point symmetry groups in three dimensions together with 14 Braivais lattice forms 230 different space groups. Out of 32 crystallographic point groups, 11 have a center of symmetry and no polarity, so they are not ferroelectric. While 21 are non-centrosymmetric out of which one has an inversion center making it centrosymmetric and remaining 20 display Piezoelectric effect. Out of these 20 classes, 10 have single polar axis and 10 are non-polar. 10 points groups with polar axis exhibit spontaneous polarization that depends on temperature and are called pyroelectrics. Ferroelectrics are part of pyroelectrics in which permanent polarization can be switched by applying external forces [11]. This classification of 32 crystal classes is shown in figure 2.3.

2.1.2 Index System for Crystal Planes

One can determine the orientation of crystal planes by three non-collinear points of a given Bravais lattice. These points are called *Miller Indices* and planes are denoted as (hkl). To index the plane in terms of Miller indices, the following rules are followed. Firstly, find the intercepts on the crystallographic axes in terms of the lattice vectors $\vec{a_1}$, $\vec{a_2}$, $\vec{a_3}$. Secondly, take the reciprocal of these three numbers and reduce them to the smallest set of integers such that they have the same ratio. These three integers, denoted by (hkl), gives the index of the plane or the set of parallel planes. As an example, for planes that intersect axes at 6, 2, 4 have reciprocals $\frac{1}{6}$, $\frac{1}{2}$, $\frac{1}{4}$, the smallest set of

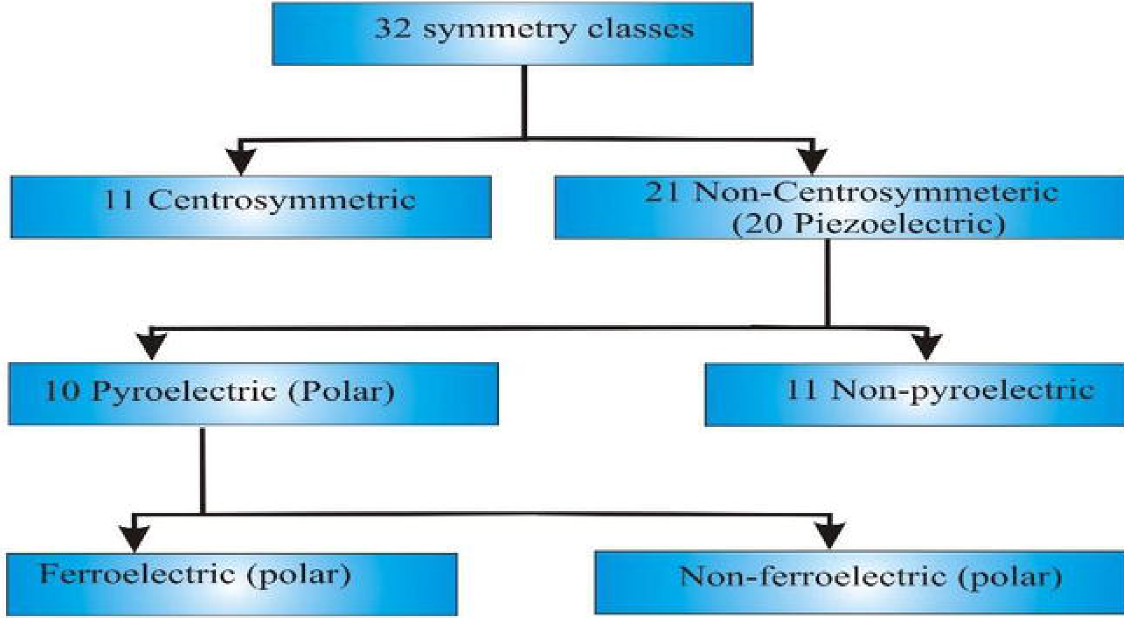

Figure 2.3: Classification of 32 symmetry classes or point groups on the basis of their ferroelectric, pyroelectric, and piezoelectric properties. Copied from [10].

integers having the same ratio are (263). Lattice planes that intersect the axis on the negative side of the origin, are indicated by the bar over the index, like $(2\bar{6}3)$. Also, if the plane is parallel to the axis or it does not intersect the axis, its reciprocal is 0. The interplanar spacing or the *d-spacing* between each lattice plane (hkl) can be calculated from lattice parameters a_1, a_2, a_3 as follows:

$$\frac{1}{d_{hkl}} = \pm\sqrt{\frac{h^2}{a_1^2} + \frac{k^2}{a_2^2} + \frac{l^2}{a_3^2}}. \tag{2.3}$$

The *d-spacing* defined by equation (2.3) is only for the crystal systems with right angles and for other crystal systems the expression for d is more complex. A certain set of planes parallel to the crystallographic direction is described as *zone* and the crystallographic direction is described as *zone axis* denoted by $[uvw]$. When zone axis $[uvw]$ is normal to the plane (hkl), then

$$hu + kv + lw = 0, \tag{2.4}$$

which is known as $Weiss\ zone\ law$.

2.1.3 Reciprocal Lattice

The reciprocal lattice is an essential concept to study crystal lattices and their diffraction properties. The primitive vectors of reciprocal lattice $\vec{a_1}^*, \vec{a_2}^*, \vec{a_3}^*$ can be defined in relation to primitive vectors

of crystal lattice $\vec{a_1}$, $\vec{a_2}$, $\vec{a_3}$ as follows:

$$\vec{a_1}^* = 2\pi\frac{\vec{a_2}\times\vec{a_3}}{\vec{a_1}.\vec{a_2}\times\vec{a_3}}; \vec{a_2}^* = 2\pi\frac{\vec{a_3}\times\vec{a_1}}{\vec{a_1}.\vec{a_2}\times\vec{a_3}}; \vec{a_3}^* = 2\pi\frac{\vec{a_1}\times\vec{a_2}}{\vec{a_1}.\vec{a_2}\times\vec{a_3}} \quad (2.5)$$

Each vector defined by (2.5) is perpendicular to the two axis vectors of the real space lattice. Hence, the generalized relation between $\vec{a_1}^*$, $\vec{a_2}^*$, $\vec{a_3}^*$ and $\vec{a_1}$, $\vec{a_2}$, $\vec{a_3}$ is described by,

$$\vec{a_i}^*.\vec{a_j} = 2\pi\delta_{ij} \quad (2.6)$$

Where δ_{ij} is Kronecker delta and $\delta_{ij} = 1$ if $i = j$ and zero otherwise.

The reciprocal lattice of the crystal is thus defined as the points spanned by set of vectors

$$\vec{G} = u_1^*\vec{a_1}^* + u_2^*\vec{a_2}^* + u_3^*\vec{a_3}^*, \quad (2.7)$$

Where $\vec{G}$ is called reciprocal lattice vector and $u_1^*, u_2^*, u_3^* \in \mathbb{Z}$. By performing the Fourier transform of a periodic function of the real space lattice, one can obtain another periodic function associated with the reciprocal space crystal lattice. By taking the inverse Fourier transform, it is also possible to go back to the real space lattice from the reciprocal space lattice. Therefore, the reciprocal lattice is useful in defining planes and the real crystal lattice is useful in defining directions. The reciprocal lattice vector that corresponds to the Miller indices (hkl) of a crystal is described by,

$$\vec{g}_{hkl} = h\vec{a_1}^* + k\vec{a_2}^* + l\vec{a_3}^* \quad (2.8)$$

The length $\vec{g}_{hkl}$ of the reciprocal lattice vector is associated with the d-spacing from equation(2.3) as follows:

$$||\vec{g}_{hkl}|| = \frac{2\pi}{d_{hkl}} \quad (2.9)$$

2.2 Ferroelectrics

2.2.1 Introduction to ferroelectric materials

The content of the following section is based on Tilley's [23], Olsen's [24], and Hole's [25] work, unless stated otherwise.

Ferroelectric materials possess an electric dipole moment which can be reversed with the help of an external electric field. As a result, switchable electric polarization is developed. Exposure to an electric field under appropriate conditions can result in a complete or partial realignment of spontaneous polarization. The change of polarization has certain requirements, of which most important is that the material is dielectric or insulator if not ohmic currents will be produced by applying an electric field. In the figure 2.4, it is shown that the ferroelectric materials are further part of the pyro-, piezo-, and dielectric materials. It is also clear from the figure that piezo-, and pyroelectric materials do not need to be ferroelectric, while a ferroelectric material is necessarily both pyroelectric and piezoelectric. So, in order to better understand ferroelectric materials, it is first important to look at di-, piezo-, and pyroelectric materials.

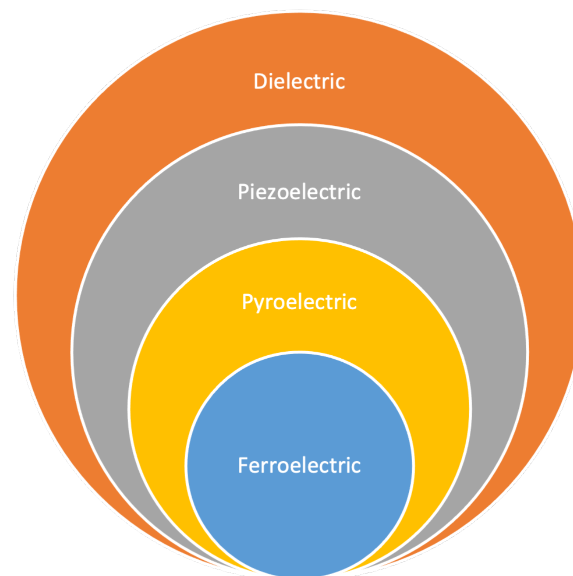

Figure 2.4: A Venn-diagram showing the relation between ferroelectric, pyroelectric, piezoelectric, and dielectric materials. Adapted from [24]

Like insulating materials, dielectric materials are poor conductors of electricity but they have a special property that on applying electric field, polarization is induced. The ability to polarize a material subjected to electric field is called relative permittivity. Piezoelectric materials fall under the category of dielectrics in which electric polarization occurs on the application of mechanical stress and this also works in reverse, such that an applied electric voltage induces mechanical stress

in the material. The latter is termed as the inverse piezoelectric effect. This direct relation between polarization and stress can be described by the following equation:

$$P = d\sigma \tag{2.10}$$

Where d is the piezoelectric coefficient, P is the induced polarization, and σ is the applied stress. The crystal structure of the material should be non-centrosymmetric such that the induced polarization cannot add pairwise to zero to give net zero polarization. Also, this effect is only present in single crystals because the random orientation of grains in polycrystalline material produces a net zero polarization.

Pyroelectric materials are piezoelectric materials that have spontaneous polarization – polarization in the absence of both an electric field and applied stress. Polarization in pyroelectric materials is temperature dependent and it decreases with increasing temperature until it vanishes above a certain temperature Tc. Tc is known as the Curie temperature and it represents the temperature for the phase transition between a paraelectric (above T_c) and pyroelectric or ferroelectric state (below T_c). A unique polar axis in addition to the non-centrosymmetric crystal structure (for piezoelectric) is required for the material to be pyroelectric. Spontaneous polarization is usually found along this unique polar axis. An example of phase transition in perovskite $BaTiO_3$ is shown in the figure 2.5. In (2.5(A)), $BaTiO_3$ has a cubic phase at high temperature and is paraelectric. When the temperature is decreased it changes from cubic to ferroelectric tetragonal phase with displacement of the Ti ion relative to the oxygen octahedron. In the ferroelectric phases, polarization is aligned in the direction of ion displacement. That is why polarization is upwards in figure 2.5B, and is downward in figure 2.5C.

Ferroelectric materials also have spontaneous polarization, but they are differentiated from pyroelectric for their ability to change the polarization by applying an electrical field in the opposite direction. An external electric field must overcome the already existing polarization first to switch the polarization. This results in a visible delay in the polarization compared to the external electric field and this delay results in the formation of a hysteresis loop, as shown in the figure 2.6. This is just the general shape of the hysteresis loop, the exact shape depends on the material. There are a few parameters that need to be clarified for understanding the hysteresis loop. i) The coercive field (E_c) is the minimum electric field required to switch the polarization. ii) The remanent polarization (P_r) is the amount of polarization that remains in the material after the electric field is removed. iii) Saturation Polarization (P_s) is the maximum amount of polarization that can be induced in the material. Now starting from the origin of the hysteresis loop in figure 2.6, here the

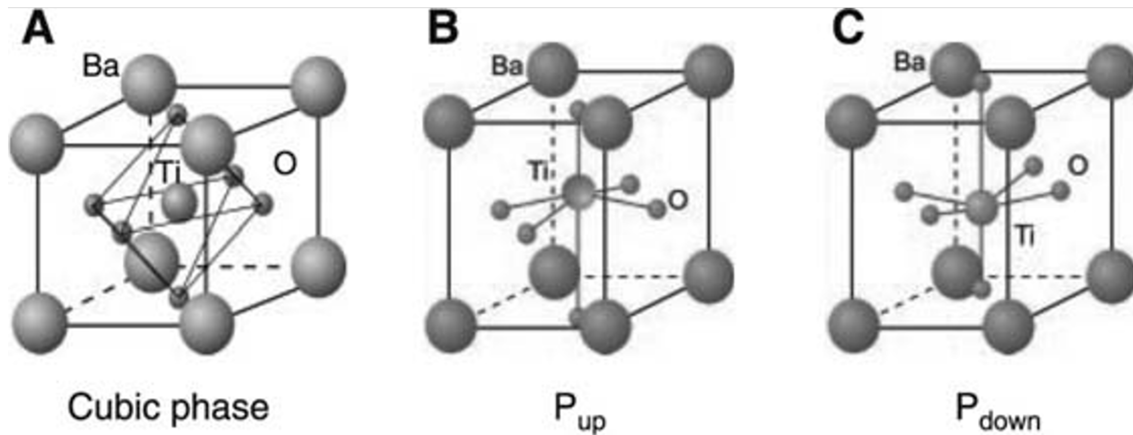

Figure 2.5: Illustration of displacive type phase transition in $BaTiO_3$. (A) Shows cubic phase and paraelectric state of $BaTiO_3$ when the temperature is above curie temperature. (B and C) Shows ferroelectric tetragonal phases below curie temperature with up and down polarization. Copied from [41].

polarization is zero due to the randomly oriented ferroelectric domains. When the electric field is increased, the domains will orient and align themselves in the direction of the applied field and reaches a saturation polarization (P_s) pointing upwards. This polarization will continue to increase linearly with the increasing electric field. When the intensity of the electric field is decreased, some of the domains can disorient and polarization within domains starts to decrease. When the value of the applied electric field reaches zero, some of the polarization remains in the domains which is called remanent polarization (P_r). Further decreasing the value of the electric field below zero or increasing it along the negative axis, will result in downward polarization of the domains. In this way, the ferroelectric polarization follows a hysteresis loop as a function of the applied electric field. Thus hysteresis loop is a fundamental feature of ferroelectric materials [26]. If the temperature T_c of the ferroelectric state increases above the upper limit, then the transition from ferroelectric to paraelectric occurs. In the paraelectric state, the polarization changes linearly with the electric field and hence no hysteresis is observed. Another interesting property of polycrystalline ferroelectrics is that the piezoelectric effect is present.

2.2.2 Applications of ferroelectrics

Ferroelectrics have numerous applications such as transducers, actuators, and sensors. As transducers, they can be used in SONAR arrays in ships or submarines and also in medical ultrasonic imaging because they can both produce and detect ultrasound waves. As actuators, these are utilized in inkjet printers and fuel injection systems. As pressure sensors, they are used in engines, tires of cars, and in the exploration of oil and gas. Due to high-temperature requirements, the number of materials that can be operational are less [24].

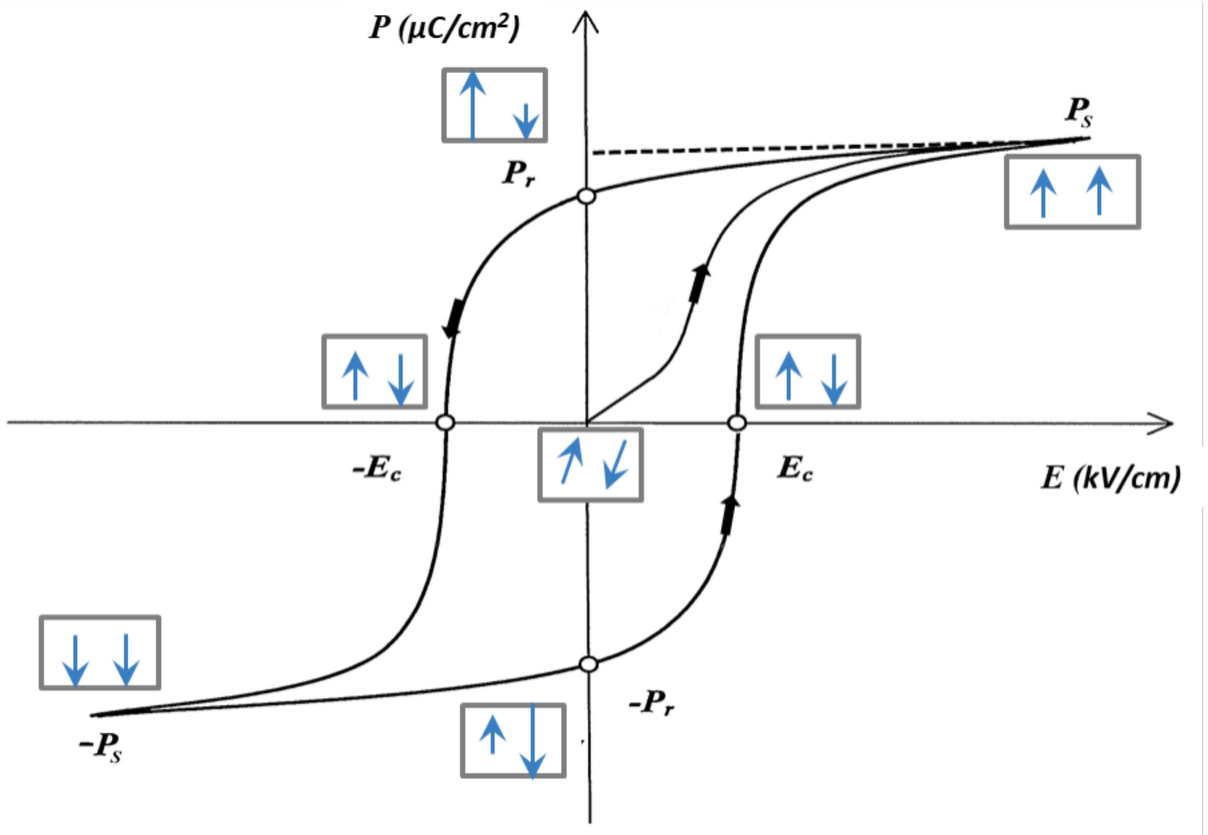

Figure 2.6: Typical hysteresis loop of a ferroelectric material below T_c which shows how the polarization and the orientation of domains are affected by the electric field. Copied from [26].

One of the major applications of ferroelectric materials is FeRAM (Ferroelectric Random Access Memory). Ferroelectricity is a practical engineering property, unlike pyroelectricity which possesses the symmetry property of crystals. The reason behind this is pyroelectrics break down electrically before reaching the coercive field [38]. FeRAM serves the same function as conventional flash memory, but it consumes less power and is faster in writing operations as well as has a greater number of write-erase cycles [38, 39, 40]. FeRAM is utilized in different applications such as electronic metering, automotive, printers, instrumentation, medical equipment, industrial microcontrollers, and radio frequency identification [40]. The principle behind the nonvolatile FeRAM is that polarization is reversed by the application of an external electric field [39]. The negative and positive remanent polarization represents the binary computational 0 and 1 [39]. The material remains polarized even if the external electric field is removed. That is why it is non-volatile memory. A typical FeRAM memory cell is shown in figure 2.7. The orientation of the dipole within the capacitor determines whether the polarization is positive or negative, and the orientation of the dipole can be reversed by applying a voltage across either line [40] as explained in section (2.2.1).

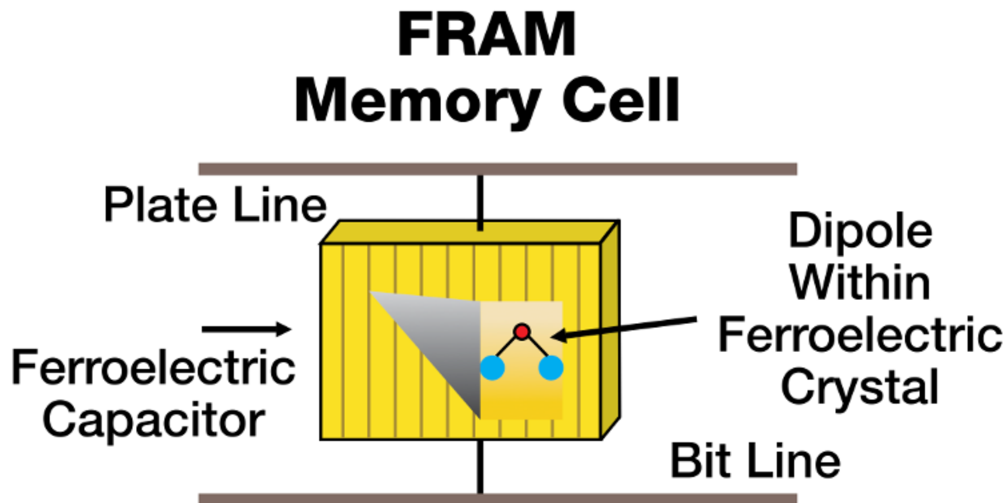

Figure 2.7: Schematic of Ferroelectric random access memory cell (FeRAM). Copied from [40].

2.3 About Strontium Barium Niobate (SBN)

It is important to know details about the material in order to understand the results obtained by transmission electron microscopy. In this project, the material studied is strontium barium niobate $Sr_xBa_{1-x}Nb_2O_6$ (SBN) and it is grown on a substrate called strontium titanate $SrTiO_3$ (STO). This section will give information on SBN, its structure, and ferroelectric properties.

2.3.1 Crystal structure of SBN

SBN is a broadly studied ferroelectric material due to its electro-optic and photorefractive applications [27]. SBN has a partially filled tetragonal tungsten bronze structure (TTB) which means that the structure contains mixed occupancy of cations and vacancies [24]. The TTB structure can be viewed as a perovskite structure, such that if the octahedra are slightly rotated in an ab-plane, the corner shearing octahedra forms perfect squares [24, 32]. The rotation of octahedra results in a unique polarization axis along the c-axis and several different cation sites are also introduced [24, 31]. Furthermore, the size of the unit cell is also increased by rotation which leads to the inclusion of ten octahedra instead of one as in the perovskite structure as shown in figure 2.8.

The O^{2-} anion in SBN and in most TTBs occupy the corners of the octahedra. While the spaces inside and between the octahedra are occupied by cations. There are a total of five different cation

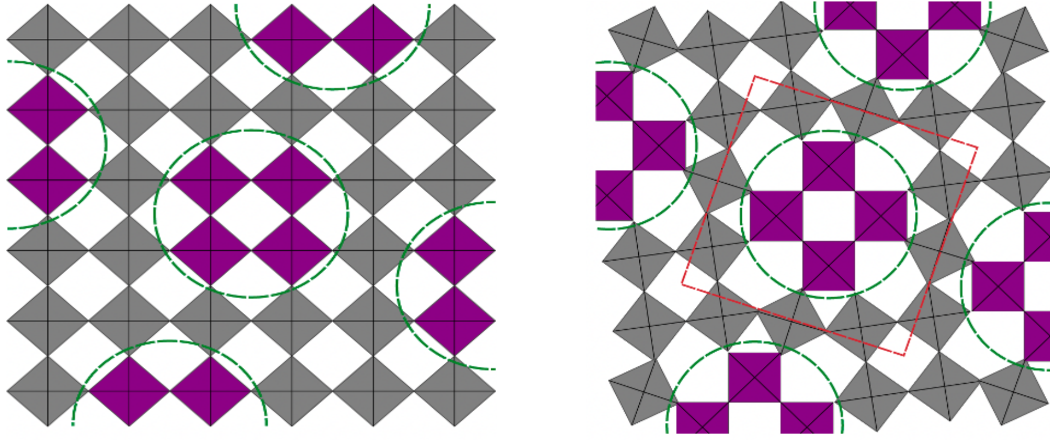

Figure 2.8: Sketch showing the relationship between perovskite and the TTB crystal structure. (a) The perovskite structure of corner-shearing BO_6 octahedra. The purple octahedra are rotated 45° to obtain the TTB structure. The green circles show the rotation areas. (b) The projection of TTB structure along the z-axis after rotation. The rotation areas are shown by the green line and the red line shows the unit cell. Copied from [25].

sites in the structure which are shown in the figure 2.9. The coordination number for the square A1 sites is 12, and for pentagonal A2 sites is 15. So, the A sites are relatively large. The C sites are small with a coordination number of 9 and it forms triangular channels through the structure. The B sites are distinguished by neighboring cation sites. A B1 octahedra contain two C sites and two A2 sites next to it, however, the B2 sites contain two A2 sites, one C site, and one A1 site next to it. The general chemical formula for TTB is $(A1, A2)(B1, B2)O_6$, where Sr and Ba normally occupy A sites and B sites are occupied by Nb in SBN [28]. It is also stated in several diffraction studies that the larger Ba-ions only reside on the A2 sites, while Sr-ions are distributed on both A1 and A2 sites. It is also mentioned in the literature that the C sites are empty and only some of the A sites are filled, explaining the partially filled TTB structure [27, 28, 29, 30].

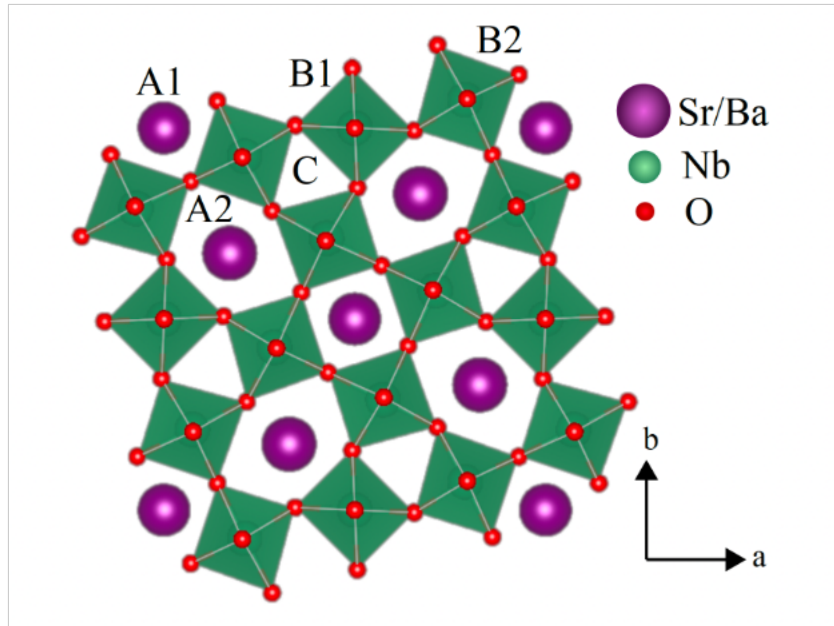

Figure 2.9: The TTB structure crystal structure of SBN projected along c-axis and showing different cation sites. O^{2-} (red atoms) are located on the corners of the octahedra with a B1 and B2 cation inside the octahedron (green Nb atom). The A1, A2, and C sites are outside the oxygen octahedra. The figure is copied from [25], and uses the crystal structure as found by [28].

2.3.2 Symmetry considerations and ferroelectric properties

A filled SBN structure belongs to the aristotype space group $P4/mbm$. However, the symmetry can be reduced by specific order due to the inherent vacancies in the unfilled SBN structure [24]. A mirror plane symmetry is present in the $P4/mbm$ space group which is perpendicular to the z-axis and thus does not allow any ion displacement along the z-direction, to maintain the symmetry. However, the ferroelectric state of SBN exhibits space group symmetry of $P4bm$. This is because of the displacement of the Nb-ions in the oxygen octahedra and displacement is mainly parallel to the z-axis that breaks the perpendicular mirror symmetry. Hence, the z-axis is the unique polarization axis in the TTB structure [28].

SBN undergoes a displacive type phase transition and it is an uniaxial ferroelectric [33]. The Curie temperature T_c for SBN ranges from $60-250°C$, depending linearly on the Sr: Ba molar ratio [16]. For higher Sr concentrations, T_c is the lowest [30]. A piezoelectric coefficient has been measured along the c-axis for a single crystal and is found to be $140pC/N$ and this value is among the largest values reported for pure SBN [34]. However, for doped SBN the value of the piezoelectric coefficient is reported up to $210pC/N$ at room temperature and these values are seen to increase with increasing temperature [34].

2.3.3 Relation between SBN and STO

The SBN thin film can be grown on substrates by both chemical and physical methods. These methods of growing thin films include an aqueous chemical solution deposition method [16], the use of polymer resin, and sol-gel synthesis with the use of a spin coating, pulsed laser deposition, and RF sputtering [25]. The thin films produced have structures ranging from polycrystalline with random orientation [35] to epitaxial and oriented [33], depending on the substrate and synthesis parameters used [16]. SBN thin films have been grown successfully on various substrates including STO(100) [25].

For the film to grow epitaxially it is important that the lattice mismatch between crystal structures of the substrate STO and SBN is relatively low such that the atoms are allowed to reside with proximity. The crystal structure of STO is simple cubic perovskite with the general formula ABO_3. A sites are occupied by Sr atoms at the corner, B sites are occupied by Ti atoms at the body centers, and O atoms are present at the face centres [43]. It is shown in figure 2.10.

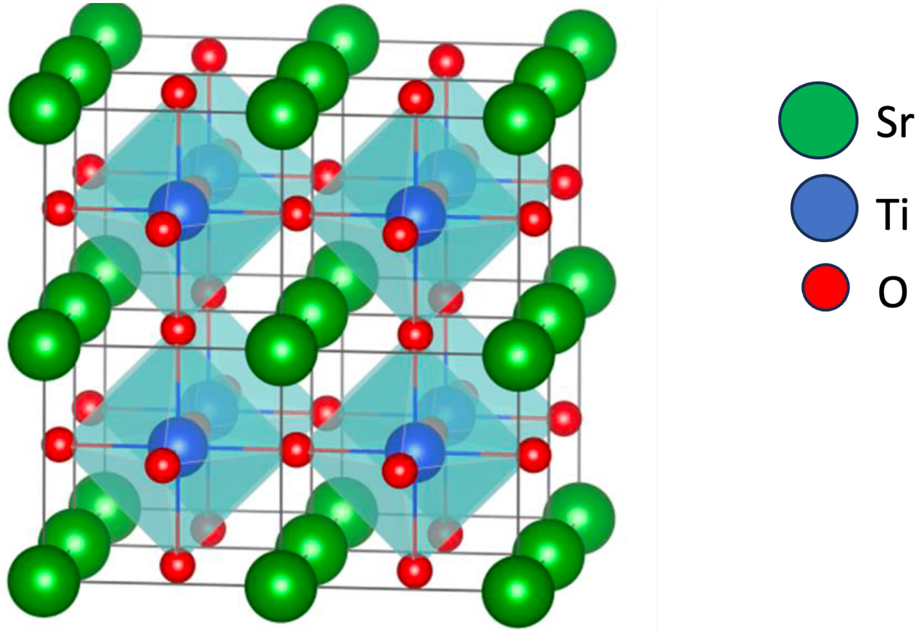

Figure 2.10: Visualization of Crystal Structure of Strontium Titanate (STO). It has a centrosymmetric perovskite structure with blue Ti atoms at the center of the octahedron formed by six O^{2-} anions. While Sr sits at the corners of the unit cell. Adapted from [42].

For most of the SBN thin films, the c-direction is oriented perpendicular to the substrate surface. However, an additional orientation with a c-direction parallel to the substrate surface is reported for STO 100 single-crystal substrate [36, 37]. The angle between the perpendicular c-orientation of SBN and a-b axis of the substrate is 18.4° as shown in figure 2.11a. The parallel orientation has the (310) or (130) orientation of SBN on the STO 100 surface as shown in figure 2.11b. It is

mentioned in paper [16] that the two orientations of the film SBN 001 and SBN 310 were observed on the STO 100 illustrated in figure 2.12. Both orientations can be achieved by several rotations of SBN on the substrate because both orientations correspond to a family of planes in SBN aligning with a family of directions in STO. There is a rotation of ±18.4° around the c-axis of SBN, parallel to the substrate surface, in the case of SBN 310. However, the c-axis here can also point in two equivalent directions, [100] or [010] direction of the substrate. SBN crystals on the other hand, for SBN 001 are rotated to ±18.4° around the c-axis of SBN, normal to the substrate surface [16].

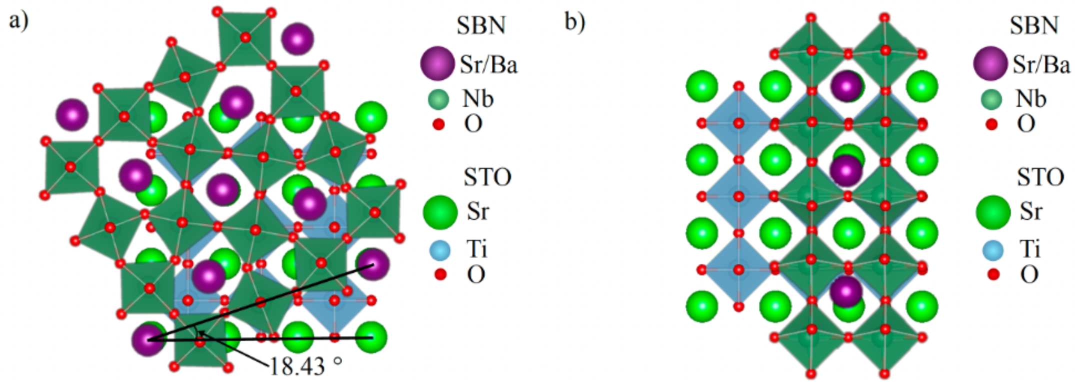

Figure 2.11: Schematic showing the lattice match between (100) oriented $SrTiO_3$ substrate and the SBN crystal structure. a) Illustrates the lattice alignment for the (001) orientation of SBN, where the unit cell is rotated ±18.4° with respect to the STO substrate. b) Illustrates orientation along the (310) plane. Figure copied from [25].

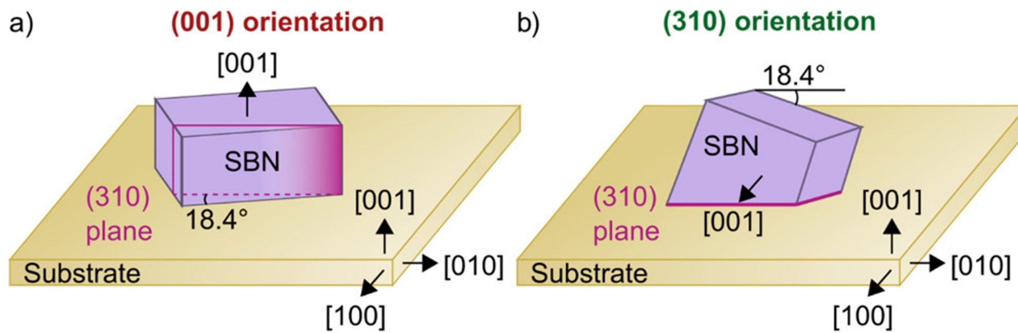

Figure 2.12: Illustration of (a) SBN 001 and (b) SBN 310 orientations on the STO 100 substrate. For the SBN 001 orientation, the [001] of SBN is normal to the surface of STO substrate and 310 planes in SBN are parallel to the [001] and [010] direction of STO. For SBN 310 orientation, the [001] of SBN is parallel to either the [100] 0r [010] direction of STO and one of the 310 planes in SBN is parallel to the STO surface. Copied from [16]

2.4 Transmission Electron Microscopy

Most of the content in this section is based on *Transmission Electron Microscopy*, a textbook by Williams and Carter [5], and is used as a reference throughout this section unless stated otherwise. Transmission Electron Microscopy (TEM) is an effective tool for providing detailed information on the structural and compositional properties of materials. That is why it plays an important role in the fields of science, education, and industry. Before the invention of Transmission Electron Microscopes in 1931, various other techniques already existed such as X-ray diffraction and Visible Light Microscopes (VLMs) to study materials. One of the main reasons to choose TEM over VLM is that a TEM offers a much higher spatial resolution. The reason behind this is, TEM as the name suggests uses electrons while VLM uses photons as a source.

The resolution of the limited by Rayleigh criterion which is given by,

$$\delta = \frac{0.61\lambda}{\mu sin\beta}, \tag{2.11}$$

Where δ is the smallest distance between two objects that can be resolved, λ is the wavelength of visible light, μ is the refractive index of the viewing medium, and β is referred to as semi collection angle of magnifying lens. Considering $\mu\ sin\beta = 1$, for simplicity, δ will be then half of the wavelength of light. For green light, having wavelength $550nm$, the resolution (δ) of VLM is about $300nm$ which is still much higher than the upper limit of the nano regime at $100nm$. It is clear that the smaller the wavelength, the better the resolving power.

Louis de Broglie proposed that an electron can behave both as a particle and a wave having its own wavelength and after his hypothesis, it was suggested to use electrons rather than visible light. The reason for selecting electrons over other particles was that electrons are charged particles and hence can be operated by Electromagnetic fields. The de Broglie wavelength λ of electrons in nm is given by

$$\lambda = \frac{1.22}{\sqrt{E}}. \tag{2.12}$$

It is clear from Equation (2.12) that the wavelength (λ) of electrons is inversely related to the accelerating voltage (E) of electrons and therefore increasing the accelerating voltage of electrons will decrease the wavelength of electrons which in turn can give us higher resolution. Thus, for electrons having an accelerating voltage of 200 kV, the wavelength will be 0.00251 nm, which means that TEM is able to resolve objects well below the Ångstrom scale, in accordance with equation (2.11). However, the resolution of the microscope is still limited because of the aberrations in the electromagnetic lenses. Apertures may also limit the resolution as they affect the semi-angle of

collection β.

2.4.1 Electron-matter interaction

Electrons interact strongly with matter because they are charged particles and Coulomb forces depend on charge. When electrons travel through the specimen in a TEM, several signals are generated as shown in figure 2.13. There are two important aspects that should be kept in mind while using TEM: i) the TEM specimen should be extremely thin, ii) the process of ionization. If the specimen is not thin enough, electrons will not be able to pass through it because electrons have low penetration depth. Electrons while traveling through the matter can remove another electron from the atoms and this is called ionization. In order to fill up the space of the removed electron, an electron can jump from a higher energy level to a lower energy level, and this results in the emission of X-rays which can be detected to determine the chemical composition.

The concept of electron scattering is very important for all types of electron microscopes. A scattering event can be defined as a collision between two objects. As an example, the collision between two electrons. Depending on the energy of the scattered electrons, scattering can be defined as elastic or inelastic. If the energy is conserved, scattering will be elastic, and if energy is not conserved, then it will be inelastic. Scattering can also be coherent (scattered electrons are in-phase), and incoherent (scattered electrons are out of phase). Generally, elastically scattered electrons are coherent, and inelastically scattered electrons are incoherent. When electrons are scattered by an angle less than 90°, it is called forward scattering, and they are scattered by an angle greater than 90°, it is called backscattering. Back-scattered electrons are used in scanning electron microscopy (SEM), while forward-scattered electrons are useful for TEM. Depending on the thickness of the specimen, there can be a single scattering event resulting in kinematical diffraction or there can be multiple scattering resulting in dynamical diffraction.

Electrons are one type of ionizing radiation and hence it produces a wide range of secondary signals some of these are shown in the figure 2.13. Different signals help to get useful information from the specimen. As an example, the direct beam is used to obtain a bright field (BF TEM) image and from elastically scattered electrons one can obtain a dark field (DF) image and electron diffraction patterns. Characteristic X-rays are used for energy-dispersive spectroscopy (EDS) and inelastically scattered electrons are used for electron energy loss spectroscopy (EELS). These techniques in TEM are discussed in detail in section 2.3.3. In the TEM, the term incident beam is commonly used for an incoming beam of electrons, and the term scattered beam is used for an outgoing signal after interaction with matter.

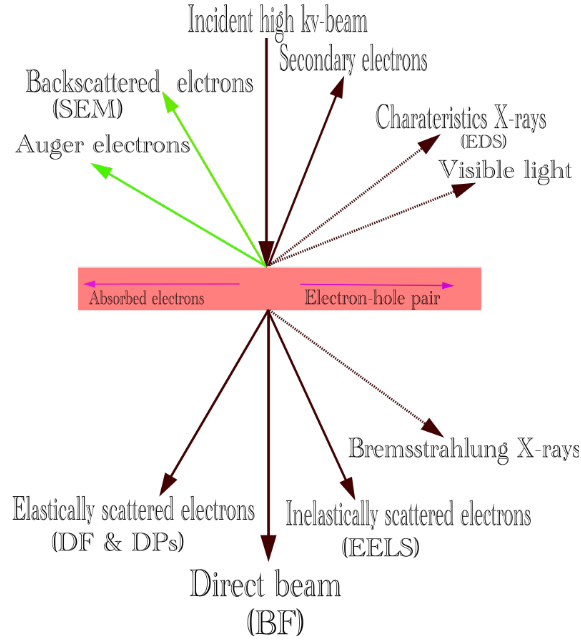

Figure 2.13: Schematic showing the different types of signals generated and corresponding TEM techniques when a high energy electron beam interacts with the TEM specimen. Adapted from [5]

The probability of an electron interacting with an atom in the material is determined by an *interaction cross-section*. It is denoted by σ and has units of area. For simplicity, let us first consider the cross-section of a single isolated atom and then it can be extended to the whole specimen. The scattering angle (θ) is the angle between the incident beam and the scattered beam and the electrons scattered by semi-angle θ end up in a region defined by solid angle Ω as shown in the figure 2.14. The relation between θ and Ω is as follows:

$$\Omega = 2\pi(1 - cos\theta), \tag{2.13}$$

where no scattering occurs when $\theta = 0$. On differentiating (2.13), one gets

$$d\Omega = 2\pi sin\theta d\theta. \tag{2.14}$$

In TEM, it is important to know whether or not electrons are scattered outside a particular scattering angle ie. they do not pass through the lens or they do not fall on the detector. To know this, one needs to find $differential$ *cross-section* ($d\sigma/d\Omega$) and it is described as the ratio of the total number of scattered particles that come out in solid angle $d\Omega$. In order to find the differential

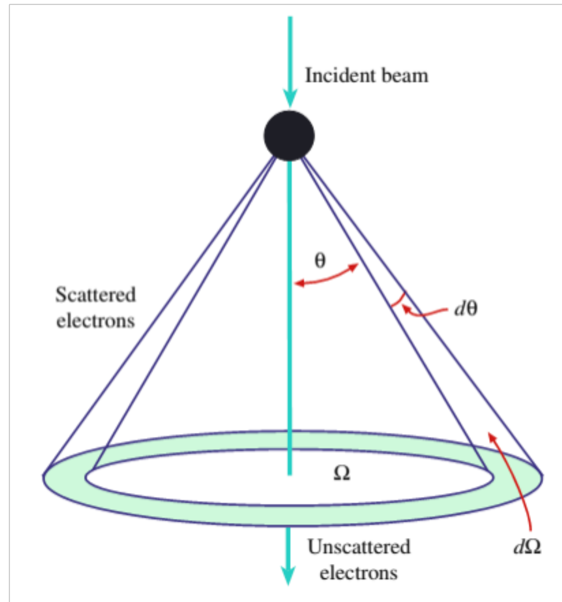

Figure 2.14: Scattering of an electron from a single isolated atom. θ is the scattering semi-angle and Ω is the solid angle. On increasing the scattering angle $d\theta$, solid angle $d\Omega$ will also increase. Copied from [5].

cross-section for a single atom, divide the equation (2.14) by $d\sigma$ on both sides and then reciprocate the equation as follows:

$$\frac{d\sigma}{d\Omega} = \frac{1}{2\pi sin\theta} \frac{d\sigma}{d\theta}. \tag{2.15}$$

Now, to calculate the cross-section for electrons that scatter away from θ, one can integrate equation (2.15) from θ to π,

$$\sigma_{atom} = \int_{\theta}^{\pi} d\sigma = 2\pi \int_{\theta}^{\pi} \frac{d\sigma}{d\Omega} sin\theta d\theta. \tag{2.16}$$

There can be a possibility that the electrons do not scatter at all or scatter at an angle close to θ=0 and in that case, limits of integration can be changed according to the type of scattering. It is clear from this integral that the scattering cross-section (σ) decreases as the scattering angle (θ) increases. Now, moving on to the specimen that contains N number of atoms per unit volume from a single atom case, the total cross-section is then given by,

$$\sigma_{total} = N\sigma_{atom} = \frac{N_0 \rho \sigma_{atom}}{A}, \tag{2.17}$$

where σ_{atom} is the scattering cross-section for a single atom, N_0 is Avogadro's number, A is the atomic weight of the atoms in the specimen and ρ is the density of the atoms. The specimen will also have some thickness t, which is important to take into account for the calculation of the probability of scattering p. Another term that should be kept in mind for finding probability is the mean free path which is described as the distance traveled by an electron inside the specimen

and is denoted by lambda (λ). Note that λ here is not the wavelength of the electron. So, the equation (2.17) turns out to be,

$$p = \frac{1}{\lambda} = t\sigma_{total} = \frac{N_0 \sigma_{atom}(\rho t)}{A}. \quad (2.18)$$

However, Rutherford described the differential cross-section, when an electron scatters through an angle θ by the nucleus of an atom in the specimen as follows:

$$\sigma_R(\theta) = \frac{e^4 Z^2}{16(4\pi\epsilon_0 E_0)^2} \frac{d\Omega}{sin^4 \frac{\theta}{2}}. \quad (2.19)$$

Where e is the charge of an electron, E_0 is the energy of the electrons in KeV, ϵ_0 is the dielectric constant, and all other terms are described earlier. This equation does not take into account the relativistic effects and assumes that the electrons scatter elastically. So, modifications have been made in the equation (2.19) and final expression looked as follows:

$$\sigma_R(\theta) = \frac{\lambda_R^4 Z^2}{64\pi^4 a_0^2} \frac{d\Omega}{[sin^2(\frac{\theta}{2}) + (\frac{\theta_0^2}{4})]^2}. \quad (2.20)$$

In above equation, λ_R is the relativistic wavelength of electron, a_0 is the Bohr radius of the scattering atom, and $\theta_0 = 0.117 Z^{1/3}/E_0^{1/2}$. Although this equation is screened and perfect for TEM calculations, it has some limitations for atoms having atomic numbers greater than 30 and for high operating voltages. In this situation, one should use equation (2.17) given by Mott and Massey. On integrating equation (2.20), one can calculate the total cross-section over a particular angular range.

When considering an electron as a wave, one needs to take into account the intensity of a scattered electron wave as the absolute square of the atomic form factor. The atomic form factor is described as the Fourier transform (FT) of the scattering electron. The general expression for X-ray scattering on an atom is given as:

$$f_x(\vec{K}) = \int_{-\infty}^{\infty} \rho(\vec{r}) e^{i\vec{K}.\vec{r}} d\vec{r}. \quad (2.21)$$

In equation (2.21), $\vec{K} = \vec{k_d} - \vec{k_i}$, is the transfer of wave vector $\vec{k_i}$ of the incoming wave and wave vector $\vec{k_d}$ of scattered wave and $\rho(\vec{r})$ is the density of electron in an atom as a function of position $\vec{r}$ from the nucleus. This atomic form factor f_x of X-rays can be related to that of electrons as follows:

$$f^B(\vec{K}) = \frac{me^2}{2\pi\hbar\epsilon_0} \left(\frac{Z - f_x(\vec{K})}{|| \vec{K} ||^2} \right). \quad (2.22)$$

Equation (2.22) is called the Mott-Bethe formula, where m and e are the mass and charge of an electron respectively, ϵ_0 is the permittivity of vacuum, and $\hbar$ is the Planck constant. The equation above is advantageous when electrons scatter on an isolated atom. However, in TEM the electrons get scattered by a group of atoms and as the wavelength of electrons is much smaller than the distance between the atoms, diffraction will take place. So, it will be discussed in the next section (2.4.2) how diffraction occurs in a crystal and the principle of diffraction.

2.4.2 Diffraction

This section is based on Charles Kittel's "Introduction to solid state physics" [1], unless stated otherwise.

Diffraction is defined as the spreading of a wave when it strikes an object or an aperture [12]. Diffraction of photons, neutrons, and electrons is helpful in studying the crystal structure and it depends on the wavelength of the incident beam and the crystal structure of the material. When the wavelength of the incident beam is comparable to that of visible light say 500 nm, the superposition of the waves scattered elastically by the individual atoms of the crystal result in ordinary refraction. However, if the wavelength of the incident beam is comparable to or smaller than the distance between the parallel planes of atoms, the outgoing beams can travel in different directions that are different from the incident direction. W. L. Bragg thus treated the parallel planes of atoms in a crystal as mirrors and gave an explanation about the diffracted beams from a crystal. In reflection by a mirror, the angle of incidence is equal to the angle of reflection. Assuming that the distance between parallel planes of atoms in a crystal is d_{hkl}, and the incoming beam is incident along the plane of the paper, the path difference between the reflected rays is $2d_{hkl}sin\theta$. This is illustrated in figure2.15a. One can detect the diffracted beams if the waves reflect and interfere constructively and constructive interference will only occur if the path difference equals an even number of wavelengths λ, yielding the $Bragg's\ law$

$$2d_{hkl}sin\theta_B = n\lambda. \tag{2.23}$$

This equation is valid for $\lambda \leq 2d_{hkl}$. To deal with 3-dimensional lattices, the Laue conditions are more general and easy to work with as compared to Bragg's law. If the wavevector of the incident beam is $\vec{k_i}$ and that of the outgoing beam is $\vec{k_d}$, then the difference between the two wavevectors is given by $\Delta\vec{k_i}$. This condition can be written as:

$$\vec{k_i} - \Delta\vec{k} = \vec{k_d}, \tag{2.24}$$

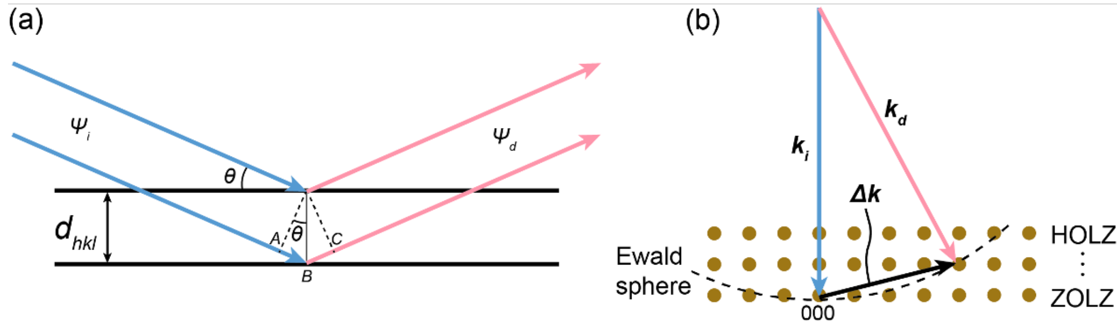

Figure 2.15: (a) Simplified description of Bragg's law. ψ_i is the incident wave which is reflected by planes separated by distance d_{hkl} and ψ_d is the scattered wave. θ is the angle of incident and path difference id given by $AB + BC$. (b) Illustration of a segment of the Ewald sphere in the reciprocal space. HOLZ and ZOLZ are indicated. Copied from [44].

where $\Delta\vec{k_i}$ is also referred to as the scattering vector. When this scattering vector $\Delta\vec{k_i}$ is equal to a particular reciprocal lattice vector $\vec{G}$ defined in equation (2.7), the Laue condition is satisfied.

$$\Delta\vec{k} = \vec{G}. \tag{2.25}$$

The equation (2.25), can be manifested in another way to give Laue equations. Taking the scalar product of both $\Delta\vec{k_i}$ and $\vec{G}$ with $\vec{a_1}, \vec{a_2}, \vec{a_3}$ and combining with equations (2.6) and (2.7)gives the Laue equations as follows:

$$\vec{a_1} \cdot \Delta\vec{k} = 2\pi h; \qquad \vec{a_2} \cdot \Delta\vec{k} = 2\pi k; \qquad \vec{a_3} \cdot \Delta\vec{k} = 2\pi l, \tag{2.26}$$

where h, k, l are the Miller indices that were introduced earlier. All three equations above show that $\Delta\vec{k}$ is located at a cone about $\vec{a_1}, \vec{a_2}, \vec{a_3}$ and thus $\Delta\vec{k}$ must meet all the three equations for the diffraction spot to intersect. This is only possible through systematic searching of the orientation of the crystal. The *Ewald sphere* is visualized in figure2.15b and this sphere helps to understand how diffraction occurs in the TEM. It gives a visual demonstration of when the Laue condition is satisfied. The Laue condition is fulfilled whenever the Ewald sphere intersects a reciprocal lattice point. The radius of this sphere in reciprocal space or the length of the wavevectors is given by $\mid \vec{k_d} \mid = \mid \vec{k_i} \mid = \mid \vec{k} \mid = 1/\lambda$, where λ is very small in electron diffraction which results in very large Ewald sphere and it can be considered as flat over local regions. Furthermore, because of the extremely thin TEM specimen, the reciprocal lattice points are elongated in the direction parallel to the direction of the beam, which gives them the shape of the rod and they are named *relrods* (abbreviation for reciprocal lattice rods). As a result, the diffraction conditions are fulfilled over an extended area in reciprocal space, giving rise 2-dimensional electron diffraction spot pattern on the detector. The sphere is drawn such that $\vec{k_i}$ is at 000 reciprocal lattice point. The zeroth-order Laue

zone (ZOLZ) is the one that contains this point. The planes parallel to ZOLZ and not containing 000, are the higher-order Laue zone (HOLZ) [44].

2.4.3 TEM Hardware and Imaging Techniques

A typical design for TEM instrument is shown in figure 2.16. A TEM is similar to a VLM, but instead of using visible light and glass lenses, it uses electrons and electromagnetic lenses. The instrument is designed as a vertical column that is kept under a vacuum and it can be divided into four components: the electron gun, the illumination system, the objective lens system, and the imaging system. These are described in the sections below.

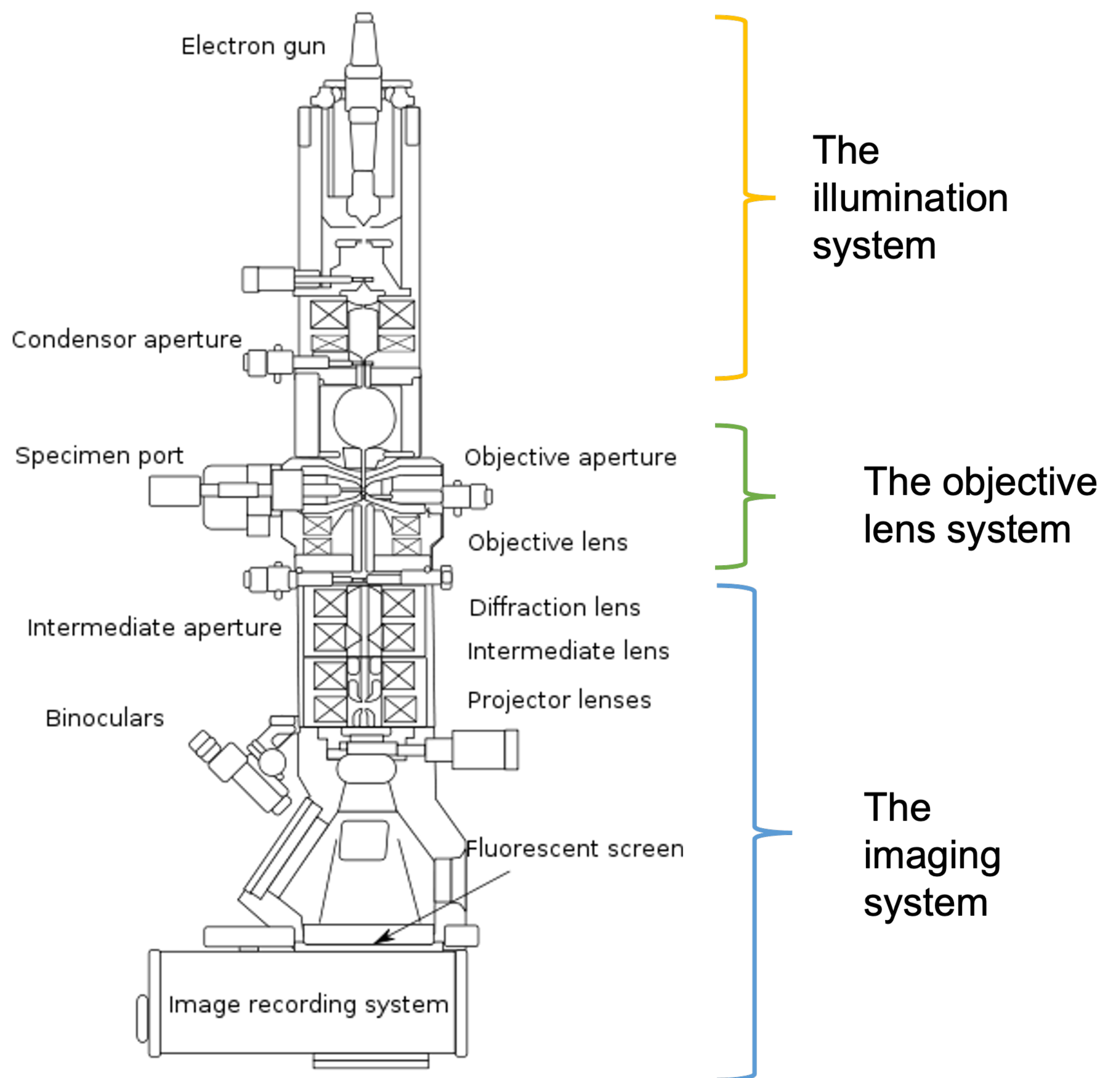

Figure 2.16: Simplified overview of a standard TEM. It consists of the illumination system, the objective system, the objective lens system, and the image recording system. Adapted from [5].

The Electron Gun

The electrons are emitted by an electron source called a 'gun' and these guns are of two types *thermionic* and *field−emission.* A thermionic gun consists of W (tungsten) or LaB_6 (Lanthanum Hexaboride) which is heated to a sufficient temperature to release electrons. The material is heated to give electrons sufficient energy to leak from the gun and overcome the barrier. This barrier is called the work function and ϕ and has typically a value of the order of a few eV. The current density J is related to the operating temperature T in Kelvin as follows:

$$J = AT^2 e^{-\frac{\phi}{kT}}. \quad (2.27)$$

This equation describes the physics behind thermionic emission and is known as Richardson's Law. In equation (2.27), A is Richardson's constant, and k is Boltzmann's constant. It is clear from the equation that the source needs to be heated to a temperature (T) in order to have energy greater than the work function ϕ so that it can release the electrons. The materials that are suitable for thermionic sources should have a high melting point or exceptionally low work function because some materials can melt or vaporize when provided with a few eV of thermal energy. In older TEMs, tungsten was being used because of its high melting point. However, the source used by modern TEMs is (LaB_6) which has a low work function.

Field-emission sources, also known as field-emission guns (FEGs) work differently from thermionic sources and use an electric field to produce electrons. It consists of a sharp tungsten needle and the principle behind FE is that the strength of the electric field increases at sharp points according to the following equation:

$$E = \frac{V}{r} \quad (2.28)$$

Where 'V' is the applied voltage and 'r' is the radius of the pointed source. So, the smaller the radius, the larger will be the electric field. Tungsten is fundamentally used as an FE source as it can be given a radius of $< 0.1\mu m$. By applying 1-kV potential tungsten tip of radius $0.1\mu m$, the electric field that is produced is $10^1 0V/m$, which in turn lowers the work function and electrons can overcome the barrier to escape from the tungsten. There are two types of FEG: (a) Cold FEGs (used in JEOL ARM200F) (b) thermionic-emission FEGs or Schottky emitters (used in JEOL JEM2100F, and on the SEM in FIB that is used for TEM sample preparation). Since the coherency of electrons is better in cold FEGs than in the thermionic source, the brightness (intensity per solid angle) is good and these are preferred when obtaining phase-contrast images. However, because of the sharp needle tip, FEGs are not able to image as large areas as TEM with thermionic guns. So, for amplitude-contrast imaging, thermionic guns are preferred.

The Illumination system

The electrons that are ejected by the electron source are then converted into a beam with the help of magnetic lenses, deflection coils, and apertures which makes up the illumination system. This beam of electrons is then transported to the specimen. This system also controls the parallelism of the beam of electrons and also the angle with which the beam enters the specimen ie. the convergence angle. For diffraction, Bright Field (BF TEM), and Dark Field (DF) imaging, the parallel beam is utilized. However, larger convergence angles are used in STEM and convergent beam electron diffraction (CBED). The condenser aperture in this system is used to select the electrons that one wants to interact with the specimen. Some electrons move away from the optic axis and are incoherent, and this aperture can also be used to reduce the number of incoherent electrons. In order to tilt the electron beam off the optic axis, deflectors are used. The pair of deflector coils can shift the beam while still keeping the beam parallel to the optic axis. The electromagnetic lenses in this system image only the gun crossover and parallel beam that hits the specimen.

The Objective lens system

The specimen inserted in the TEM sits in the objective system and it is the ground for image formation. The objective lens, the objective aperture (OA), and the specimen holder together makes up the *objective lens system*. The objective aperture decides which electrons will create the final image and is located at the back focal plane (BF TEMP) of the objective lens. This system plays an important role in TEM anatomy as the interaction between electron beam and specimen occurs here and images and diffraction patterns are also formed in this system. The quality of data collected about the specimen depends on the quality of the objective lens system. In the image plane of the objective lens and above the imaging system, a selected area aperture (SA) is located. The function is to select the area of the specimen and allow the electrons to pass from that area only.

The Imaging system

The objective system forms the intermediate image of the specimen and it is then passed to the imaging system. The imaging system consists of a diffraction lens (DL), an intermediate lens (IL), a projector lens (PL), a viewing screen and an image recording system. The purpose of diffraction and the intermediate lens is to magnify and focus real space image or the diffraction pattern formed by the objective lens in the BF TEM. The final real space image or the diffraction pattern is projected on the viewing screen or the image recording system with the help of projectors.

The depth of field is the measure of how much an object can be moved along the optic axis and still remains in focus and is given by $D_{ob} = d_{ob}/\beta_{ob}$. The depth of view is the measure of how much the detector can be moved along the optic axis and still record the focused image. It is given by $D_{im} = d_{ob}M_T^2/\beta_{ob}$. Here, d_{ob} is the resolution in the object, β_{ob} is the maximum angle of the beams emerging from the object, M_T is the transversal magnification of the system. The complete TEM specimen can be in focus at the same time because D_{ob} is usually in the order of tens or hundreds of nanometers. Also, detectors and cameras inside the TEM can be placed anywhere after the imaging system because d_{ob} is usually in the order of meters.

2.5 Imaging Techniques

As shown in figure 2.13 of Electron specimen interaction the interaction between an electron beam and specimen generates different signals. With the help of these signals, a TEM can be operated in various modes specialized to a particular signal and can help us analyze the different aspects of the sample micro-structure. This section will briefly explain the techniques that were used throughout the thesis. The content of this section is mainly based on [5] and [47], unless stated otherwise.

Obtaining contrast

Amplitude contrast and *Phase contrast* are the two types of contrasts that must be considered in TEM images. The contrasts occur when an incident beam of electrons scatters onto a sample, it can change both the amplitude and the phase of the electrons in the beam. The examples of amplitude contrast are Diffraction and mass-thickness and HRTEM is an example of phase contrast.

The amplitude contrast can be enhanced by inserting an objective aperture in the back focal plane of the objective system. One can choose to form an image by using only scattered or unscattered electrons. Figure 2.17b shows the image formed by inserting OA on the central spot of the diffraction pattern while figure 2.17a shows the image formed without inserting OA. These images clearly show that the contrast in the image can be improved by inserting OA. BF TEM image is formed when the objective aperture is centered at the unscattered beam. The intensity of the outgoing beam depends on the Z (atomic) number and thickness of the sample. If the thickness of the sample varies while the Z is the same, then areas with thicker regions will scatter more electrons and hence will appear as dark while thinner regions will scatter less electrons and will appear as bright. Similarly, in a flat specimen containing more than one element (having different Z), the areas with high Z will scatter more than areas with low Z numbers. As a result, areas with high Z number will be dark and the ones with low Z will be bright. As both Z and thickness contribute to the contrast in the image, that is why it is called mass-thickness contrast.

Areas in the sample that diffract more than other areas also appear darker, which leads to the conclusion that the orientation of the crystal will also affect the BF TEM images. This type of contrast is called diffraction contrast. This can be understood from the difference in figure 2.18a and figure 2.18b. Figure 2.18a is taken when the substrate is perfectly on zone while figure 2.18b is obtained after tilting the crystal direction by +18.4°. In figure 2.18a, the grains marked 1 and 2 are darker as compared to the ones in figure 2.18b.

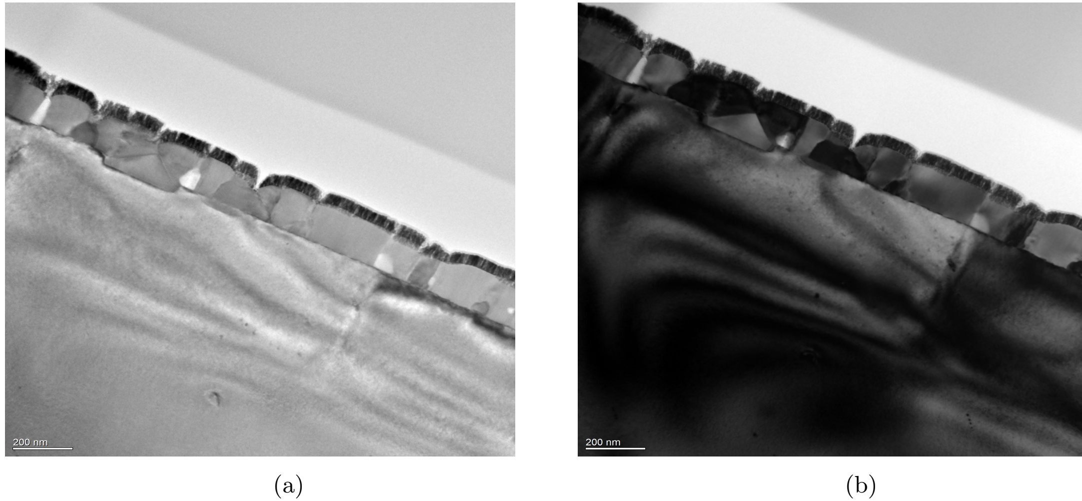

(a) (b)

Figure 2.17: Illustration of contrast mechanism in BF TEM images. (a) Shows the BF TEM image taken without inserting OA and hence contrast in this image is poor. (b) Shows the BF TEM taken with OA which leads to better contrast.

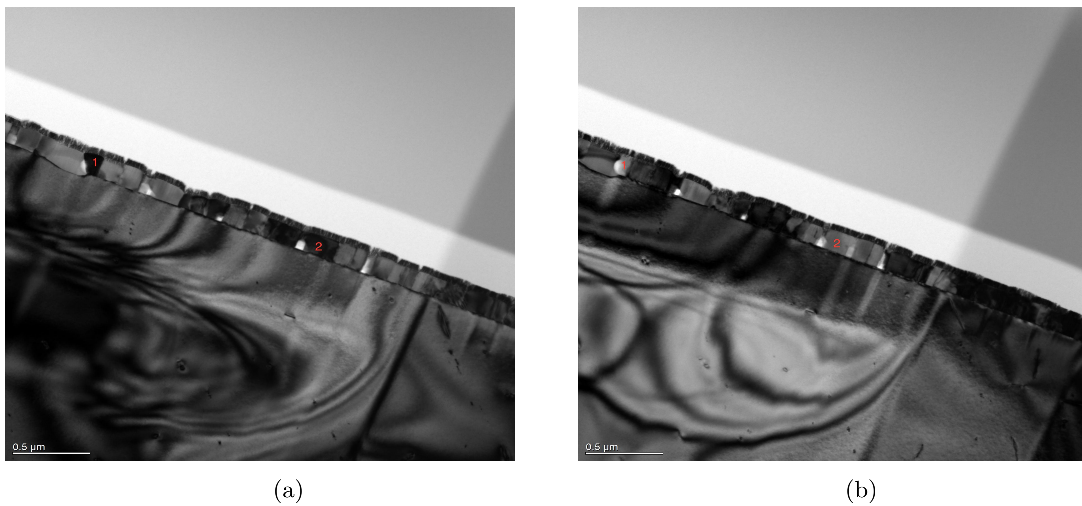

(a) (b)

Figure 2.18: Illustration of how tilting affects the diffraction contrast in the BF TEM image. (a) Shows the BF TEM obtained on zone (b) Shows the BF TEM obtained after tilting +18.4°. The difference in contrast can be understood by looking at the grains marked 1 and 2.

The procedure to obtain a BF TEM image is simple. One needs to start by selecting the selected area aperture and then going into the diffraction mode, so that the selected area diffraction pattern is formed. The DP consists of spots in which the central spot which represents the direct beam is

selected by inserting an OA on that spot. This OA is inserted into the BF TEMP of the objective lens, and it will block out the other spots in the DP. After centering the OA around a bright central spot, remove the selected area aperture and return to image mode. An illustration of the beam path followed during the formation of BF TEM images is shown in figure 2.19.

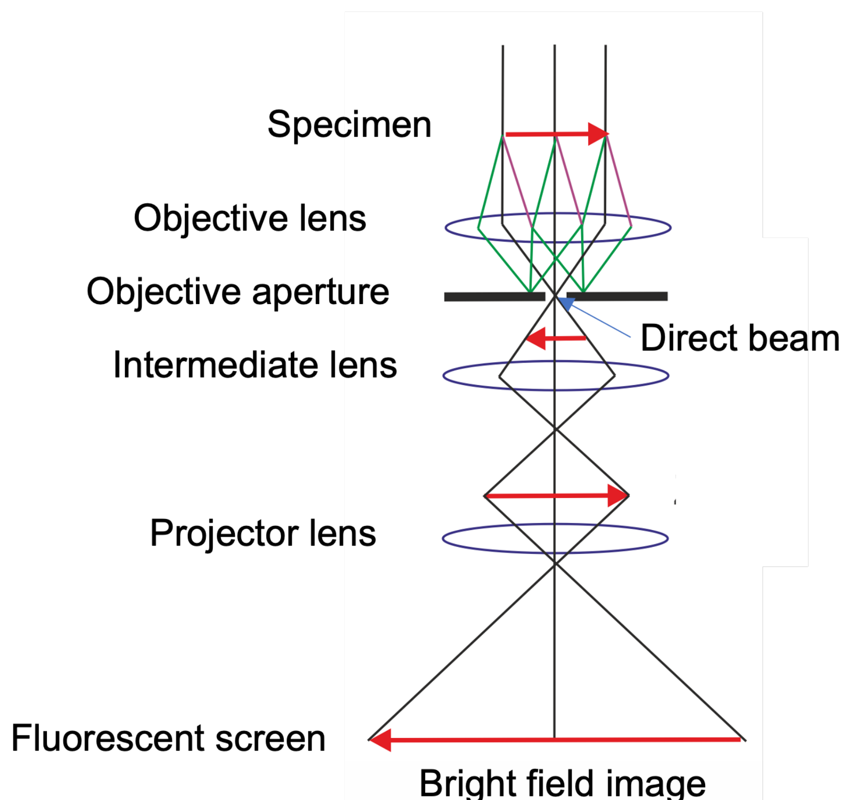

Figure 2.19: Simplified schematic of a path followed by electron beam while obtaining BF TEM iamge. Adapted from [5]

Dark Field imaging

Dark field (DF) TEM images are created by placing an objective aperture on one (or a few) of the scattered electrons rather than direct beam of electrons. This is similar to obtaining BF TEM image but instead of selecting a direct electron beam, a diffracted beam is selected. There are two methods to do it. The first one is that the OA can be placed on the dark area between the central spot and other bright spots in SAD mode to block the direct beam and allow the diffracted beam to pass through. After returning to the image mode from the SAD mode, the resulting image will be DF image. The second method is to tilt the incoming electron beam by an angle equal and opposite to the scattering angle which is 2θ and keep the OA in one place. This will give the impression that Diffraction Pattern has shifted in the SAD mode such that the OA covers an area that contains diffracted spots. The second method is preferred because the electrons that are off-axis are affected more by aberrations and astigmatism than the on-axis electrons. An example

of how the beam path looks when applying tilting is shown in the figure 2.20.

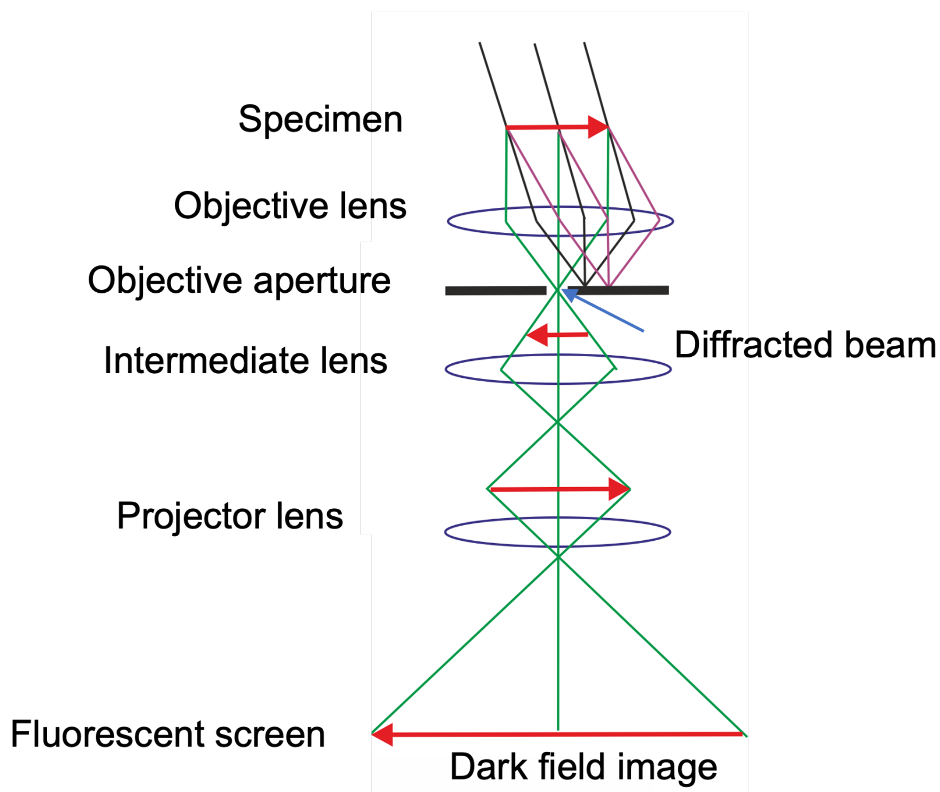

Figure 2.20: Simplified schematic of a path followed by electron beam while obtaining DF image. Adapted from [5]

The main reason for the contrast in DF imaging is diffraction contrast, similar to BF TEM imaging but the contrast is reversed in this case. The areas that look bright in BF TEM become dark in the DF image if all spots except the direct beam are included in OA.

Selected Area Electron Diffraction

Selected Area electron diffraction is one of the most useful techniques in the TEM and this is also used the most for this project. The reason behind this is that a DP can give information about the crystal structure, orientation of the grains, and much more. TEM has the ability to switch between *image mode* and $diffraction\ mode$ with just one click. When the object plane of the intermediate lens is the image plane of the Objective lens, then TEM is in the image mode and the image obtained is projected onto the fluorescent screen or camera. When the object plane of the IL is the back focal plane of the OL, then TEM is in the diffraction mode. The DP obtained is also shown on the camera or on screen. To obtain the selected area electron diffraction pattern, a parallel beam of electrons is utilized. The procedure starts with the insertion of the selected area aperture to select the desired area of the specimen from which one wants to obtain a DP, and this aperture is centered on the optic axis. After adding the selected area aperture, spread the beam

to the maximum to have as parallel beam as possible, and then chose the selected area diffraction mode. Figure 2.21 shows the path followed by the electron beam while obtaining a DP which appears on the screen. One can also change the focus of the DP with the help of diffraction-focus controls.

An amorphous specimen gives a DP in the form of rings, while a crystalline specimen in SAED mode gives a DP with spots referred to as reflections. Figure 2.22 shows an example of a selected area electron DP. Each spot in the DP is characterized by Miller indices *hkl* and corresponding lattice points in reciprocal space. As described earlier in the section the radius of the Ewald sphere depends on the wavelength of the incoming electron beam. Due to the very small wavelength of electrons, the Ewald sphere becomes very large compared to the distance between neighboring reciprocal lattice points which in turn results in multiple visible points in the DP produced on the screen.

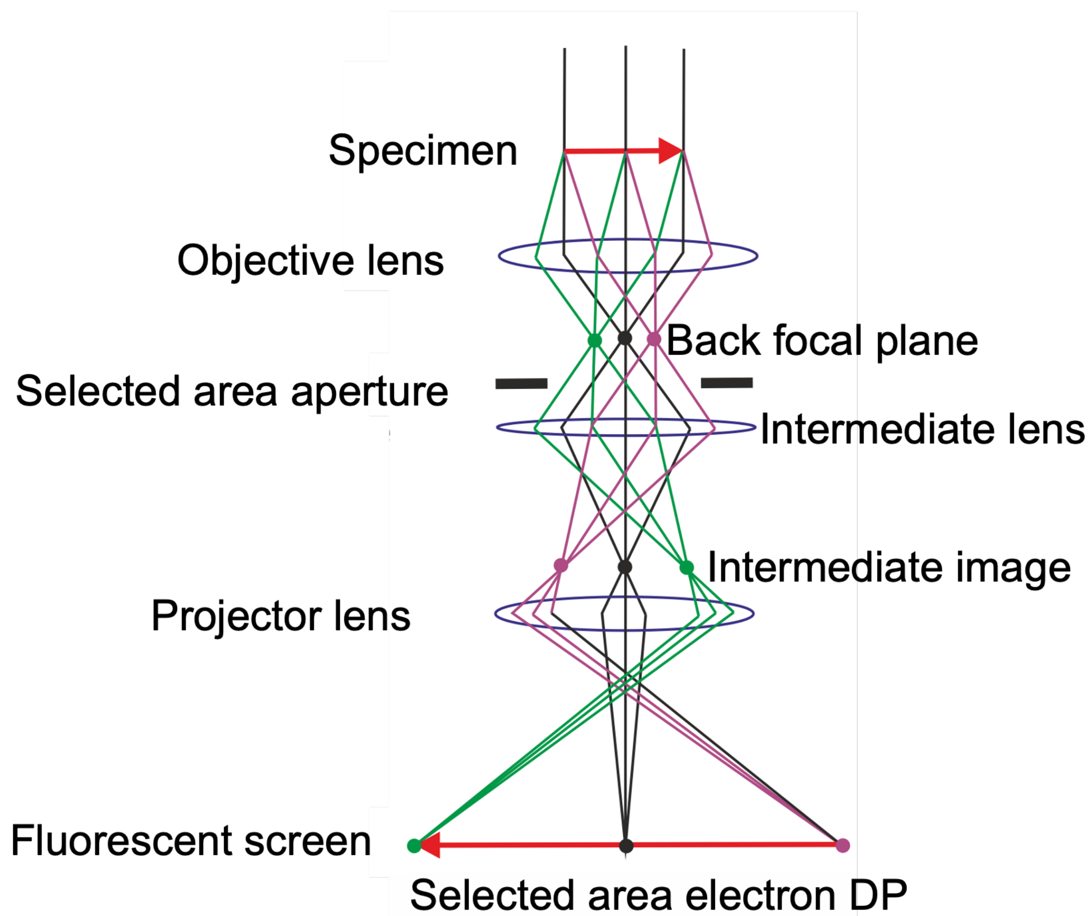

Figure 2.21: Simplified schematic of a path followed by the electron beam in SAED mode. Adapted from [5]

As the DPs fulfill Bragg's law and are projection of the reciprocal space lattice, these are dependent on the structure of the crystal and the orientation of the grains. Hence, grains with different

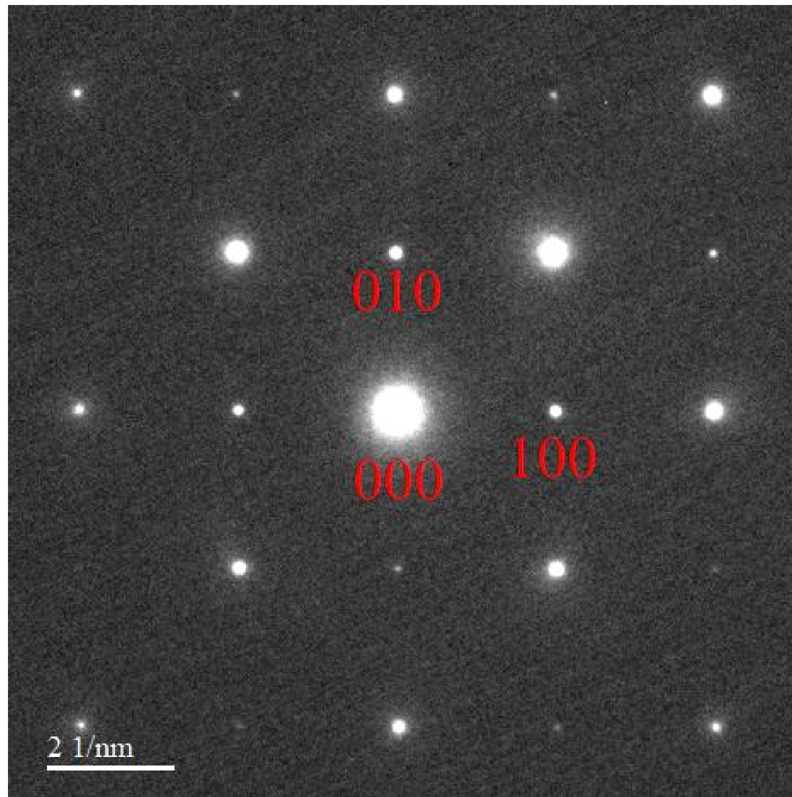

Figure 2.22: Example of a SAED pattern from a substrate strontium titanate (STO) at the [001] zone axis.

orientations produce different types of DPs. Selected area diffraction patterns (SADP) are useful for selecting the spots used for BF TEM or DF imaging.

STEM

Among all other imaging techniques in TEM, Scanning Transmission Electron Microscopy (STEM) is one of the most effective techniques. In STEM, the objective lens system is replaced by an electron detector. The lenses are adjusted such that the incoming beam becomes narrow, and cone-shaped. This forms a probe and on scanning this probe across the specimen, convergent beam electron diffraction (CBED) patterns are formed for each probe position. The symmetries in the crystal affect the CBED patterns. The STEM image is formed pixel by pixel with the help of this probe with a few tens of milliradians beam convergence. The STEM images are not affected by the defects in the lenses in the imaging and objective system. The quality of the probe depends on the quality of the condenser lens system because the probe is formed by this system. So, the resolution in the final image also depends on the condenser lens system and hence on the size of the probe. A TEM with FEG based illumination system is a better option for obtaining STEM images. One important thing to be kept in mind is that like other Scanning microscopy techniques, STEM only focus on the surface of the specimen when the depth of focus in STEM is quite low.

Furthermore, another important fact is that even though only the surface is in focus, the beam does not spread too much when it passes through the specimen and the reason behind this is the incoming beam of electrons gets channeled by the atomic columns. Also, the magnification in STEM is determined by the distance between the pixels across the scanned region and the number of pixels in the image, which means that the magnification is determined by the field of view. However, magnification is not necessarily proportional to the spatial resolution of the image.

HAADF STEM

For compositional and structural analysis of the specimen, Atomically resolved high-angle annular dark field (HAADF) STEM is one of the most powerful imaging techniques [48]. A STEM detector detects the intensity of selected areas in the CBED pattern. The detector sends the signals and where the intensity of a pixel corresponds to the probe location of the specimen, these signals are converted into an image. Depending on the range of the scattering angles of the transmitted electrons detected by the detector, the STEM detector is divided into BF TEM, ADF, and HAADF detectors [48]. Figure(2.23) shows a simplified version of this. The electrons that are scattered incoherently and elastically at large angles are detected by HAADF detector. Rutherford scattering given by the following equation is helpful in understanding the scattering of electrons at high angles.

$$\frac{d\sigma}{d\Omega} = \frac{Z^2 e^4}{16 E_0^2 sin^4(\theta/2)}, \tag{2.29}$$

Here $(d\sigma/d\Omega)$ is the differential scattering cross-section, e is the electron charge, E_0 is the kinetic energy of the incident electron, Z is the atomic number, and θ is the total scattering angle [13]. The heavier element will scatter more, as it is clear from the equation that probability of scattering is proportional to the square of the atomic number Z. Due to dependence on the Z number, the HAADF is also known as *Z-contrast imaging.* On summing the intensities of the electrons scattered by individual atoms in the specimen, HAADF-STEM images are formed. Thermal diffuse scattering is also included. When the spacing between atomic columns in the specimen is larger than the probe size, each atomic column is illuminated consecutively when the probe scans over the specimen. HAADF-STEM is less sensitive for materials with low Z because the intensity of each column in the map depends on the average atomic number z of the atoms in the column. The only drawback of HAADF-STEM is the possibility of specimen contamination or beam damage because of the high intensity of incoming electrons scanning over an area for a long period of time [13].

Energy Dispersive Spectroscopy

Energy dispersive spectroscopy (EDS) is a powerful technique that helps to find the elemental

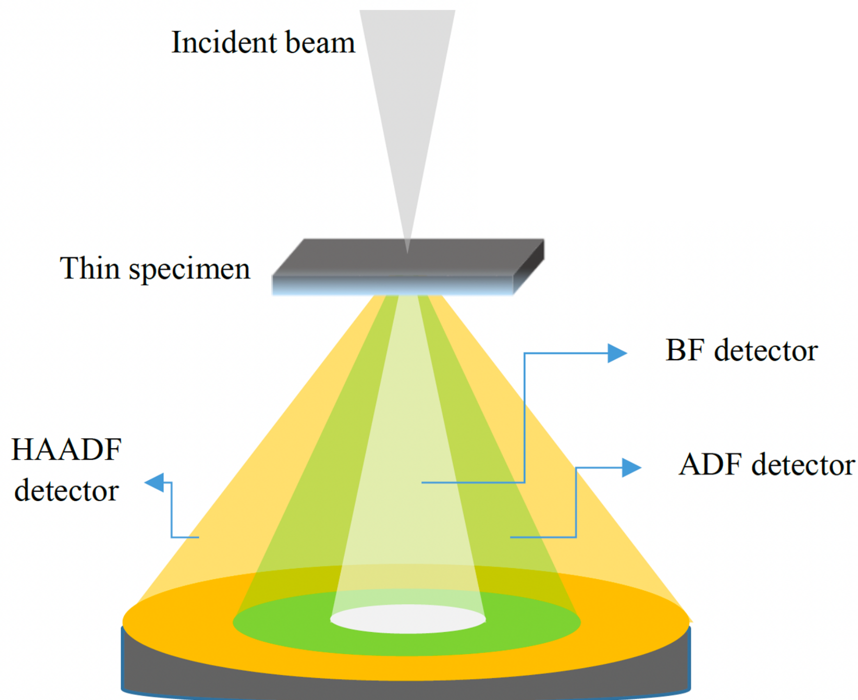

Figure 2.23: Simplified schematic of a STEM setup including a bright field (BF TEM), annular dark field (ADF), and high angle annular dark field (HAADF) detector. Copied from [49].

composition of the specimen. The basic principle behind this is when an atom in the specimen is stroked by a high-energy electron, it gets illuminated and internal excitations within the atom may occur. The electron that has been excited leaves a hole and this hole is filled up with the electron from the high-energy shells, resulting in the release of an x-ray having a certain amount of energy. These x-rays have different energies which can be detected by inserting an energy-dispersive detector close to the sample. The data can be acquired in two ways. First, one can operate the TEM in regular imaging mode and obtain energy-dispersive spectra from large areas. Second, one operate the TEM in STEM mode and obtain a spatial map of the chemical composition of the sample. There are tables that contain experimental data on the allowed transitions for elements $3-95$. One such table by Centre for X-ray optics [6], contains experimental data on the allowed transitions for elements 3-95 and can be used to index EDS.

Electron Energy loss spectroscopy

When an electron beam interacts with the specimen, it generates a number of signals as discussed in section (2.4.1). Some of the incoming electrons lose their energy after interacting with the specimen resulting in inelastic scattering of electrons. The energy lost by these electrons gives information about the chemical and structural properties of the specimen in the form of a spectrum called

electron energy loss spectrum [45, 46]. Many TEMs have been fitted with an electron spectrometer that forms an energy-loss spectrum from electrons passing through the sample. The EEL spectrum can provide information about the chemical and crystallographic structure of the specimen down to the atomic level [45]. The EELS spectrum can be divided into two regions: low-loss and high-loss [5]. The low-loss spectrum contains the zero-loss peak (ZLP) which arises from the electrons that do not lose their energy [44]. The high-loss spectrum contains the ionization edges, which are obtained as a result of excitation of the inner shell electrons [44]. XEDS and EELS are complementary to each other and most Analytical electron microscopes nowadays are equipped with both kinds of spectrometers [5].

3 Experimental Methods

This section briefly presents the synthesis of the thin films analyzed followed by a detailed description of the sample preparations before the techniques used in the TEM. Finally, the processing of data that was collected is discussed.

3.1 Chemical Solution Deposition

The material studied in this master project is strontium barium niobate ($Sr_xBa_{1-x}Nb_2O_6$) thin films grown on (001) oriented strontium titanate ($SrTiO_3$) substrate. The thin films were synthesized at the Department of Material Science and Engineering, NTNU, by Ph.D. candidate Viviann Hole Pedersen. As the synthesis of the thin films is not the focus of this project, a brief introduction to the deposition technique used will be presented and the reader can refer to the [16] for details on film growth.

To prepare oxide thin films aqueous chemical solution deposition (CSD) method was used which is an environment-friendly method. This technique uses a liquid precursor and heat treatments to form thin films. Precursor solutions of Sr and Ba precursors were prepared according to the method given in [17], and the Nb precursor solution was prepared according to the method given in [18]. The preparation of Sr, Ba, and Nb was performed using strontium niobate (Sigma-Aldrich, >90%), barium niobate (Sigma-Aldrich, 99.999%), and Ammonium niobate (v) oxalate hydrate (Aldrich chemistry, 99.99%) as precursors and Ethylenediaminetetraacetic acid (Sigma-Aldrich, >98.5%), citric acid (Sigma-Aldrich, 99.0%), and DL-malic acid (Sigma-Aldrich, >90%) as complexing agents. Details on the preparation method used can be found in [16, 17, 18]. After preparing Sr, Ba, and Nb solutions separately, a stable aqueous precursor solution was prepared by mixing the solutions in stoichiometric amounts to obtain a Sr:Ba:Nb ratio of 40:60:200, which was referred to as SBN40. This solution was used to make samples SBN 001 and SBN 310 based on the orientation and had a concentration of 0.07128M SBN.

After the preparation of the solution, the thin films were made through five cycles of deposition followed by pyrolysis and annealing, which builds the film samples layer by layer. An illustration of the cycle is given in figure 3.1. Two different orientations of the film were expected based on the heating rate and the termination of STO. The SBN 001 sample was prepared on a SrO terminated substrate while the SBN 310 sample was prepared on a TiO_2 terminated substrate. To prepare the two different substrate orientations, both substrates were cleaned for 5 minutes in acetone followed by ethanol in an ultrasound bath at 80°C prior to further treatment. Additionally, both

substrates were annealed at a high temperature of 1050°C for 1 hour in a tube furnace in a pure O_2 atmosphere to give an atomically flat surface [14]. To obtain the SrO termination, based on findings from [20], one substrate was O_2 plasma cleaned for 5 minutes directly before thin film deposition. For the TiO_2 terminated substrate, an additional etching step in deionized water was added. The substrate was etched for 30 minutes in an 80°C ultrasound bath before O_2 annealing and again for 5 minutes after annealing [14]. Finally, the TiO_2 terminated substrate was heated to 550°C for 2 minutes in air prior to thin film deposition to promote adhesion. The precursor solution of SBN was filtered through a 0.2µm filter upon deposition on the substrate and subsequently spin coated at 3500rpm for the 30s. Spin coating is a technique of depositing thin liquid solutions onto a flat surface rapidly. The substrate on which the solution is to be deposited is placed on a fixed but rotating platform and then precursor solution is added onto it. The substrate is rotated at a very high speed which helps the solution to deposit uniformly on it by the centrifugal force [7].

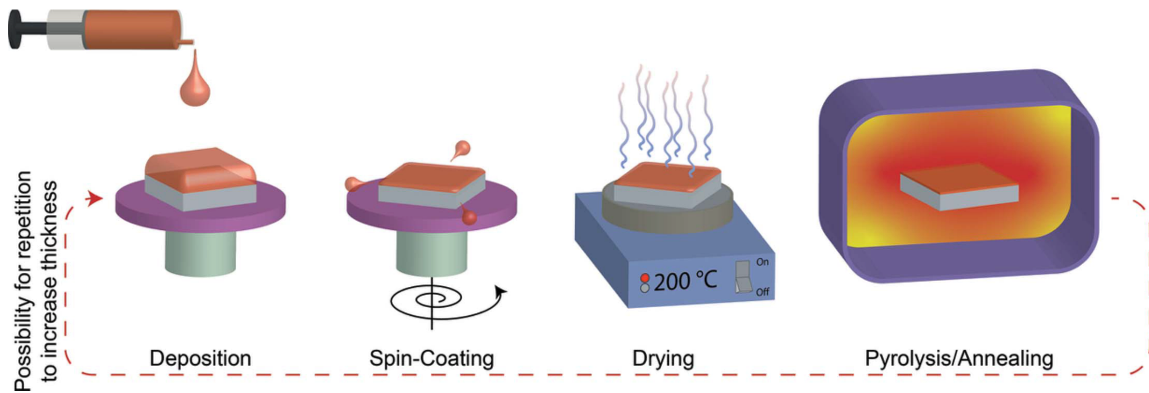

Figure 3.1: Figure shows the different steps followed in the typical CSD method. The red line indicates that one must repeat the process in order to increase the thickness of the film. Copied from [15]

.

After spin coating, the film was dried for 4 minutes at 200°C on a hot plate followed by pyrolysis and annealing. Pyrolysis and annealing play an important role in the crystallization of the film. Pyrolysis is the decomposition of the material by heating in the absence of oxygen [21], and annealing is referred to as heat treatment that can alter the physical and chemical properties. As an example, annealing can increase the strength and reduce the ductility by reducing the interactions between dislocations [19]. Since the orientation of SBN depends on the heating rates, the two samples were crystallized using different heating rates. SBN 001 was heated to 900°C (pyrolysis + annealing) at the rate of 0.04°C/second and held for 30 minutes before cooling to ambient temperature with a rate of 100°C/minute. The other sample SBN 310 was heated at the rate of 100°C/min upto 600°C (pyrolysis) and held at this temperature for 5 minutes. After this, it was heated to 1000°C (annealing) at the rate of 20°C and held for 45 seconds. Cooling was then performed at the same rate as SBN 001. The process of deposition and pyrolysis was repeated five

times until the desired thickness was achieved for each sample.

3.2 Focussed Ion Beam (FIB) sample preparation

FIB TEM samples were prepared with a $Helios\ G4\ UX\ dual-beam$ instrument from $Thermo\ Fisher\ Scientific$ at NTNU $NanoLab$. FIB is an advanced technique and it requires much experience and training to operate and handle properly. Therefore, the author did not prepare the FIB samples. The specimens used in the project were made by Senior Researcher at SINTEF Industry and associate Professor II at NTNU, Per Erik Vullum. Since the functioning of FIB is not the focus of this study, it will not be discussed in detail. However, there are some aspects of this technique relevant to this project and those will be discussed.

The FEI system's Dual Beam technology together with SEM (Scanning electron microscope) analysis and FIB milling are able to obtain ultra-thin TEM specimens. Due to the poor electrical conductivity of the SrTiO3 substrate and the SBN films, all samples were coated by a thin layer (typically 20 – 30 nm thick) of Pt-Pd (ratio 80:20) by using a Cressington sputter coater prior to FIB preparation. The first part of the protection layer was made by electron beam-assisted deposition to make sure that Ga could not damage the upper part of the SBN films. The upper and major part of the carbon protection layer was made by ion beam-assisted deposition. Approximately 2µm thick and 10µm long TEM lamellae were cut out and transferred to dedicated Cu TEM half-grids by standard lift-out procedures, using a tungsten "Easylift" micromanipulator. All coarse thinning was done with 30 kV acceleration voltage for the Ga+ ions. Final thinning was performed at 5 kV and then 2 kV on either size of the lamellae to minimize surface damage. The TEM lamellae had a final thickness typically in the range 50 – 100 nm.

3.3 TEM operations

To study the ferroelectric thin films, two different TEMs were used: JEOL JEM-2100 and JEOL JEM-ARM200F. Both instruments were operated at 200kV. The JEOL JEM-2100 is quipped with LaB_6 thermionic electron source and JEOL JEM-ARM200F is equipped with cold FEG. JEOL JEM-2100 has a Gatan 2k Orius CCD camera with *Gatan Digital Micrograph* software [22] and it was used mainly to obtain BF TEM images and SADPs. The BF TEM images were taken to have an overview of the whole sample. SADPs were taken from all the grains of both samples with the same camera length in order to compare d-spacing and lattice parameters and primarily to find the crystallographic orientation of the SBN grains. The JEOL JEM-ARM200F is double spherical aberration corrected and was operated by Per Erik Vullum. It was used to obtain HAADF images,

EELS and EDS elemental maps, and line profiles of all three different orientations from SBN 001. HAADF-STEM images were obtained using a Gatan ADF detector. EDS and EEls were performed simultaneously in STEM mode. The EDS signal was detected with a $100mm^2$ Centurio detector, covering a solid angle of 0.98 sr (steradian). EEL spectroscopy was acquired with GIF Quantum ER in dual EELS mode, using 1ev/channel(2048 channels in total), with a 67mrad semi-collection angle into the spectrometer and 21 mrad (milliradian) semi-convergence angle of the beam. High-resolution spectroscopy maps were further acquired with 61 pA beam current, $0.3\mathring{A} \times 0.3\mathring{A}$ pixel size, and 0.01s dwell time per pixel.

3.4 ReciPro Simulations of Diffraction Patterns

In order to understand the results, there is a need to do some simulations with recipro but before looking at the simulations, it is first important to know what is actually the meaning of in-plane and out-of-plane orientation or polarization. As mentioned in section (2.3.2) polarization is along the unique c-axis of the TTB structure, which means that one needs to know the direction of the c-axis in order to know whether the polarization is in-plane or out-of-plane. When the c-axis is parallel to the interface between the SBN film and STO substrate, then it is in-plane and when the c-axis is perpendicular to the interface, then it is out-of-plane. It is shown in figure 3.2. In terms of DP, for the c-axis to be in the plane the DP will show the ab plane of the film and it should be comparatively denser than that of STO, and for the c-axis to be out-of-plane, the reflection marked as red in figure 3.3, should be 001. Also, the horizontal line of reflections in DP represents the in-plane direction (orange line) and the vertical line of reflections (blue line) represents the out-of-plane direction.

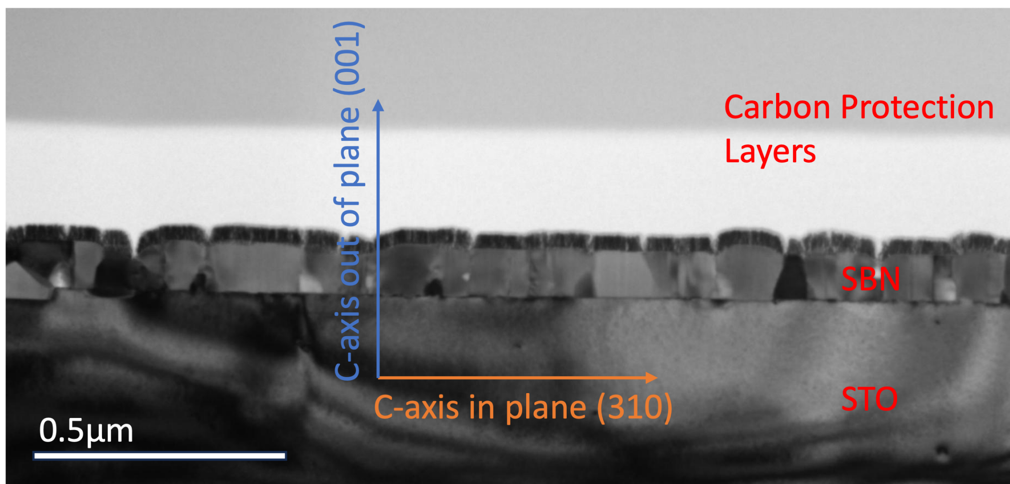

Figure 3.2: Illustration of in-plane and out-of-plane c-axis. The orange line that is parallel to the interface between the SBN film and STO substrate represents the in-plane direction and the blue line normal to the orange line represents the out-of-plane direction.

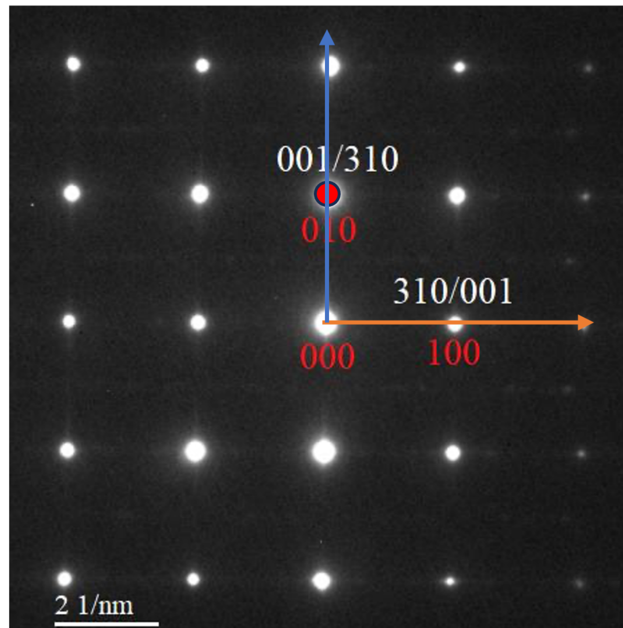

Figure 3.3: Illustrattion of in-plane and out-of-plane direction of c-axis in terms of DP. The orange line represents the in-plane and the blue line represents the out-of-plane c-axis. The blue line is to be preserved while performing tilting.

In order to confirm the out-of-plane orientation, the recipro software was used to look at the DPs at a particular zone axis. Figure 5.1 shows the diffraction pattern of SBN when (a) it is oriented to the (310) zone axis (b) it is tilted $+18.4°$ from (310) (c) it is tilted $-18.4°$. As explained earlier in this section that for out-of-plane polarization, the Bragg reflection along the out-of-plane direction should be 001, which is the case here. So, in this way, one can differentiate between 310 and 001 reflections and hence know the polarization direction. However, in DP 3.4c, it can be noticed that it does not reach any high symmetry zone axis after tilting $-18.4°$. Then another simulation was done. SBN was oriented to [130] zone axis and gave DP as shown in 3.5a. Again tilting of $\pm 18.4°$ away from [130] was performed. It was then noticed that the tilting [130] by $-18.4°$, reaches [100] zone axis as shown in 3.5c. However, tilting by $+18.4°$ gave us DP that is away from the high symmetry zone axis, as shown in 3.5b. Therefore, to find the polarization direction, one needs to tilt in both directions.

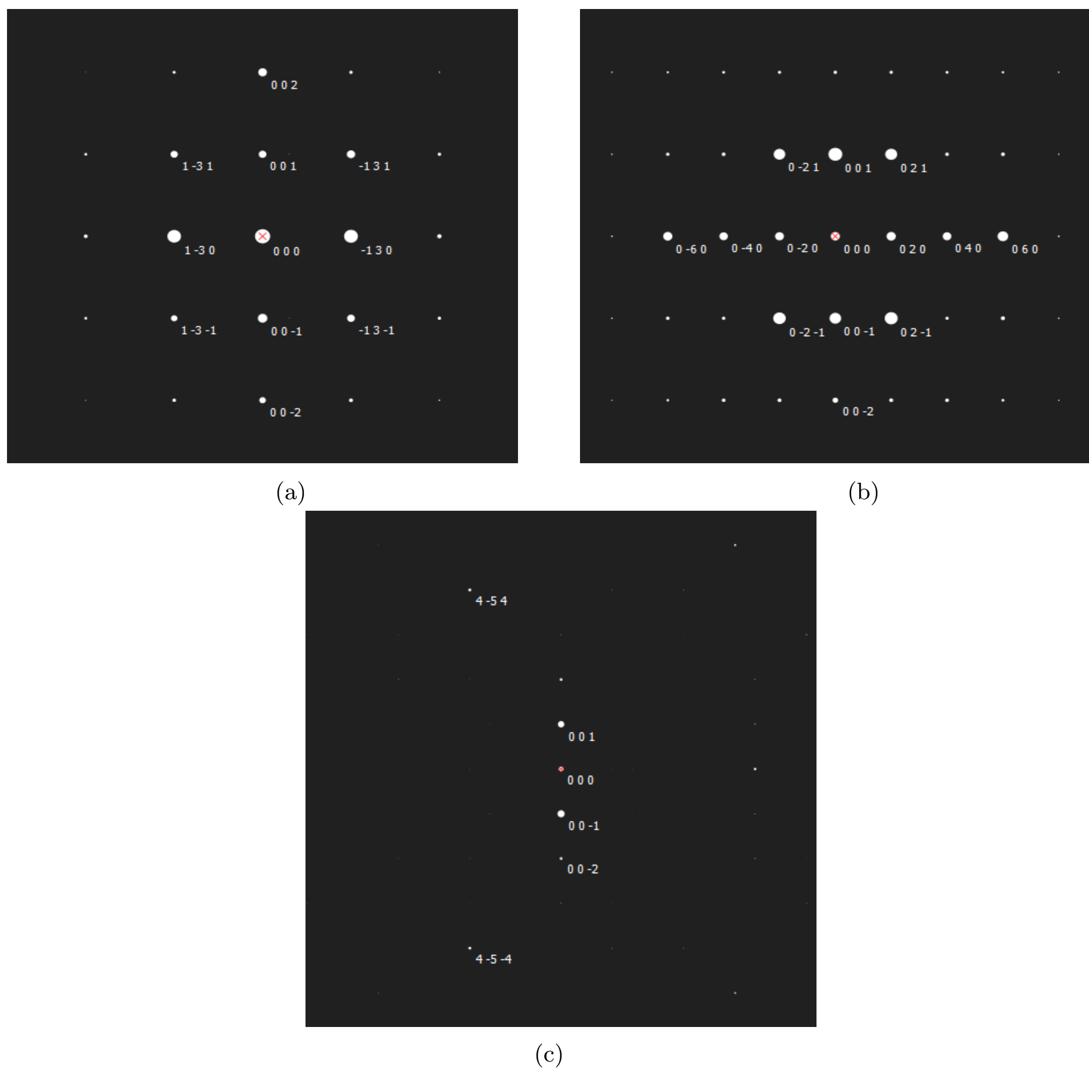

Figure 3.4: Illustration of how to confirm out-of-plane orientation using ReciPro simulations of DPs. (a) DP of SBN on [310] zone axis. (b) DP of SBN when it is tilted +18.4° and it is clear that the [001] or c-axis points in out-pf-plane direction. (c) DP of SBN when it is tilted −18.4° and it does not reach any high symmetry zone axis. Made with [58].

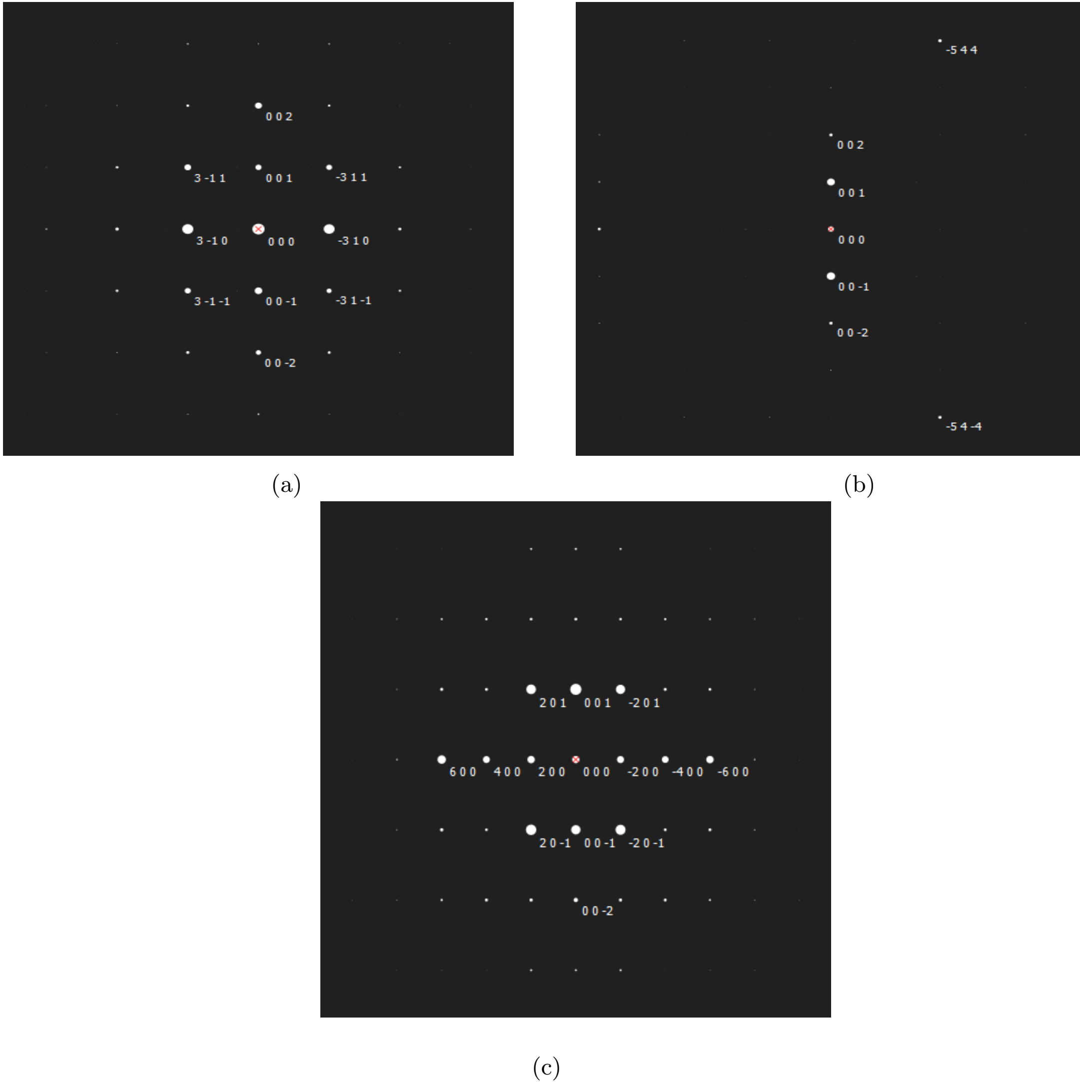

(c)

Figure 3.5: Illustration of how to confirm out-of-plane orientation using ReciPro simulations of DPs. (a) DP of SBN on [130] zone axis. (b)DP of SBN when it is tilted +18.4 and it does not reach any high symmetry zone axis (c) DP of SBN when it is tilted −18.4° and it is clear that the [001] or c-axis points in an out-of-plane direction. Made with [58].

4 Results

In this section, the results from the characterization of the two SBN samples are presented. Additional data are presented in the appendix. First, the BF TEM and HRTEM images are included which show the microstructure of the thin film. Then SADPs from selected grains are presented which helps in understanding the crystal orientation. Finally, HAADF STEM images, elemental maps from EELS and EDS data, and lines profiles taken by Per Erik Vullum using the JEOL JEM-ARM200F are presented. The discussion of the results is done in the section (5).

4.1 Thin Film Microstructure

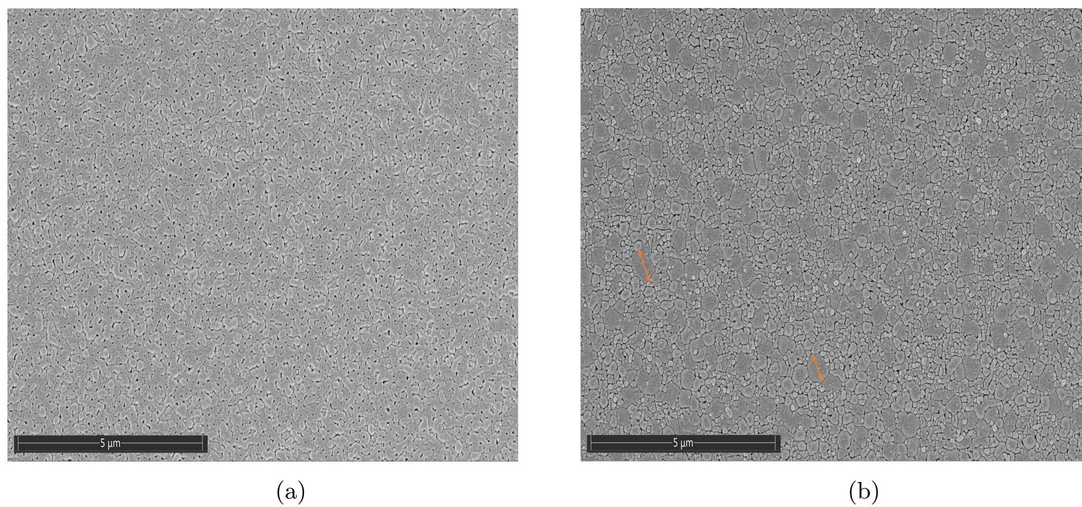

(a) (b)

Figure 4.1: SEM images of (a) SBN 001 and (b) SBN 310 obtained during FIB sample preparation. It can be seen that (b) has some large spherical grains marked by orange arrows. Obtained by Per Erik Vullum.

Figures 4.1a and 4.1b show the secondary electron SEM image of the samples named SBN 001 and SBN 310, respectively. These images show the surface of the thin films and were obtained prior to FIB preparation and after Pt/Pd coating to make the surface electrically conductive. It can be noticed that there are grains of varying sizes in both images. However, one can notice that in 4.1b, there are grains that are bigger in size than other grains (marked with orange arrows) and the number of these grains is more in 4.1b than in 4.1a.

Figure 4.3 shows the overall BF TEM image of the sample named SBN 001: (a) when STO is on zone (b) after tilting in +18.4° (c) after tilting in -18.4°. Four different BF TEM images were stitched together to obtain this image. The thin layer above the SBN film is the Pt/Pd layer deposited during FIB sample preparation. This TEM lamella contains about 54 grains of different sizes. The different grains are marked with different colored arrows depending on their contrast

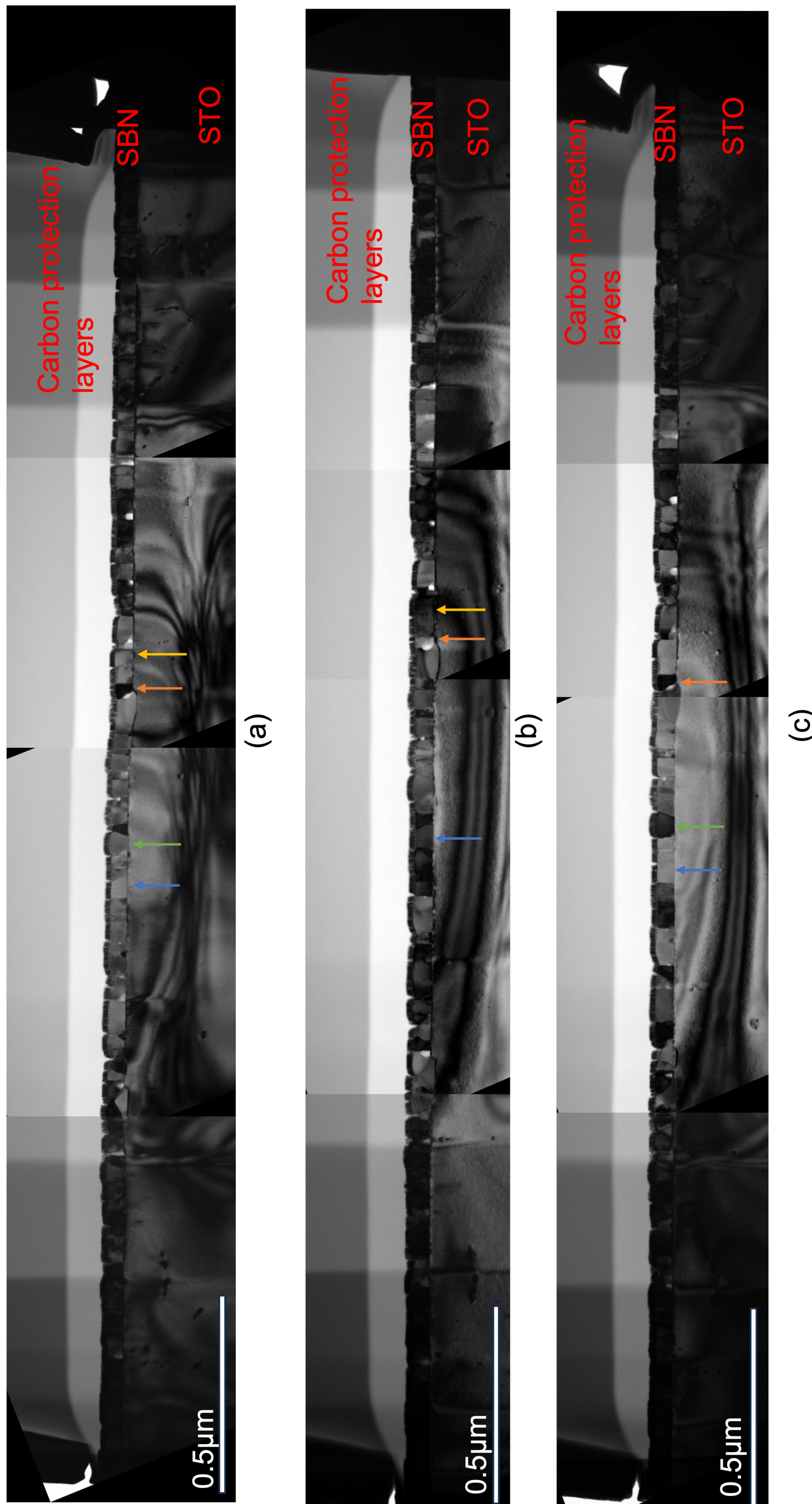

Figure 4.2: Overall BF TEM images of sample SBN 001 (a) when STO is on the zone, (b) when STO is tilted $+18.4°$, and (c) when STO is tilted $-18.4°$. The arrows show the typical grains that can help us in understanding diffraction contrast. The grains marked with blue and yellow arrows are bright when and become dark after tilting $+18.4°$, while the grain marked with an orange arrow is dark in (a) and becomes bright in (b). Grain marked with a green arrow becomes darker in (c) meaning that this grain comes to the zone after tilting $-18.4°$.

Figure 4.3

and orientation. A small objective aperture centered around the 000 spot in the diffraction pattern was used during BF TEM imaging. Hence, the dark contrast grains are the ones that are on zone while the bright contrast grains are the ones that are out of zone or slightly away from the high symmetry zone-axis. This type of contrast is called diffraction contrast as described in section

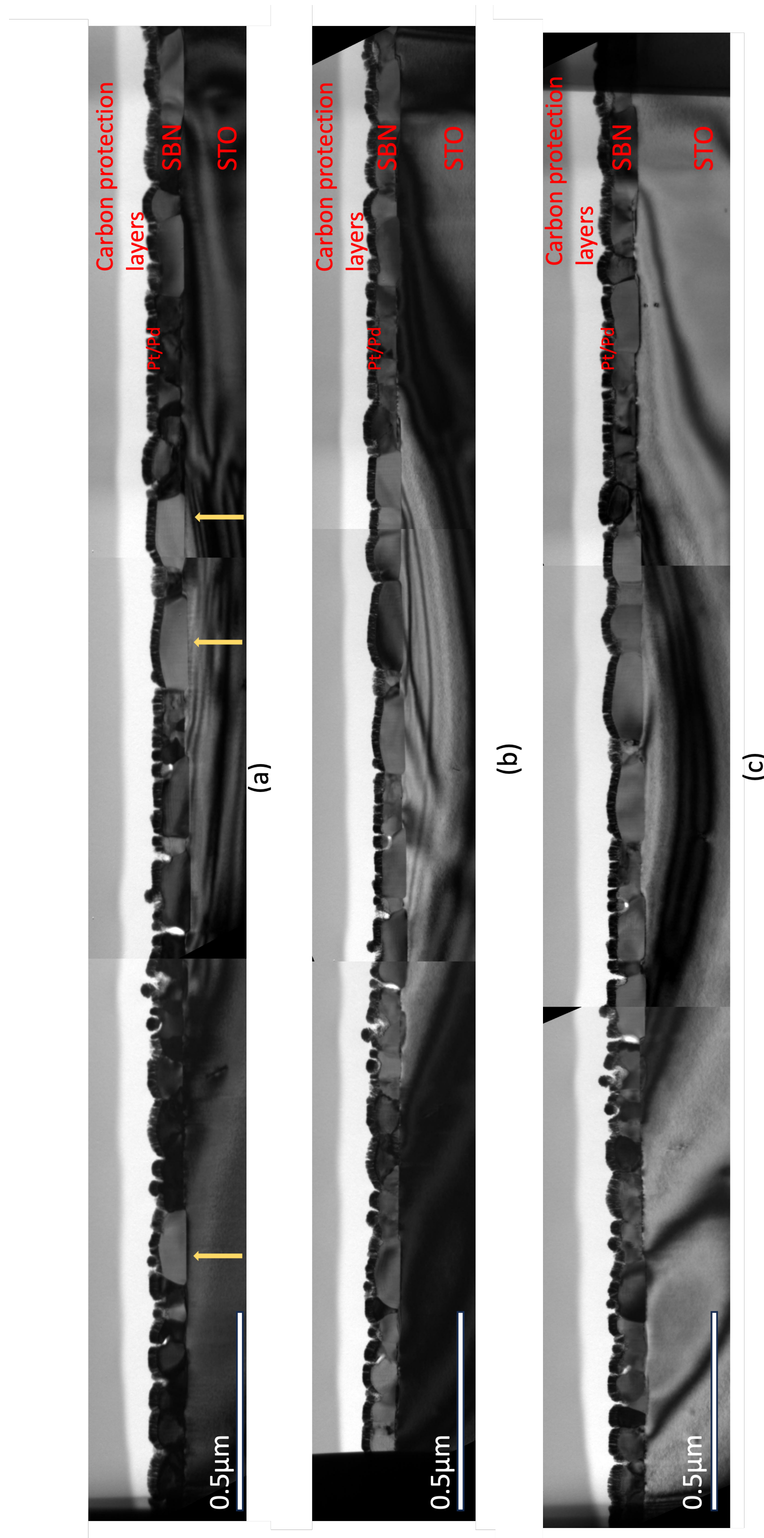

Figure 4.4: Overall BF TEM images of sample SBN 310 (a) when substrate STO is on the zone, (b) when substrate STO is tilted $+18.4°$, and (c) when substrate STO is tilted -18.4. The yellow arrows represent the grains that are wide than other grains and have a nearly flat interface than the other grains.

Figure 4.5

(2.5). In figure 4.3a four different grains are marked with different colored arrows. One can notice that the grain marked with an orange colored arrow is dark and hence it is on zone, while the grain with a blue arrow is the brightest and hence out of zone. While the other two grains with green and yellow arrows are grains that are away from the zone axis and can be brought to zone

after tilting either +18.4°or -18.4°. Figure 4.3b shows the BF TEM image of SBN 001 after tilting +18.4°. It can be noticed that the grain with the yellow arrow has become darker after tilting +18.4° which is a strong indication that this grain is now on zone. However, the grain with the orange arrow has become brighter. Figure 4.3c shows the BF TEM image of SBN 001 after tilting -18.4°. Here in this image, the grain with the green arrow has become darker after tilting -18.4° which is again an indication that this grain has come to the zone after tilting. However, in order to know whether the grain is on zone or not one must not only rely on the contrast, SADPs will give the exact information about this. This will be more clearly discussed in later sections.

In the same way, figure 4.5 shows the BF TEM of the sample named SBN 310: (a) when STO is on zone (b) after tilting +18.4° (c) after tilting −18.4°. In these BF TEM images, just like in figure 4.3, the contrast of the grains changes after tilting which helps us to have assumptions about whether the grain is on zone or not. One interesting thing that is to be noticed in figure **??**, is that some of the grains (marked with yellow arrows) are brighter as compared to other grains and these grains have a relatively flat interface (which is going down into the substrate) than the other grains. The next section will provide information on DPs from all grains of three different types.

4.2 Understanding Orientation with DPs

This section shows the BF TEM images, and SADPs from the grains with different orientations namely, in-plane, out-of-plane, and random from both samples. It also includes the Kikuchi pattern which helps the reader to understand which band was preserved while performing tilting. It is also to be kept in mind that the tilting was performed on the substrate STO and not on the SBN. So, when it is said written 'On zone´, this means that substrate is on zone and not the film.

Figures 4.6a and 4.6b show the BF TEM images obtained from a part of the films SBN 001 and SBN 310 respectively. Grains are marked as A, B, and C depending on the type of DP obtained. D here represents the STO substrate. The circles around the different grains represent the selected area aperture which means that this particular region was selected while obtaining SADPs. It is important to know that the smallest selected area diffraction aperture covers a circular region that is approximately 150nm in diameter. This region is usually larger than the size of the SBN grains. Hence, the STO substrate, protection layers, and sometimes one of the neighboring SBN grains contribute to the diffraction pattern from a specific grain. That is why some of the DPs in the result part 4.13a and 4.13b have rings, which means that an amorphous protection layer is included in the selected area aperture.

Figures 4.7a and 4.8a show the SADP that was taken from the substrate only, which is why it is marked as D. It is clear from the DP that it is oriented on the [001] zone axis.

Figures 4.7b and 4.8b show the DP from the substrate (D) and grain marked as (A). This grain has an in-plane orientation which was easy to predict with the help of known Miller indices of STO in the diffraction pattern. The lattice parameter of STO is $3.905\mathring{A}$, and the STO is of 001 type. With this information, we found the d-values for the STO spots and this in turn helped in calculating the d-values for all the spots from SBN. Also due to the nearly equal values of lattice parameters, the in-plane [100] of STO (in red) is parallel to the [310] of SBN (in white) while the out-of-plane [010] of STO is parallel to the [-130] of SBN. This brings us to the conclusion that the c-axis, in this case, is coming parallel to the interface between the film and substrate, hence c-axis is in-plane. As the polarization is along the c-axis, the polarization for this grain A is in-plane.

Figures 4.7c and 4.8c show the DP taken from grain B and substrate. This DP looks similar to the DP of STO in figure 4.7a but the only difference is that [010] reflection in (4.8c) is denser as compared to the one in the DP of STO. The distance between the 310 and the (001) planes of SBN are almost identical. Furthermore, this lattice plane distance match quite well the lattice parameter of the $SrTiO_3$ substrate. Hence, the $< 310 >$ and [001] directions of SBN tend to align with the $< 100 >$ directions of $SrTiO_3$. However, this close match between the 310 and (001)

planes of SBN makes it hard to discriminate between these directions. But as described in the sections (3.4) and in (2.3.3), tilting ± 18.4 degrees around the [100] direction of $SrTiO_3$ makes it possible to discriminate between the $< 310 >$ and the [001] directions of SBN, and hence uniquely determine the direction of the ferroelectric polarization.

Figure 4.7d and 4.8d show the DP from grain C and substrate. It is clear from this DP that this grain is not oriented to any zone axis. So, one can conclude that this grain has a random orientation.

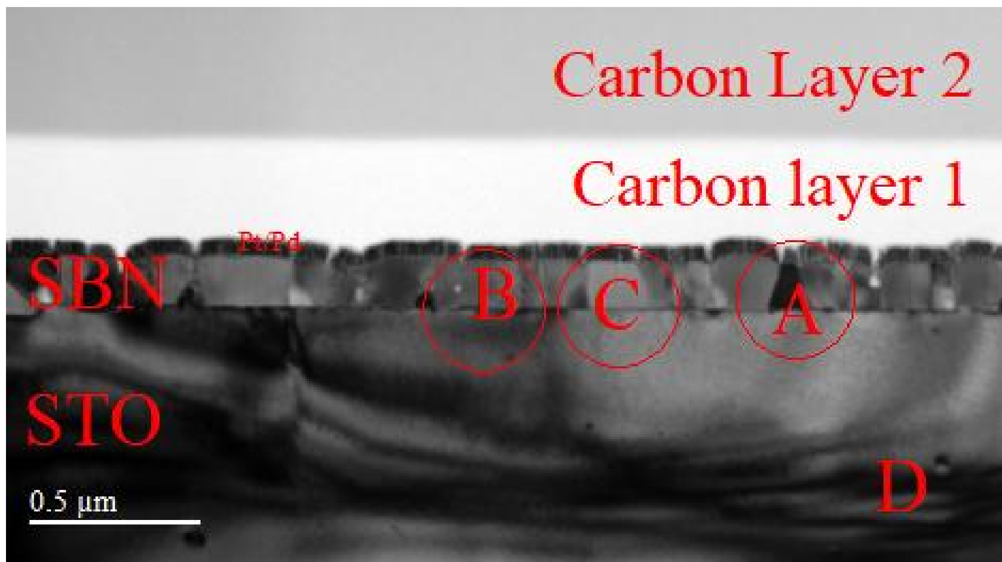

(a)

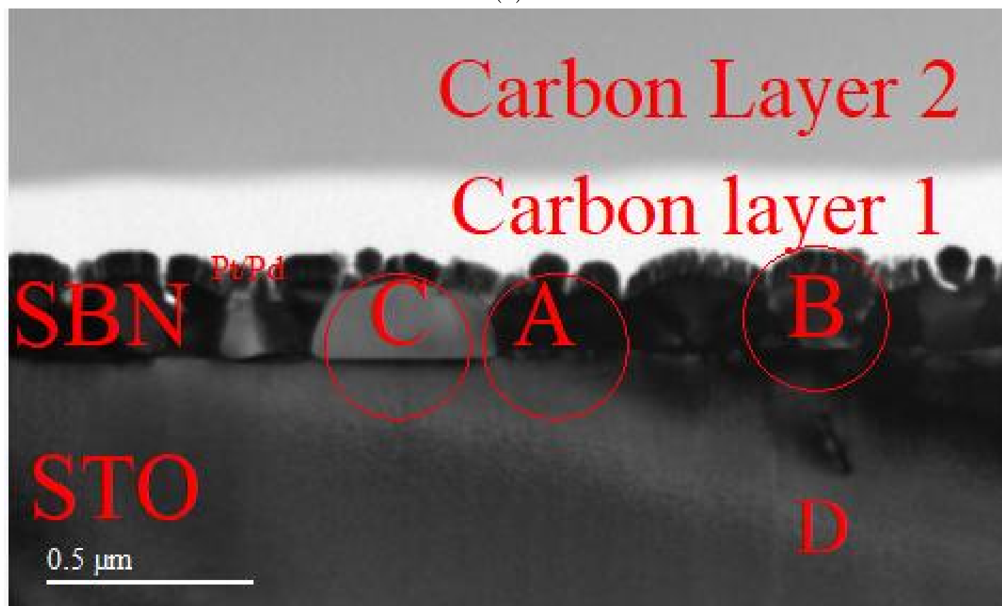

(b)

Figure 4.6: BF TEM images (a) from SBN 001 (b) SBN 310 showing the different types of grains marked with A, B, and C depending on their contrast. The darkest grain is marked as A and the brightest is marked as C. D represents the substrate. Red rings around the grains indicate the selected area aperture. The selected area aperture around grain A in (a) covers the neighboring grains also showing that the smallest selected area aperture is larger than the width of the grains.

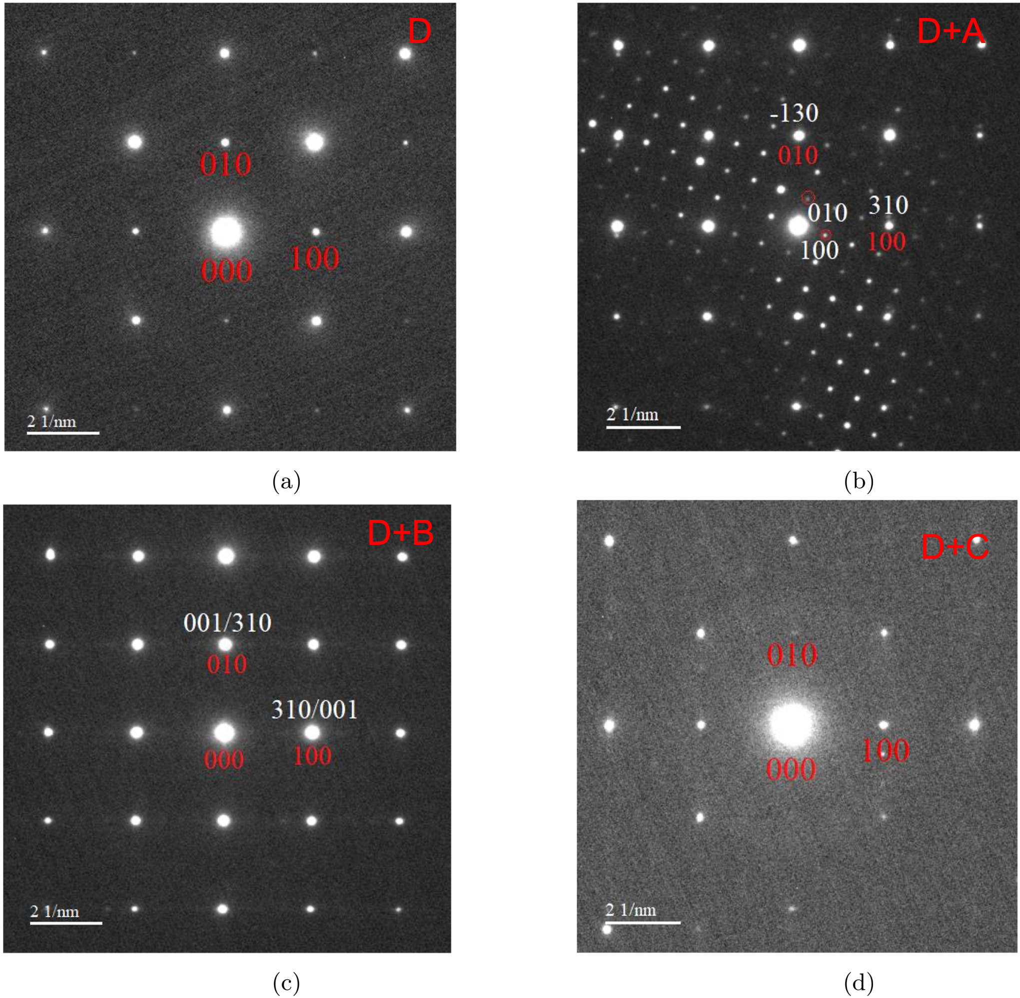

(a) (b)

(c) (d)

Figure 4.7: DPs from sample named SBN 001 corresponding to the BF TEM in 4.6a. (a) DP from the substrate STO marked by D in 4.6a. This DP shows that the STO is oriented to the [001] zone axis. (b) DP from grain marked A in 4.6a including STO. DP of SBN is denser than that of STO, indicating that DP is from the ab plane of the SBN and c-axis is parallel to the interface between STO and SBN. Therefore c-axis is in-plane and hence the polarization is in-plane. (c) DP from grain marked C in 4.6a plus substrate STO. This DP looks similar to the DP of STO in (a) and thus in this DP. Also, it is hard to discriminate between the 310 and 001 Bragg reflections of SBN (in white) because the distance between 310 and the (001) planes of SBN are almost identical and lattice plane distance matches well with the lattice parameter of STO. Therefore, titling was performed to know the direction of c-axis. (d) DP from grain marked C in 4.6a plus the substrate D. DP shows that this grain is not oriented to any zone axis, hence it has random orientation.

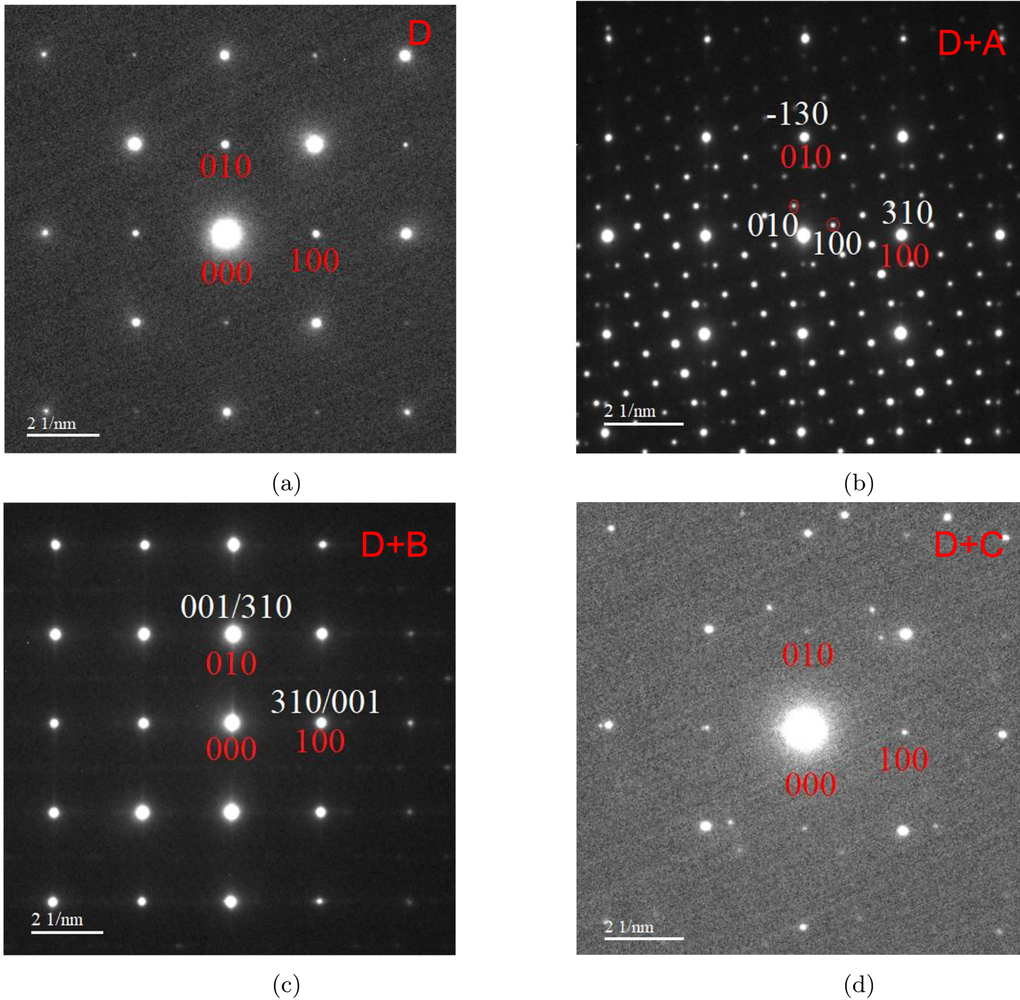

(a) (b) (c) (d)

Figure 4.8: DPs from sample named SBN 310 corresponding to the BF TEM in 4.6b. (a) DP from the substrate STO marked by D in 4.6b. This DP shows that the STO is oriented to the [001] zone axis. (b) DP from grain marked A in 4.6b including STO. DP of SBN is denser than that of STO, indicating that DP is from the ab plane of the SBN and c-axis is parallel to the interface between STO and SBN. Therefore c-axis is in-plane and hence the polarization is in-plane. (c) DP from grain marked C in 4.6b plus substrate STO. This DP looks similar to the DP of STO in (a) and thus in this DP. Also, it is hard to discriminate between the 310 and 001 Bragg reflections of SBN (in white) because the distance between 310 and the (001) planes of SBN is almost identical and the lattice plane distance matches well with the lattice parameter of STO. Therefore, titling was performed to know the direction of the c-axis. (d) DP from grain marked C in 4.6b plus the substrate D. DP shows that this grain is not oriented to any zone axis, hence it has a random orientation.

4.3 To find out-of-plane orientation

It was found in the section above that DPs from some grains are very dense and after finding d-values and indexing the spots, it was concluded that grains having these DPs have in-plane orientation. While in the diffraction patterns 4.8c and 4.7c, it is hard to figure out the orientation and difficult to discriminate between Bragg reflections 001 and 310. As mentioned in section (2.3.3), the angle between the perpendicular c-axis (001) of SBN and a-b axis (310) of STO is 18.4°, so this particular diffraction pattern was tilted ±18.4° along the direction out-of-plane direction as described in section (3.4). Figure 4.9 shows the Kikuchi pattern in real space of the substrate STO (a) before tilting or on zone and (b, c) after tilting in ±18.4°. The red line represents the band preserved during the tilting process.

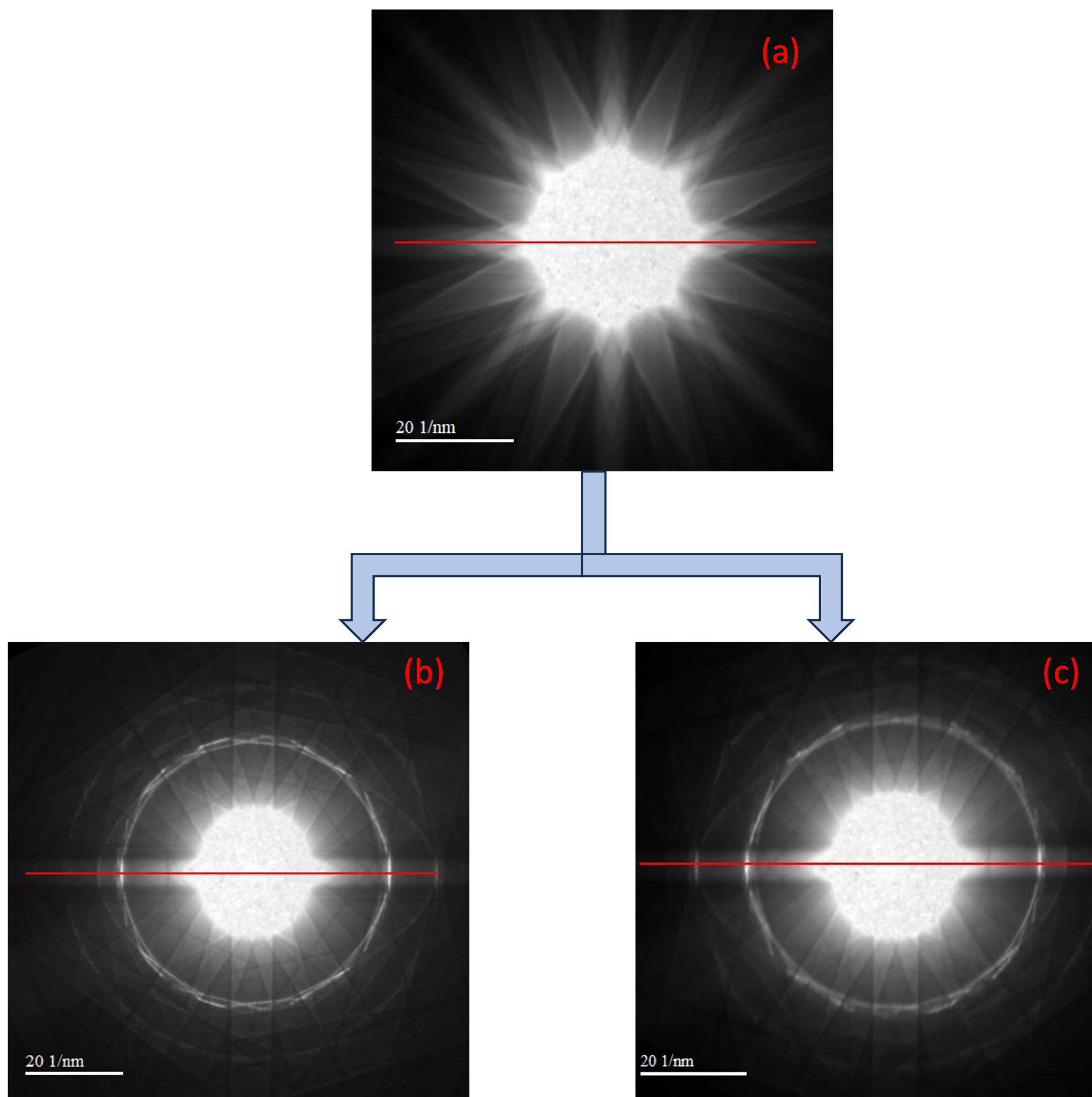

Figure 4.9: Kikuchi pattern from substrate STO obtained during tilting process: (a) when substrate STO is on zone, (b) when substrate STO is tilted +18.4, and (c) when substrate STO is tilted −18.4°. The red line indicates the band in the Kikuchi pattern that was preserved during tilting.

Figures 4.10a, 4.11a, 4.12a, and 4.13a, show the DPs from grains of type B from SBN 001 and SBN 310, when these grains are on the zone. Figures 4.10b and 4.12b shows the DP after tilting these grains by $-18.4°$ and figures 4.11b, 4.13b show the DP after tilting these grains by $+18.4°$. It can be noticed that the DPs after tilting match the DP in figure 3.4b and 3.4c that we got from recipro simulations. This brings us to the conclusion that the vertical Bragg reflection in 4.10a, 4.11a, 4.12a, and 4.13a is 001 and that the c-axis, in this case, is out-of-plane. Therefore, the polarization of grains of type B is out-of-plane. One can also notice that Bragg reflections along the horizontal line after tilting become dense. It is also proof that this direction is either a or b and not c. So, according to the explanation in section (3.4), these types of grains have out-of-plane polarization.

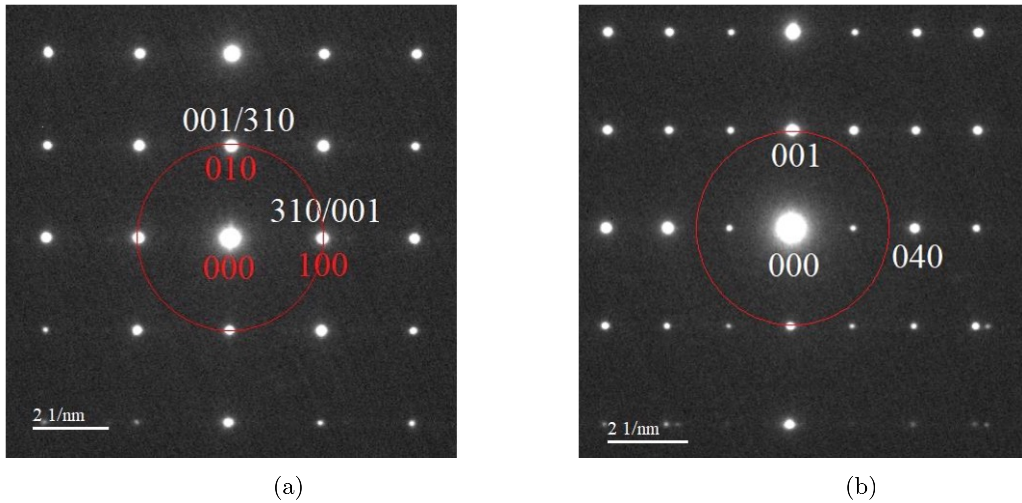

(a) (b)

Figure 4.10: DPs from the grain of type B of SBN 001 (a) before and (b) after tilting in -18.4°.

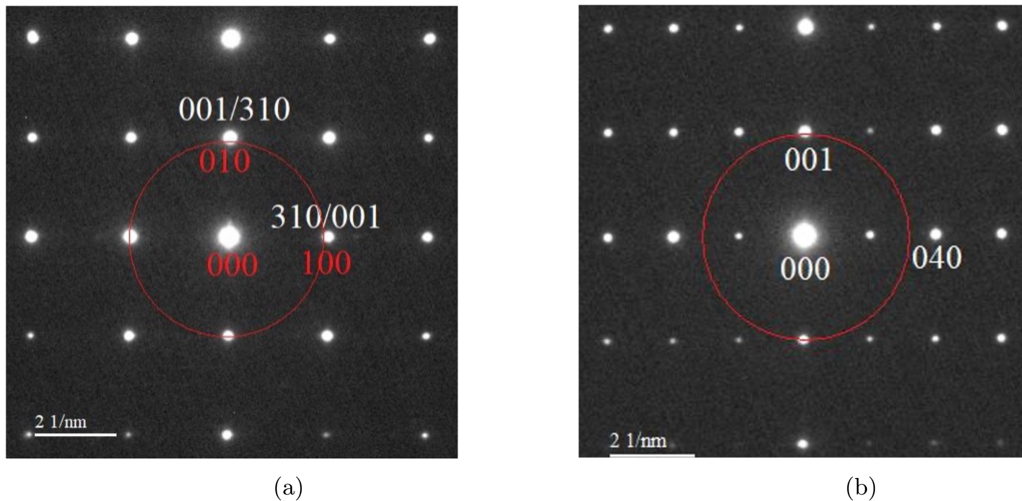

(a) (b)

Figure 4.11: DPs from the grain of type B of SBN 001 (a) before and (b) after tilting in +18.4°.

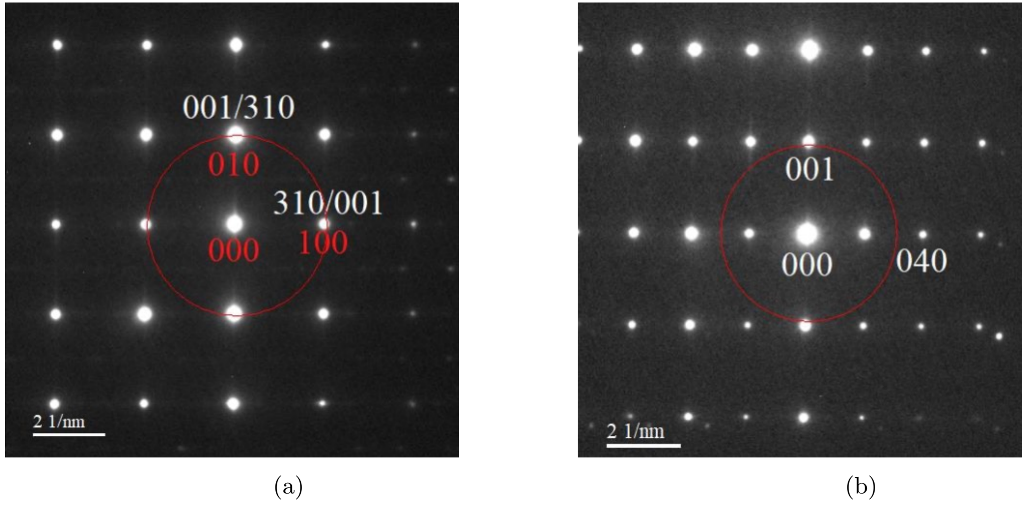

(a) (b)

Figure 4.12: DPs from grain of SBN 310 (a) before and (b) after tilting in -18.4°.

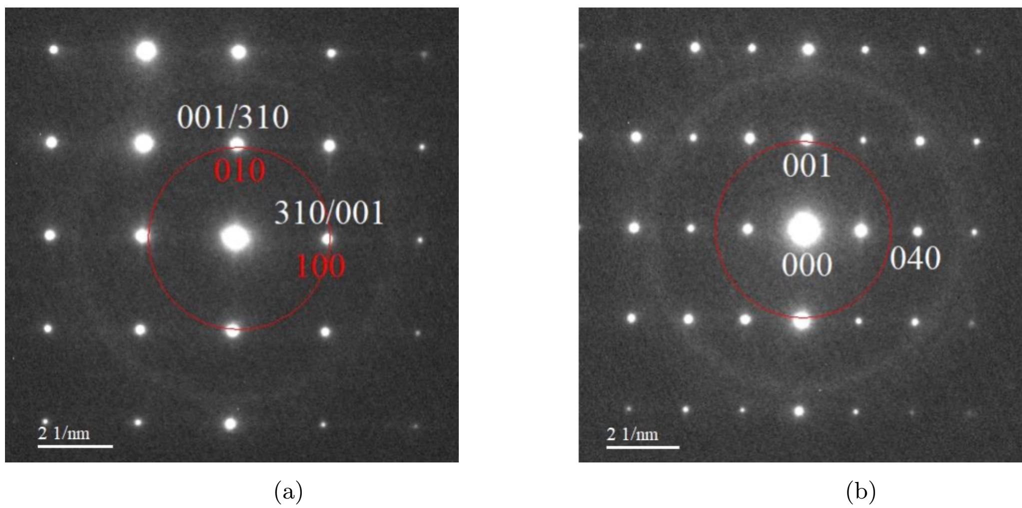

(a) (b)

Figure 4.13: DPs from the grain of SBN 310 (a) before and (b) after tilting in +18.4°. It can be noticed that in all DPs after tilting, the reflections along in-plane directions become denser, which means that it is either the a or b axis of SBN thin film, and hence, c-axis is along the out-of-plane direction. Therefore grains of type B have out-of-plane orientation.

4.4 Statistics of the grains

In this way, with the help of SAED patterns and tilting, the polarization direction or direction of the c-axis was figured out from all the grains of both samples. The table (4.1) shows the statistics of all the grains of SBN 001. There were 54 grains in total. It was expected that all the grains in this sample have out-of-plane polarization. Which is proven to be true. As 50 out of 54 grains i.e. 92.6% of the grains have out-of-plane polarization. Only 2 grains have in-plane polarization and there were only 2 grains with random orientation.

Table 4.1: Statistics of all grains from SBN 001

Statistics from SBN 001		
Total number of grains	54	Percentage
Grains with in-plane polarization (310)	2	3.7
Grains with out-of-plane polarization (001)	50	92.6
Grains with Random orientation	2	3.7

In the same way table (4.2) shows the statistics from the other sample named SBN 310. The total number of grains observed in this case were approximately 41. This sample was expected to have more in-plane polarization of the grains. But the results were slightly different. Out of 41 grains, only 23 (56.1%) had in-plane polarization, 13 (31.7%) had random orientation, and 5 (12.2%) had in-plane polarization. The reason for this will be discussed in the discussion section.

Table 4.2: Statistics of all grains from SBN 310

Statistics from SBN 310		
Total number of grains	41	Percentage
Grains with in-plane polarization (310)	23	56.1
Grains with out-of-plane polarization (001)	5	12.2
Grains with Random orientation	13	31.7

4.5 Results from JEOL JEM-ARM200F

This section will present the results obtained from JEOL JEM-ARM200F by my co-supervisor Per Erik Vullum. These results were obtained from three types of orientations (in-plane, out-of-plane, and random) from only one sample named SBN 001. It will first show the HAADF-STEM images, and EELS and EDS maps from all three types of orientation and then line profiles corresponding to these maps.

Figures 4.15, 4.16, and 4.17 show the HAADF-STEM image along with elemental maps from three types of orientations out-of-plane, in-plane, and random respectively. From the HAADF STEM image, it was found that the interface between the substrate and the film is not flat. Hence it was difficult to know about the STO termination that whether it is terminated with TiO_2 or SrO. The illustration in figure 4.14 helps the reader to understand about the termination. It can be seen in figure 4.14a that TEM lamella has a thickness of approximately 60nm, which was calculated using HAADF STEM. Ideally, the interface should look like the one illustrated in figure 4.14a. STO substrate should either terminate with the SrO layer or TiO_2, such that it is easy to find the termination by just looking at the interface. However, the variations in surface topography of the STO surface are less than the thickness of the TEM lamella as illustrated in 4.14b, which makes it difficult to know about the termination.

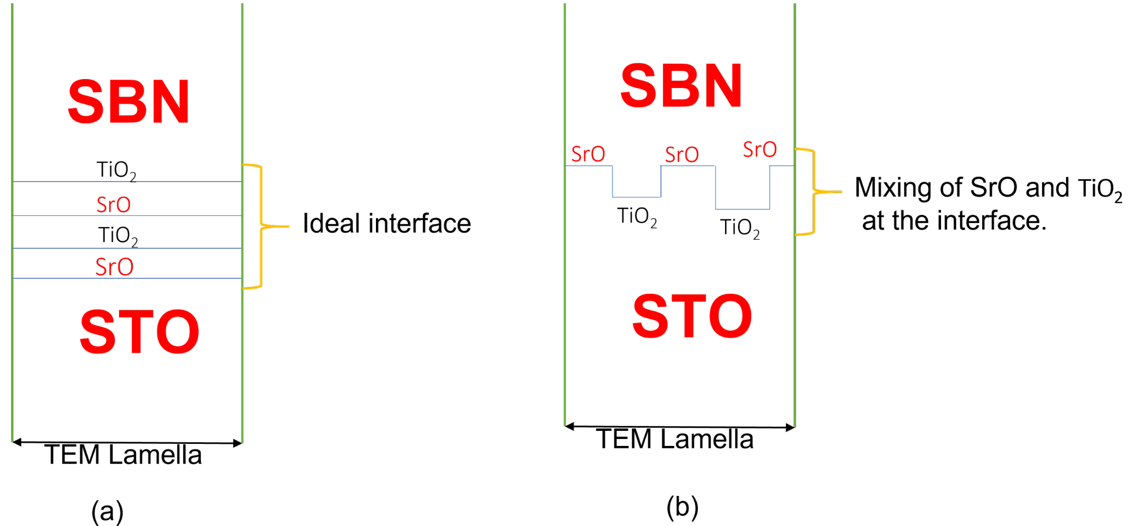

Figure 4.14: Illustration of surface topography of STO substrate. (a) Ideally, STO should either terminate with SrO or TiO_2. However (b) shows that the surface topography of STO changes alot within the thickness of TEM lamella.

The maps of Sr, Ti, O, and Ba are obtained from EELS data, while the map for Nb is taken from EDS data. In the colored map, it was noticed that the Ba and Sr occupy different sites in the film, which was expected [27, 57].

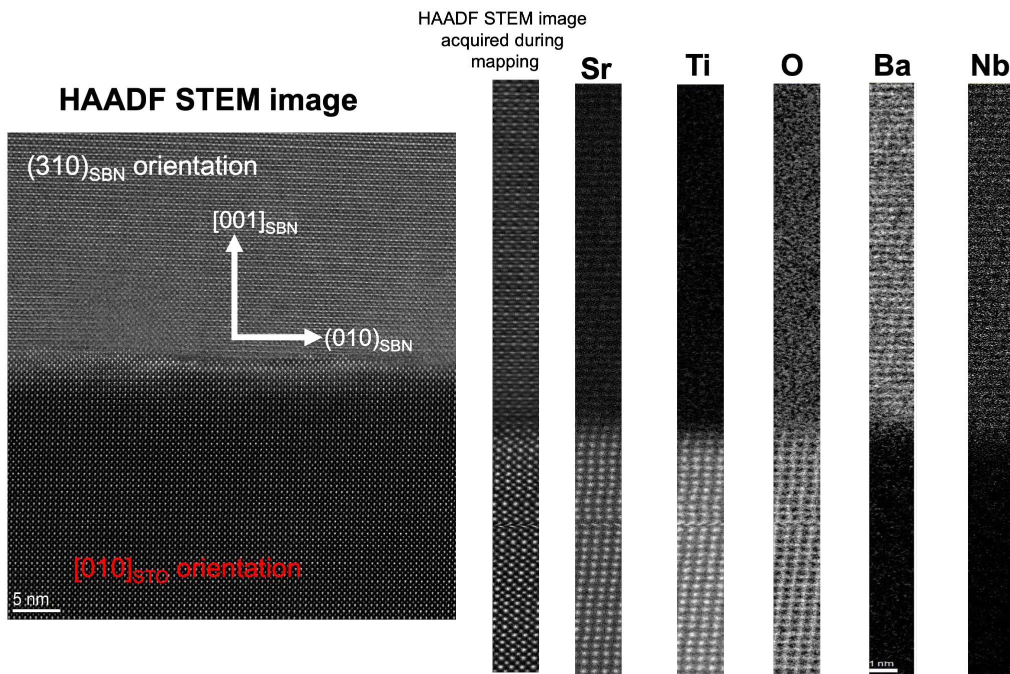

Figure 4.15: Figure showing HAADF STEM image from grain with in-plane polarization along with EELS (for Sr, Ti, O, and Ba) and EDS (for Nb) elemental maps. The colored map shows that Ba and Sr occupy different sites in the thin film structure. Taken by Per Erik Vullum.

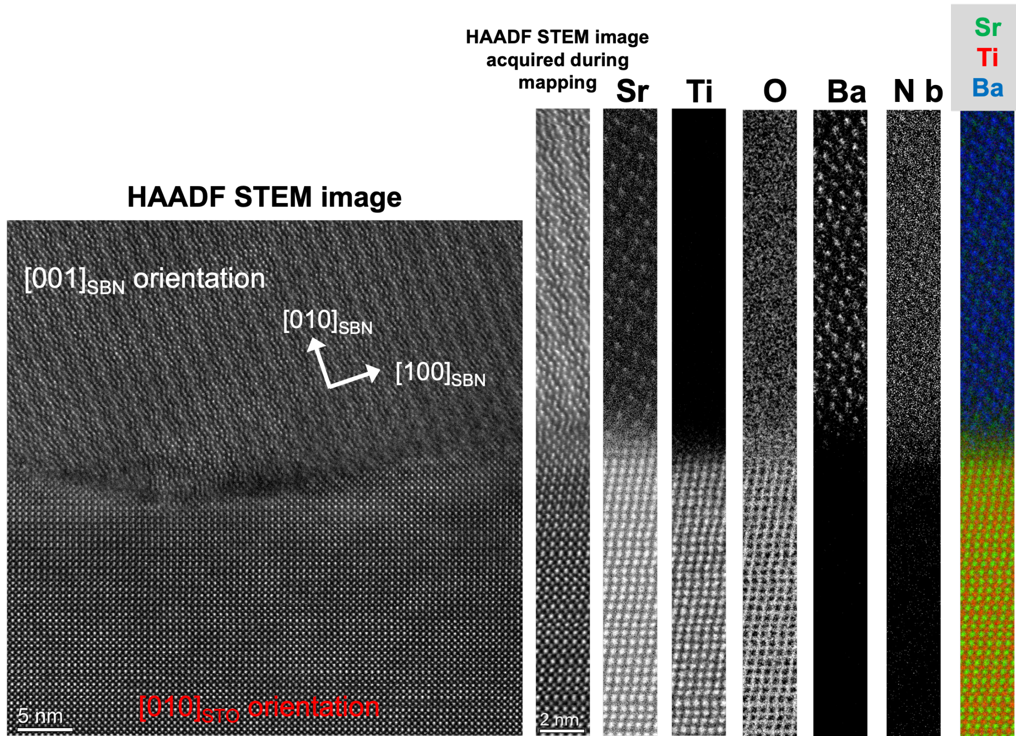

Figure 4.16: Figure showing HAADF STEM image from grain with out-of-plane polarization along with EELS (for Sr, Ti, O, and Ba) and EDS (for Nb) elemental maps. Taken by Per Erik Vullum

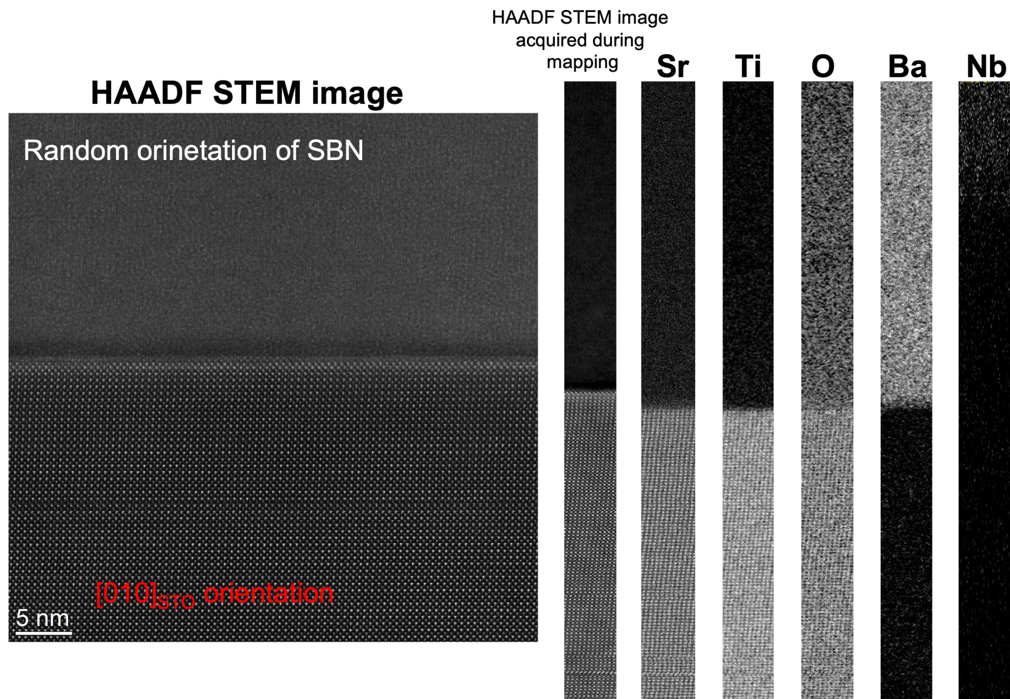

Figure 4.17: Figure showing HAADF STEM image from grain with random orientation along with EELS (for Sr, Ti, O, and Ba) and EDS (for Nb) elemental maps. Taken by Per Erik Vullum

Figures 4.18a, 4.18b, and 4.18c show the line profiles obtained from the EELS maps from three different orientations of grains: (a) out-of-plane (b) in-plane (c) random. These line profiles show how the chemical composition, in atomic percentage, develops as a function of distance from the STO/SBN interface. Above, the line profile is the HAADF STEM image which is rotated 90° to make it horizontal with STO on the left and SBN on the right. It can be observed clearly that there are systematic errors in the qualifications. In STO, we see that Ti and Sr are higher than 20%, while O is lower than 60%. However, the relative changes are reliable. It can be also noticed that Nb is not included in the quantifications, because Nb peaks were not present inside the detected energy loss region. The very interesting and surprising thing that was worth noting from these profiles was, the Ti peak does not decay to zero up to nearly 15nm into the SBN film.

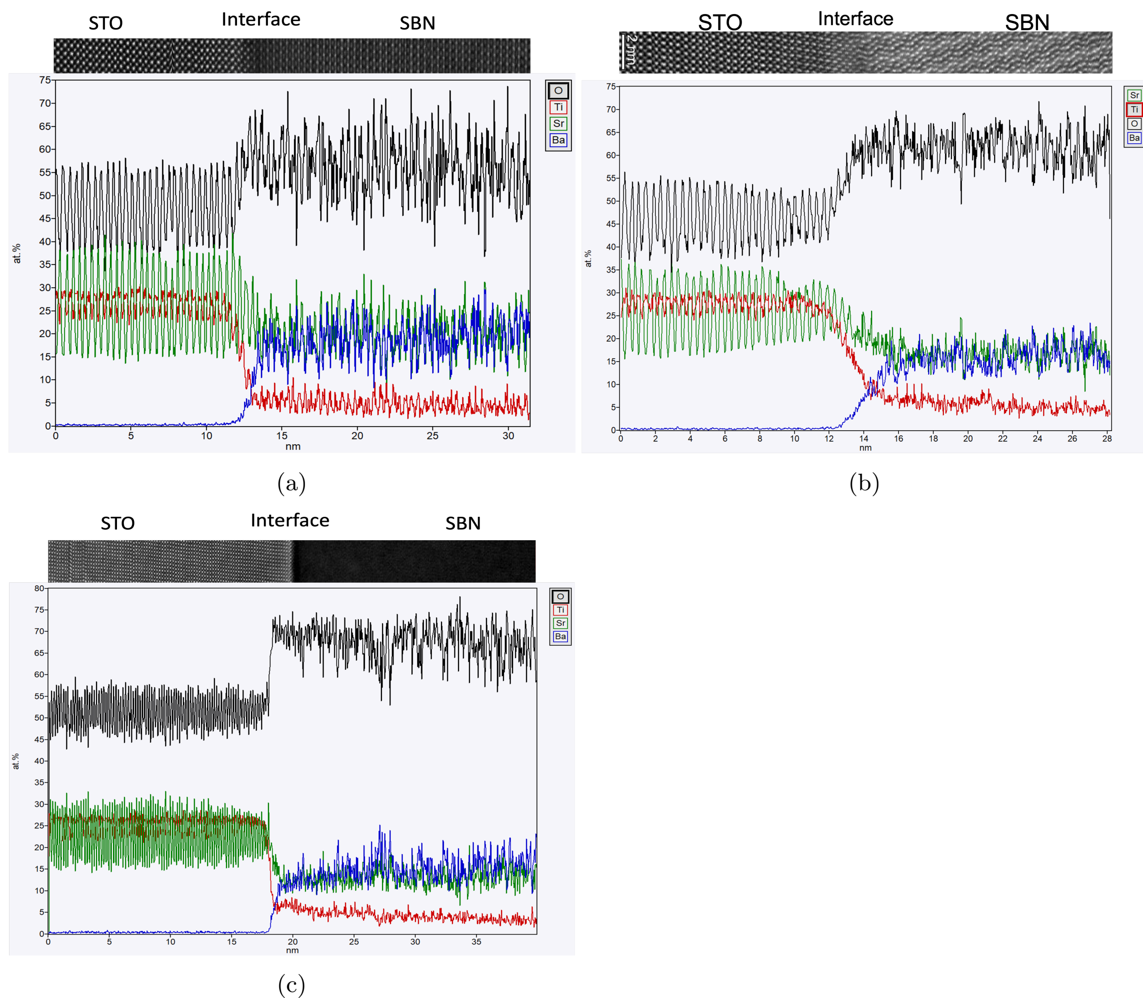

(a)

(b)

(c)

Figure 4.18: Line profiles from grains with (a) out-of-plane (b) in-plane (c) random orientation. It can be noticed that Ti signal does not decay to zero upto the distance of approximately 15nm in the film.

5 Discussion

In the results it has been found that the grains in the SBN thin films possess three types of orientations: in-plane, out-of-plane, and random. It was expected to have mainly out-of-plane orientation in SBN 001 and in-plane orientation in SBN 310 based on [16], however, grains with random orientation were also found. It was also noticed that these grains are relatively wide and go into the substrate as shown in the BF TEM image 5.1a. First, it was believed that the heat treatments might have changed the surface topography of the substrate. But later, it was discovered that the quality of the substrates as received were of low quality and defects were discovered. From statistics in section (4.4), it was found that SBN 310 had more randomly oriented grains (31.7%), while SBN 001 had only 3.7% randomly oriented grains. It was discovered by Viviann from the atomic force microscopy (AFM) images, after thin film deposition, that the defects vary quite a lot at different places on the substrate, so it could be possible that a spot with more defects was chosen for SBN 310 and a spot with good quality was chosen for SBN 001. However, it is still not confirmed as the substrates themselves were not investigated before thin film deposition.

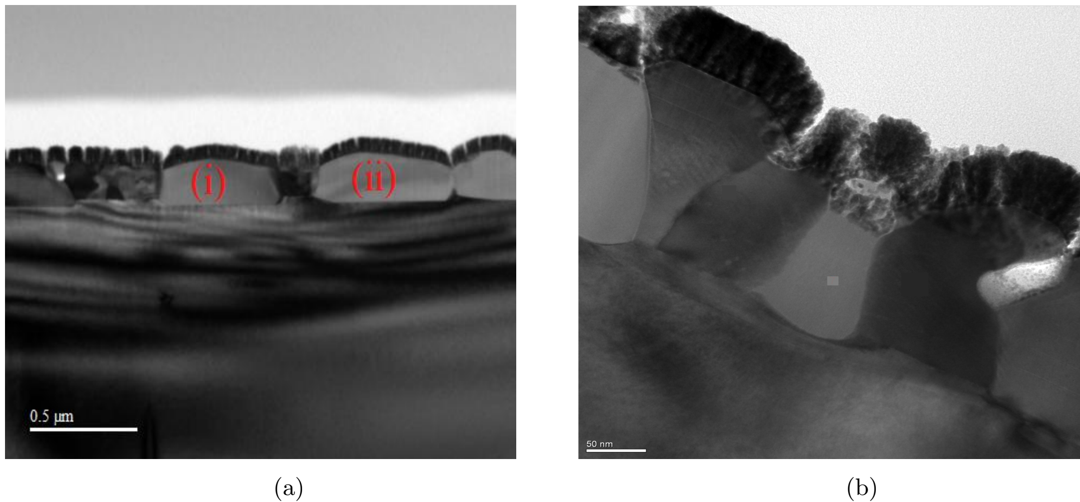

(a) (b)

Figure 5.1: (a) BF TEM image showing randomly oriented grains marked (i) and (ii) going slightly down into the substrate STO. (b) HRTEM image showing the variations in surface topography of substrate STO.

As mentioned in section (4.5), the surface topography of STO substrate varies a lot. This is shown in the HRTEM image 5.1b taken from SBN 310. The main problem is that the length scale of the surface steps and variations in the surface topography of STO is significantly smaller than the typical thickness of the TEM lamella. Hence, the interface between the substrate and the film is smeared out in the two-dimensional projections in the TEM and STEM images. This smearing made it difficult to conclude about any consistent surface termination of the STO substrate for the various SBN grain orientations. So, the hypothesis that SrO termination favors out-of-plane

orientation and TiO_2 termination favors in-plane orientation cannot be confirmed. However, the high texture in SBN 001 confirms the hypothesis that the out-of-plane polarization is favored, also for multiple layers, by the given substrate pre-treatment, expected to give SrO termination, and a slow heating rate of 0.04°C/s. [16].

From the line profiles, it was discovered that the titanium does not decay to zero up to approximately 15nm deep into the film. Ideally, it should decay to zero within a few nanometers of the film since there is no Ti in the SBN film [44]. Ti diffusion into SBN has likely occurred due to the reason that SBN can accommodate quite large concentrations of Ti[56]. Nb is substituted by Ti despite the fact Nb has a valency of +5 and Ti has a valency of +4. In order to maintain charge neutrality, oxygen vacancies are introduced [56].

6 Conclusion

The aim of this theis was to study the orientations of the different grains in two samples of SBN thin film: SBN 001 and SBN 310. Thin films were synthesized using a method called acqueos chemical solution deposition. TEM samples were prepared usin FIB technique. Different TEM techniques were then used to find out the polarization directions in all the grains. A summary of the results and what more in future can be done is given in this section.

SBN 001 was found to have 92.6% of grains with out-of-polarization, while SBN 310 has 56% of grains with in-plane polarization, 31% with random, and 12% with out-of-plane The orientation of the grains is important for practical applications of ferroelectric materials as SBN is uniaxial ferroelectric with polarization along the c-axis. It is also desirable to have the axis pointing in the same direction for all the grains, to achieve maximum polarizability of the films. The maximum polarizability is reduced in SBN 310 because the c-axis in this case is in-plane and grains can point in two directions and average polarization goes diagonally along the STO surface. However, SBN 001 has maximum polarizability, because polarization in all grains point normal to the STO surface giving a single out-of-plane polarization. So, SBN 001 orientation is preferable and further studies can focus on how to achieve out-of-plane orientation of all the grains in the film [16].

It as also found using line profiles that the Ti signal does not decay to zero in SBN film for all three orientations of SBN 001. The diffusion of Titanium into the film can alter the properties of the film. Thus future studies can also focus on how to avoid titanium diffusion into the film or how to take advantage of this intermixing. New spectroscopy maps that extend across the entire film thickness could give insight into how far Ti has diffused. Significant Ti concentrations in SBN could possibly alter several of the material properties, such as Curie temperature, the amplitude of the polarization, and the external coercive field necessary to switch the polarization. Hence, it is relevant for the applied properties of the material system.

The STO single crystal substrates on which SBN film was spin-coated obviously belong to a poor batch with very large variations in surface topography as found in HAADF STEM images. New samples grown on better STO substrates, (close to) atomically flat over several square micrometers could possibly give more systematic results with respect to the orientation of the SBN grains. Such samples would also be much better suited for TEM characterizations as it would be a lot easier to determine the surface termination of STO, and hence figure out from a fundamental perspective how in-plane and out-of-plane polarization can be tuned and tailor-made.

References

[1] C.Kittel. *Introduction to Solid State Physics.* Wiley, 2005.

[2] R.J.D Tilley. *Crystals and Crystal Structures.* Wiley, 2006.

[3] P. Hofmann. *Solid State Physics- An Introduction.*Wiley-VCH, 2015.

[4] J. Als-Nielsen and D. McMorrow. Elements of Modern X-ray Physics. Wiley, 2011. ISBN 9781119970156

[5] D. B. Williams and B. C. Carter. Transmission Electron Microscopy, A Textbook for Materials Science. Springer, 2009. doi: 10.1007/978-0-387-76501-3.

[6] X-ray data booklet, 2000. URL http://xdb.lbl.gov/.

[7] M. A. Aegerter, M. Mennig, *Sol-Gel Technologies for Glass Producers and User*, Kluwer Academic Publishers, 2004.

[8] W. D. Callister and D. G. Rethwisch. *Materials Science and Engineering: An Introduction.* 8th. Wiley, 2009.

[9] A. Sengupta, C. K. Sarkar. *Introduction to Nano: Basics to Nanoscience and Nanotechnology.* Springer, 2015.

[10] M. I. Khan, T. C. Upadhyay, *General Introduction to Ferroelectrics.* IntechOpen, 2021.

[11] P. Costa, J. N. Pereira, N. Pereira, N. Castro, S. Gonçalves, and S. L. Mendez. "Recent Progress on Piezoelectric, Pyroelectric, and Magnetoelectric Polymer-Based Energy-Harvesting Devices." Energy Technology, 2019, https://doi.org/10.1002/ente.201800852.

[12] A. Norton, *Dynamic Fields and waves*, 1st ed. CRC Press, 2000. https://doi.org/10.1201/9780429187513.

[13] B. Fultz, J. M. Howe, *Transmission Electron Microscopy and Diffractometry of Materilas.* 3rd ed., Springer Berlin, Heidelberg, 2007.

[14] J. Chang, Y. S. Park, and S. K. Kim, "Atomically flat single-terminated SrTiO3 (111) surface". Applied Physics letters 92, 2008, DOI: 10.1063/1.2913005

[15] A. B. Blichfeld, K. Bakken, D. Chernyshov, J. Glaum, T. Grande, and M. A. Einarsrud, "Experimental setup for high-temperature in situ studies of crystallization of thin films with atmosphere control". Journal of Synchrotron Radiation, 2020, https://doi.org/10.1107/S1600577520010140.

[16] V. H. Pedersen, A. B. Blichfeld, K. Bakken, D. Chernyshov, T. Grande, and M. A. Einarsrud, "Crystallization and Texturing of $Sr_xBa_{1-x}Nb_2O_6$ Thin Films Prepared by Aqueous Solution Deposition- An In Situ X-ray Diffraction study". Crystal Growth and Design, ACS Publications, 2022, https://doi.org/10.1021/acs.cgd.2c00553.

[17] T. M. Raeder, K. Bakken, J. Glaum, M. A. Einarsrud, and T. Grande, "Enhanced in-plane ferroelectricity in $BaTiO_3$ thin films fabricated by aqueous chemical solution deposition". AIP publishers, 2018, https://doi.org/10.1063/1.5059549.

[18] F. Madaro, "Synthesis of Textured $K_xNa_{1-x}NbO_3$ Materials. Norwegian University of Science and Technology: NTNU, Trondheim, Norway, 2010.

[19] X. Huang, N. Hansen, and N. Tsuji, "Hardening by Annealing and softning by Deformation in Nanosctructured Metals". Science, 2006, DOI: 10.1126/science.1124268.

[20] A. G. Schrott, J. A. Misewic, D. W. Abraham, and Y. Zhang, "A-site surface termination in strontium titanate single crystals". Applied Physics Letters, 2001, https://doi.org/10.1063/1.1404129.

[21] E. Stauffer, J. A. Dolan, R. Newman, *Fire Debris Analysis: Chapter 4*. Science Direct, 2008, DOI: 10.1016/B978-012663971-1.50008-7

[22] "Gatan microscopy suite software." URL: http://www.gatan.com/products/ tem-analysis/gatan-microscopy-suite-software. Accessed: 03.12.2017.

[23] R.J.D Tilley. *Undestanding Solids: The science of materials.* Wiley, 2004.

[24] G. H. Olsen, "Ferroelectric Tungsten Bronzes, Ph.D. thesis". Norwegian University of Science and Technology, 2016.

[25] V. Hole, "Hydrothermal synthesis of $Sr_xBa_{1-x}Nb_2O_6$ on nanostructured substrates, Master's thesis." Norwegian University of Science and Technology, 2019.

[26] K. Rani, "Switchable photovoltaic properties in ferroelectric PZT thin films." Materials Science. Université Paris-Saclay, 2022.

[27] S. Podlozhenov, H. A. Graetsch, J. Schneider, M. Ulex, M. Wöhlecke, and K. Betzler, "Structure of strontium barium niobate $Sr_xBa_{1-x}Nb_2O_6$ (SBN) in the composition range $0.32 \leq x \leq 0.82$." Structural Science, 2006, ISSN 0108-7681.

[28] P. B. Jamieson, S. C. Abrahams, and J. L. Bernstein, "Ferroelectric Tungsten Bronze-Type Crystal Structure. I. Barium Strontium Niobate $Ba_{0.27}Sr_{0.73}Nb_2O_{5.78}$." The journal of Chemical Physics, Volume 48, Number 11, 1968.

[29] J. G. Carrio, Y.P. Mascarenhus, W. Yelon, I. A. Santos, D. Garcia, and J. A. Eiras, " Structure Refinement of $(Sr, Ba)Nb_2O_6$ Ceramic Powder from Neutron and X-Rays Diffraction Data." Materials Research, Volume 5, Number 1, 2002.

[30] R. R. Neurgaonkar, W. F. Hall, J. R. Oliver, W. W. Ho, and W. K. Cory, "Tungsten bronze Sr1-x Ba x Nb2O6: A case history of versatility." Ferroelectrics, DOI: 10.1080/00150198808201379.

[31] A. R. West. *Solid state chemistry and its applications*, 2nd edition, 63-66, Wiley, 2014.

[32] M. Pàsciak, P. Ondrejkovic, J. Kulda, P. Vanêk, J. Drahokoupil, G. Steciuk, L. Palatinus, T. R. Welberry, H. E. Fischer, J. Hlinka, and E. Buixaderas, "Local structure of relaxor ferroelectric $Sr_xBa1-xNb_2O_6$ from pair distribution function analysis." Physical Review B 99, 104102, 2019, DOI: 10.1103/PhysRevB.99.104102.

[33] A. Infortuna, P. Muralt, and M. Cantoni et. al., " Epitaxial growth of $(SrBa)Nb_2O_6$ thin films on $SrTiO_3$ single crystal substrate." Journal of applied physics 100, 2006, https://doi.org/10.1063/1.2372577.

[34] T. R. Volk, V. Yu. Salobutin, L. I. Ivleva, N. M. Polozkov, R. Pankrath, and M. Woehlecke, "Ferroelectric properties of strontium barium niobate crystals doped with rare-earth metals." Physics of the Solid State 42, 2129-2136. ISSN: 1090-6460 (11 2000).

[35] M. Meloa, E.B. Araujoa, A.P. Turyginb, V.Ya. Shurb, and A.L. Kholkin, "Physical properties of strontium barium niobate thin films prepared by polymeric chemical method." Ferroelectrics 496, 177-186, 2016.

[36] K. Nishio, Y. Watanabe, and T. Tsuchiya, "Epitaxial Growth of $Sr_xBa1-xNb_2O_6$ Thin Films Prepared from Sol-Gel Process." Journal of Sol-Gel Science and Technology 26, 245-250. issn: 1573-4846 (2003).

[37] K. Nishio, N. Seki, J. Thongrueng, Y. Watanabe, T. Tsuchiya, "Preparation and Properties of Highly Oriented $Sr_{0.3}Ba_{0.7}Nb_2O_6$ Thin Films by a Sol-Gel Process." Journal of Sol-Gel Science and Technology 16, 37-45. ISSN: 1573-4846 (1999).

[38] J. F. Scott, and C. A. Paz De Araujo, "Ferrolectric Memories". Science, 1989, DOI: 10.1126/science.246.4936.1400.

[39] N. Setter, D. Damjanovic, L. Eng, G. Fox, S. Gevorgian, S. Hong, A. Kingon, H. Kohlstedt, N. Y. Park, G. B. Stephenson, I. Stolitchnov, A. K. Taganstev, D. V. Taylor, T. Yamada, S. Streiffer, "Ferroelectric thin films: Review of materials, properties, and applications." Journal of Applied Physics, 100, 051606 (2006), https://doi.org/10.1063/1.2336999.

[40] https://www.ti.com/lit/ml/szzt014a/szzt014a.pdf. Accessed: 2015-11-07.

[41] K. M. Rabe, M. Dawber, C. Lichtensteiger, C. H. Ahn, and J. M. Triscone, "Modern Physics of Ferroelectrics: Essential Background." Physics of Ferroelectrics, 2007, Volume 105, ISBN: 978-3-540-34590-9.

[42] Y. S. Hou, S. Ardro, and R. Q. Wu, "Hybrid density study of band gap engineering of $SrTiO_3$ photocatalyst via doping for water splitting." Research Gate, 2021.

[43] X. Fang, "Phase Transition in Strontium Titanate." Department of Physics, University of Illinois at Urbana-Champaign. https://guava.physics.uiuc.edu/ nigel/courses/563/Essays2013/PDF/fang.pdf.

[44] I. M. Nylund, "Transmission electron microscopy of ferroic materials." PhD thesis, Norwegian University of Science and Technology, Trondheim, 2022, ISSN: 2703-8084.

[45] R. F. Egerton, and M. Malac, " EELS in the TEM." Journal of Electron and Related Phenomena 143 (2005) 43-50, 2005.

[46] J. Verbeeck, S. Hens, P. Potapov, and D. Schryvers, "Electron Energy Loss Spectrometry." Encyclopedia of Analytical Science, 2nd edition, Elsevier, 2005, 324-331, https://doi.org/10.1016/B0-12-369397-7/00605-1.

[47] E. Christiansen, "TEM characterization of $LaFeO_3$ Thin Films on $SrTiO_3$ (111) substrates." Master's thesis, Norwegian University of Science and Technology, Trondheim, 2015.

[48] N. Tanaka, *Scanning Transmission Electron Microscopy Of Nanomaterials: Basics Of Imaging And Analysis*. Imperial College Press, 2014.

[49] A. A. Saleh, "Relationship between selforganization and creation/resorption of microstructural defects under ultrashort laser irradiation." PhD thesis, Université Jean Monnet, 2020, Research gate. DOI: 10.13140/RG.2.2.28826.39369.

[50] https://nano.oxinst.com/campaigns/downloads/simultaneous-eds-and-eels.

[51] T. Lukasiewicza, M.A. Swirkowicza, J. Decb, W. Hofmana, W. Szyrskia, " Strontium-barium niobate single crystals, growth, and ferroelectric properties." Journal of Crystal Growth, Science Direct, 2007.

[52] S. S. Thöny, K. E. Youden, J. S. Harris, Jr., and L. Hesselink," Growth of epitaxial strontium barium niobate thin films by pulsed laser deposition." AIP Publishing, 1994.

[53] https://www.brighton-science.com/blog/what-is-materials-science-and-why-is-it-crucial-for-new-product-development.

[54] Material Science, Advanced material charatreization with electron microscopy and spectroscopy, Thermo Fisher Scientific.

[55] M. Kohli, C. Wuethrich, K. Brroks, B. Willing, M. Fprster, P. Muralt, N. Setter, P. Ryser, "Pyroelectric thin-film sensor array." Sensors and Actuators A: Physical, 1997. https://doi.org/10.1016/S0924-4247(97)01484-2.

[56] J. Pérez, H. Amorin, J. Portelles, F. Guerrero. J. C. M'Peko, and J. M. Siqueiros, "Electrical Properties of the Titanium Modified SBN Ceramic System." Journal of Electronics, 2001.

[57] M. S. Kim, P. Wang, J. H. Lee, J. J. Kim, H. Y. Lee, and S. H. Cho, "Site Occupancy and Dielectric Characteristics of Strontium Barium Niobate Ceramics: Sr/Ba Ratio." Research Gate, 2002, [DOI: 10.1143/JJAP.41.7042].

[58] "ReciPro software", https://github.com/seto77/ReciPro/releases/tag/v.4.865

[59] V. V. Shvartsman, D. C. Lupascu, "Lead-Free Relaxor Ferroelectrics." Journal of the Americal Ceramic Society, 2012.

Appendix

A SBN 001

BF TEM image

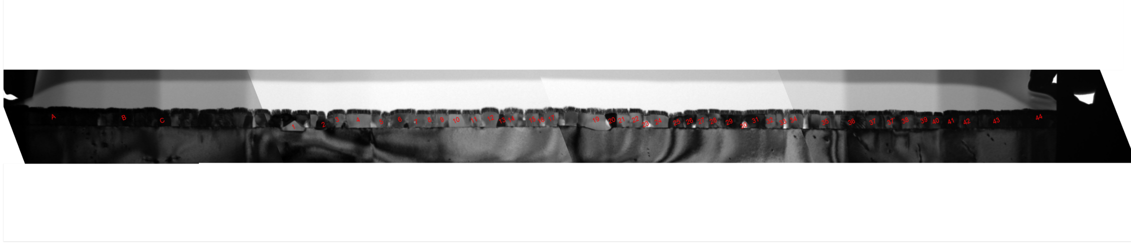

Figure A.1: BF TEM of SBN 001 when STO is on zone showing all the grains studied marked with different numbers.

DPs of grains with in-plane polarization

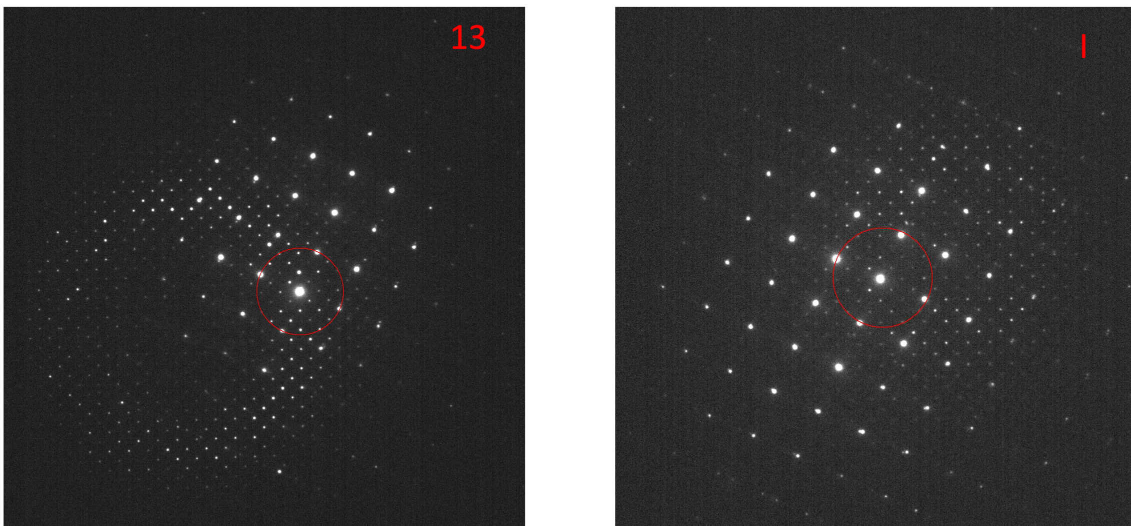

Figure A.2: DP from random grains with in-plane orientation. There were only two grains with in-plane polarization.

DPs of grains with out-of-plane polarization

There were 50 grains having out-of-plane polarization from a total of 54 grains. 38 out of 50 grains come to the zone after tilting in -18.4° and rest 12 out of 50 grains come to the zone after tilting in $+8.4^{\circ}$. Only three from each type are shown here.

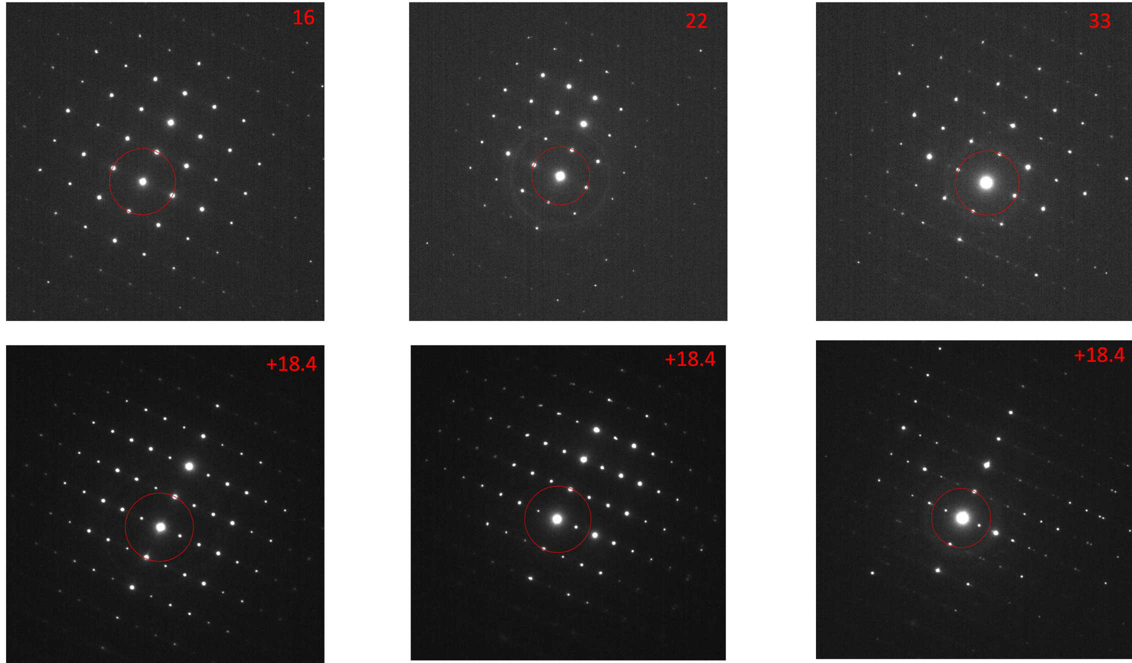

(a) DPs that come to zone after tilting $+18.4^{\circ}$

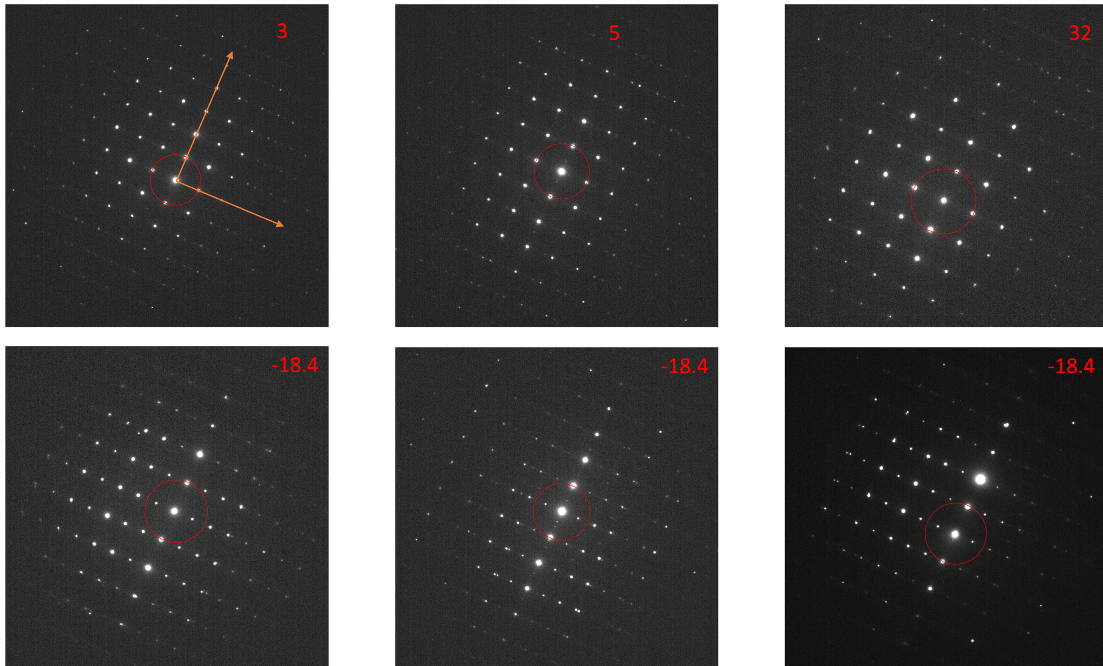

(b) DPs that come to zone after tilting in -18.4°

Figure A.3: DPs of grains with out-of-plane polarization

DPs of randomly oriented grains

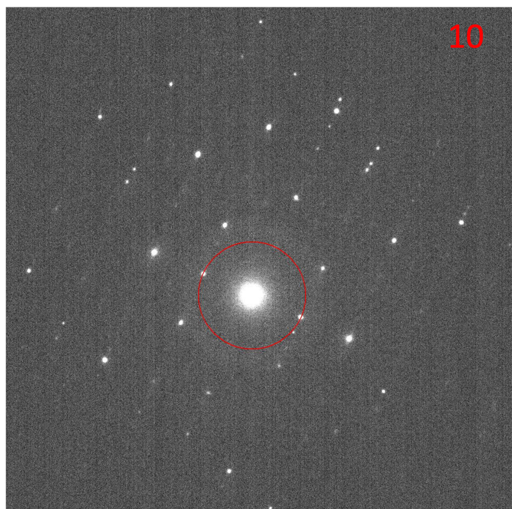

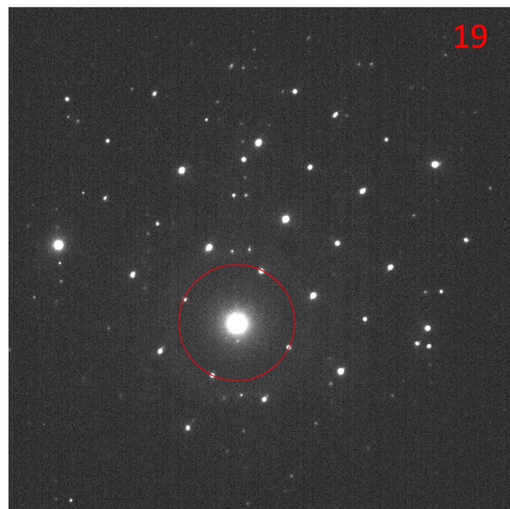

Figure A.4: DPs of grains with random orientation. There were only two grains with random orientation.

B SBN 310

BF TEM image

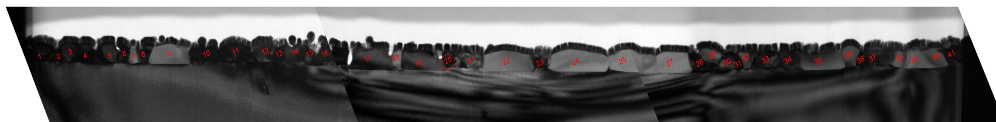

Figure B.1: Shows the BF TEM images of SBN 310 with the numbering of all the grains when STO is on zone.

DPs from grains with in-plane orientation

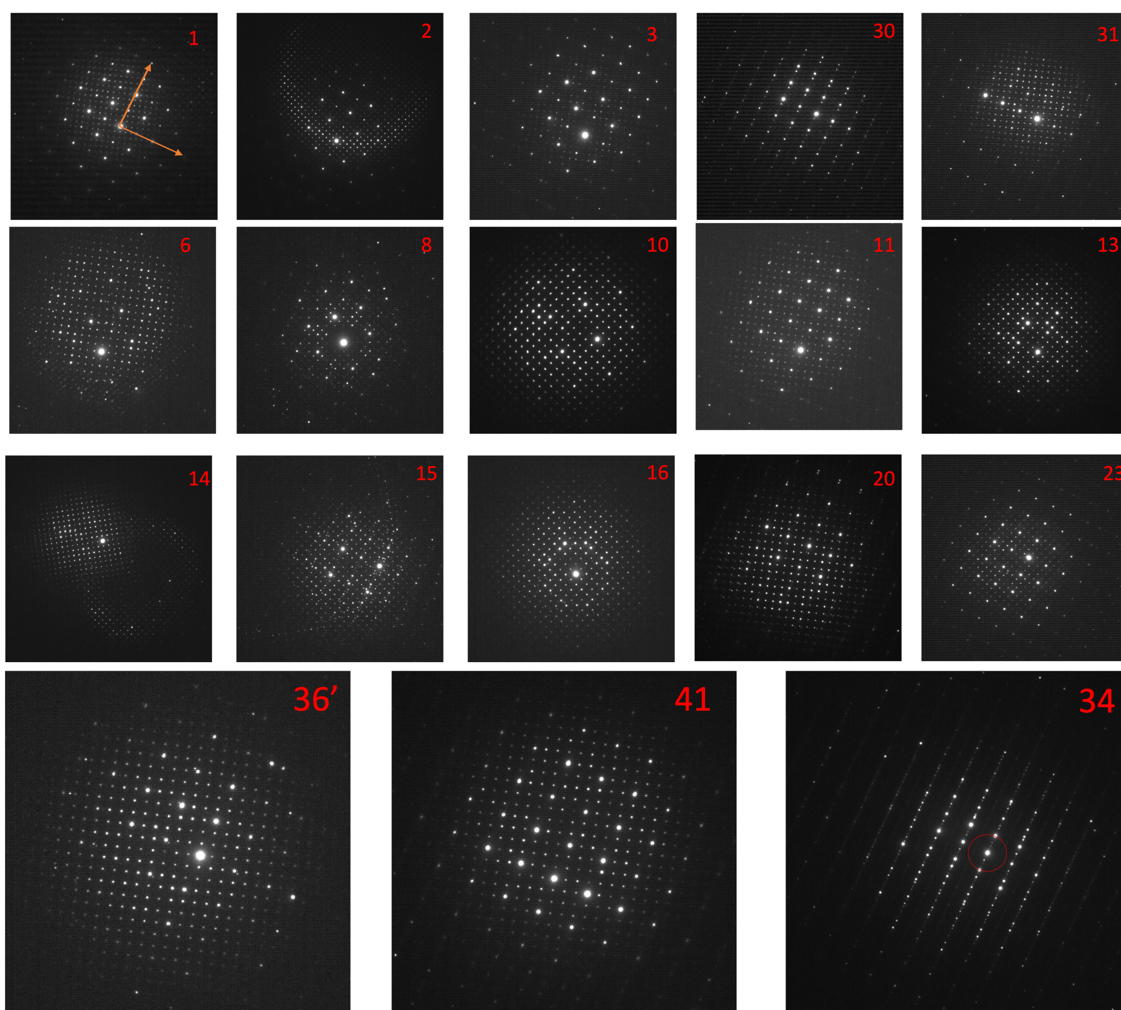

Figure B.2: DPs from all the grains with in-plane polarization.

DPs from grains with random orientation

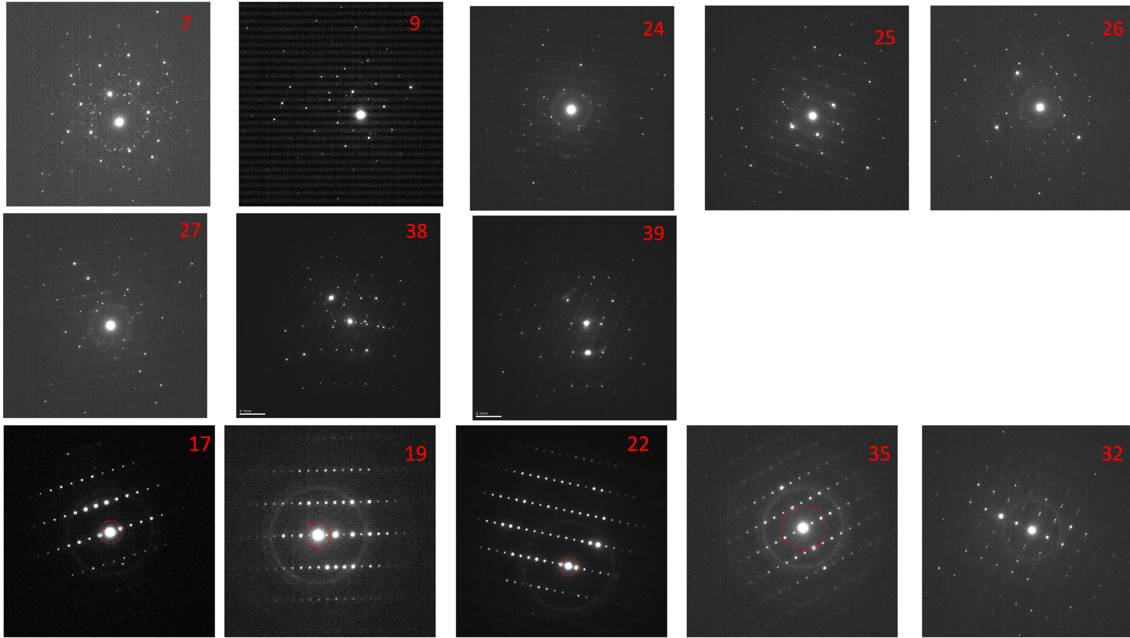

Figure B.3: DPs with random orienataion

DPs of grains with out-of-plane polarization

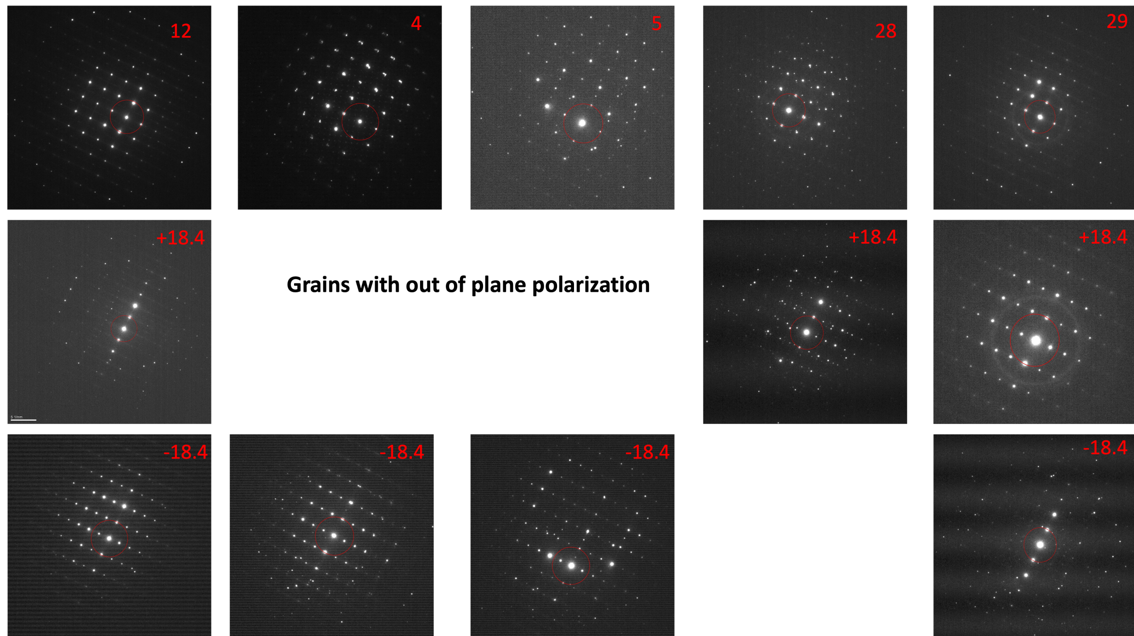

Figure B.4: DPs from grains with out-of-plane polarization. +18.4 and -18.4 refers to the angle of tilt. Grains 12, 4, and 5 come to zone after tilting in -18.4/degree, while grains 28, 29 come to zone after tilting +18.4°.

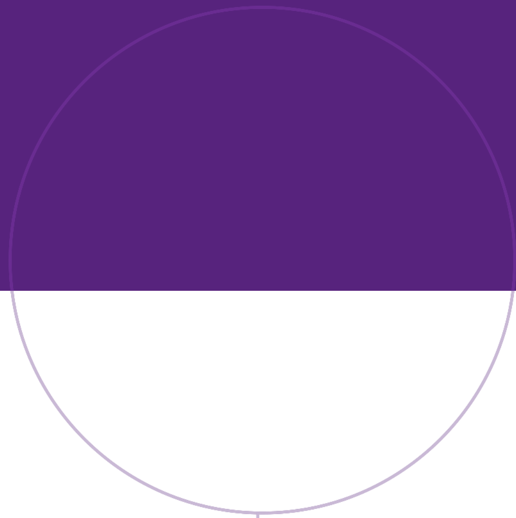

Norwegian University of
Science and Technology